SANDIA REPORT
SAND2019-15351
Printed December 19th, 2019

Sandia National Laboratories

Initial Simulations of Empty Room Collapse and Reconsolidation at the Waste Isolation Pilot Plant

Benjamin Reedlunn, Georgios Moutsanidis, Jonghyuk Baek, Tsung-Hui Huang, Jacob Koester, Edward Matteo, Xiaolong He, Karan Taneja, Haoyan Wei, Yuri Bazilevs, Jiun-Shyan Chen, Chven Mitchell, Robert Lander, and Thomas Dewers

Prepared by
Sandia National Laboratories
Albuquerque, New Mexico 87185
Livermore, California 94550

Issued by Sandia National Laboratories, operated for the United States Department of Energy by National Technology & Engineering Solutions of Sandia, LLC.

NOTICE: This report was prepared as an account of work sponsored by an agency of the United States Government. Neither the United States Government, nor any agency thereof, nor any of their employees, nor any of their contractors, subcontractors, or their employees, make any warranty, express or implied, or assume any legal liability or responsibility for the accuracy, completeness, or usefulness of any information, apparatus, product, or process disclosed, or represent that its use would not infringe privately owned rights. Reference herein to any specific commercial product, process, or service by trade name, trademark, manufacturer, or otherwise, does not necessarily constitute or imply its endorsement, recommendation, or favoring by the United States Government, any agency thereof, or any of their contractors or subcontractors. The views and opinions expressed herein do not necessarily state or reflect those of the United States Government, any agency thereof, or any of their contractors.

Printed in the United States of America. This report has been reproduced directly from the best available copy.

Available to DOE and DOE contractors from

U.S. Department of Energy
Office of Scientific and Technical Information
P.O. Box 62
Oak Ridge, TN 37831

Telephone: (865) 576-8401
Facsimile: (865) 576-5728
E-Mail: reports@osti.gov
Online ordering: http://www.osti.gov/scitech

Available to the public from

U.S. Department of Commerce
National Technical Information Service
5301 Shawnee Road
Alexandria, VA 22312

Telephone: (800) 553-6847
Facsimile: (703) 605-6900
E-Mail: orders@ntis.gov
Online order: https://classic.ntis.gov/help/order-methods



ABSTRACT

The Waste Isolation Pilot Plant (WIPP) is a geologic repository for defense-related nuclear waste. If left undisturbed, the virtually impermeable rock salt surrounding the repository will isolate the nuclear waste from the biosphere. If humans accidentally intrude into the repository in the future, then the likelihood of a radionuclide release to the biosphere will depend significantly on the porosity and permeability of the repository itself. Room ceilings and walls at the WIPP tend to collapse over time, causing rubble piles to form on floors of empty rooms. The surrounding rock formation will gradually compact these rubble piles until they eventually become solid salt, but the length of time for a rubble pile to reach a certain porosity and permeability is unknown. This report details the first efforts to build models to predict the porosity and permeability evolution of an empty room as it closes. Conventional geomechanical numerical methods would struggle to model empty room collapse and rubble pile consolidation, so three different meshless methods, the Immersed Isogeometric Analysis Meshfree, Reproducing Kernel Particle Method (RKPM), and the Conformal Reproducing Kernel method, were assessed. First, the meshless methods and the finite element method each simulated gradual room closure, without ceiling or wall collapse. All three methods produced equivalent room closure predictions with comparable computational speed. Second, the Immersed Isogeometric Analysis Meshfree method and RKPM simulated two-dimensional empty room collapse and rubble pile consolidation. Both methods successfully simulated large viscoplastic deformations, fracture, and rubble pile rearrangement to produce qualitatively realistic results. In addition to geomechanical simulations, the flow channels in damaged salt and crushed salt were measured using micro-computed tomography, and input into a computational fluid dynamics simulation to predict the salt's permeability. Although room for improvement exists, the current simulation approaches appear promising.

ACKNOWLEDGMENT

The authors would like to acknowledge Ross Kirkes and Brad Day for their helpful comments about the WIPP Performance Assessment, Mario Martinez for his thoughts on permeability and porosity, Till Popp for alerting us to the ventilation drifts at the Teutschenthal mine, and Chet Vignes, Shelly Nielsen, and Moo Lee for reviewing a draft of this report. We also thank Dr. David Kamensky for his help carrying out the FEniCS computations.

CONTENTS

1. Introduction **13**
- 1.1. Background . . . 13
- 1.2. Relevant Physical Processes . . . 17
  - 1.2.1. Gradual Room Closure . . . 17
  - 1.2.2. Fracturing Around the Room . . . 19
  - 1.2.3. Rubble Pile Consolidation . . . 19
  - 1.2.4. Rubble Pile Permeability . . . 20
  - 1.2.5. Crushed Salt Models versus Rubble Pile Models . . . 21
- 1.3. General Research Plan . . . 21

2. Assessment of Numerical Methods for Geomechanical Simulations **24**
- 2.1. Potential Numerical Methods . . . 24
- 2.2. Assessment Problems . . . 27
  - 2.2.1. Gradual Room Closure . . . 28
  - 2.2.2. Room Collapse and Rubble Pile Consolidation . . . 29
  - 2.2.3. Salt Material Model . . . 30
  - 2.2.4. Viscoplastic Scaling . . . 36

3. Immersed Isogeometric Analysis Meshfree Simulations of Empty Room Closure **38**
- 3.1. Introduction . . . 38
- 3.2. Two-Dimensional Room Closure . . . 39
  - 3.2.1. Prototyping in FEniCS . . . 39
  - 3.2.2. Immersed-Meshfree Analysis . . . 41
- 3.3. Two-Dimensional Roof Fall . . . 43
  - 3.3.1. Prototyping in FEniCS . . . 43
  - 3.3.2. Immersed-Meshfree Simulations . . . 45
- 3.4. 3D Smooth Room Closure . . . 48
- 3.5. Three-Dimensional Roof Fall . . . 49
- 3.6. Conclusions and Observations . . . 49
- 3.7. Future Directions . . . 50
  - 3.7.1. Non-Local Damage Model . . . 50
  - 3.7.2. Time Scaling . . . 51
  - 3.7.3. 3D Computations . . . 51
  - 3.7.4. Constitutive Modeling . . . 51

4. Reproducing Kernel Particle Method Simulations of Empty Room Closure **52**
- 4.1. Introduction . . . 52

4.2. Model Setup . . . 52
4.2.1. Triaxial Compression Test . . . 53
4.3. Numerical Approach . . . 54
4.3.1. Damage Regularization . . . 54
4.3.2. Pressure Projection . . . 55
4.3.3. Benchmark Problem: Notched Bar Compression Test . . . 56
4.4. Modeling of Empty Room Closure and Roof Falling . . . 60
4.4.1. Room Closure Modeling . . . 60
4.4.2. Roof Fall Modeling . . . 65
4.5. Summary . . . 79
4.6. Future Work . . . 80

5. Conforming Reproducing Kernel Simulations of Empty Room Closure 81
5.1. Introduction . . . 81
5.2. Model Setup . . . 81
5.2.1. Salt Model . . . 82
5.3. Results . . . 84
5.4. Future Work . . . 88

6. Further Analysis of Geomechanical Simulation Results 89
6.1. Introduction . . . 89
6.2. Room Size Analysis . . . 90
6.3. Ventilation Drift Collapse at the Teutschenthal Mine . . . 92

7. Development of Methods to Characterize Permeability/Porosity Relationships as a Function of Rubble Polydispersity 94
7.1. Introduction . . . 94
7.2. Methods . . . 94
7.2.1. WIPP Salt Sample Provenance . . . 94
7.2.2. Computerized Tomography and Image Analysis . . . 95
7.2.3. Geocosm Cyberstone Modeling . . . 95
7.2.4. CFD Modeling of Gas Transport . . . 95
7.2.5. The "Drop" Experiment . . . 95
7.3. Results . . . 96
7.3.1. CT Imaging . . . 96
7.3.2. Grain Size Distributions of Run-of-Mine Salt Floor Samples . . . 98
7.3.3. Grain Separates . . . 98
7.3.4. Cyberstone^{TM} Modeling . . . 99
7.3.5. CFD Modeling of Gas Transport in DRZ Core Fractures . . . 101
7.4. Conclusions . . . 105

8. Summary and Potential Future Work 106

References 111

Bibliography 111

Appendices **116**

A. Finite Element Modeling Details **116**
A.1. Model Setups for Room Shape and Size Studies 116
A.2. Numerical Settings for Room Shape and Size Studies 117
A.3. Numerical Settings for Gradual Room Closure Simulations 118

LIST OF FIGURES

Figure 1-1. WIPP layout. 14
Figure 1-2. Photographs of filled rooms at the WIPP. 15
Figure 1-3. Photographs of rubble piles resulting from roof falls at the WIPP (Carrasco 2019b). 16
Figure 1-4. Locations of upper and lower horizon disposal rooms within an idealized stratigraphy. 17
Figure 1-5. The effect of initial room shape on gradual room closure. 18
Figure 1-6. Horizontal and vertical closure percentages for an empty room compared against the same room filled with nominal or strong containers (modified from Reedlunn et al. (2019)). 20

Figure 2-1. Finite elements with element death. 25
Figure 2-2. Finite elements with interelement cracks. 26
Figure 2-3. Particle methods. 27
Figure 2-4. Gradual room closure simulation geometry and boundary conditions. 28
Figure 2-5. Room collapse and rubble pile consolidation geometry and boundary conditions. 30
Figure 2-6. Damage boundary. 33
Figure 2-7. Triaxial compression schematic 34
Figure 2-8. Constant strain rate tests and model predictions at room temperature, a constant strain rate of 10^{-6} s^{-1}, and four different radial confining stresses. 35

Figure 3-1. 2D room closure. Final configuration. Results with FEniCS. 40
Figure 3-2. 2D room closure. Time evolution of vertical and horizontal closures for the Lagrangian computation compared against the Sierra computation. 40
Figure 3-3. Immersed 2D room closure. Final configuration for two different discretizations. 41
Figure 3-4. Immersed 2D room closure. Time evolution of vertical and horizontal closures for the three discretizations compared against the Sierra computation. 42
Figure 3-5. Immersed 2D room closure strong scaling. 43
Figure 3-6. 2D roof fall. Clay seam. 44
Figure 3-7. 2D roof fall. Results with FEniCS at 0.1 yr. Red - failed material; Blue - intact material. 44
Figure 3-8. Immersed 2D roof falls with two different clay seam thicknesses. Roof fall and evolution of damage until closure. Red - failed material; Blue - intact material. 45
Figure 3-8. (Continued) Immersed 2D roof falls with two different clay seam thicknesses. Roof fall and evolution of damage until closure. Red - failed material; Blue - intact material. 46
Figure 3-9. Immersed 2D roof fall at 2 yr without modeling the clay seam. Red - failed material; Blue - intact material. 47

Figure 3-10. Preliminary 3D results. 48

Figure 4-1. A comparison between analytical and numerical solutions regarding the evolution of strain components and the damage variable in the triaxial compression test. 54
Figure 4-2. Master-slave nodal distribution in (a) notched bar compression test, and (b) room model with rounded corners. 56
Figure 4-3. Notched bar compression test. 57
Figure 4-4. Damage fields of the notched bar under compression at different simulation time: (top) without RKSR and (bottom) with RKSR. 58
Figure 4-5. Pressure fields of the notched bar under compression with M02 discretization: (a) without and (b) with pressure projection. 58
Figure 4-6. Pressure fields of the notched bar under compression with different discretizations. 59
Figure 4-7. Force-displacement curves of the notched bar under compression, without and with pressure projection. 59
Figure 4-8. Nodal distribution of sharp-corner room closure under different discretizations. 62
Figure 4-9. Room closure measurements for sharp corner model. 63
Figure 4-10. Computational efficiency of RKPM simulation. The details of the data of CPU time and discretization can be found from Table. 4-4. p is the number of processors employed in the simulation, and NP is the total number of nodes in the 2-layer discretization explained in Sec. 4.4. 63
Figure 4-11. Speedup for sharp corner model under different discretization refinement. 64
Figure 4-12. Damage distributions of room closure modeling under different discretizations. 65
Figure 4-13. Damage field of room closure modeling at different time with $h_{min} = 0.1m$. 66
Figure 4-14. Room closure measurements for creep-damage model under different discretizations. 67
Figure 4-15. Adaptive time scaling profile for modeling roof falling with $t_1^{mb} = 0.35$ and $t_2^{mb} = 1.35$: (a) physical time t versus momentum balance time t^{mb}, and (b) corresponding scaling factor. 67
Figure 4-16. Typical three stages of room closure with roof falling in the WIPP. 68
Figure 4-17. The roof falling process at the 39th year in empty room modeling with adaptive time scaling factor. 69
Figure 4-18. The room closure after the roof falling and impacting. 70
Figure 4-19. Final room closure configuration and the corresponding closure time for the cases with (a) $\alpha = 0.5$, (b) $\alpha = 2.0$, and (c) $\alpha = 3.0$ in Eq. (4.1). The left hand side is the full view of the room model and right hand side is the zoom-in view of the room closure configuration. 72
Figure 4-20. Circular area used to calculate the normalize porosity. 73
Figure 4-21. Normalized porosity in the empty room closure without clay seam, measured by Eq. (4.16) 73
Figure 4-22. Discretization of empty room with clay seam model. 74
Figure 4-23. Damage propagation of modeling the empty room closure with clay seam and $\alpha = 0.5$. 74
Figure 4-24. The roof falling process at the 7th year in empty room modeling with clay seam. 75

Figure 4-25. The room closure process following after the roof falling in the clay seam model 77
Figure 4-26. Final room closure configuration and the corresponding closure time for the cases with clay seam and (a) $\alpha = 0.0$, (b) $\alpha = 0.5$, (c) $\alpha = 2.0$, and (d) $\alpha = 3.0$. The left hand side is the full view of the room model and right hand side is the zoom-in view of the room closure configuration. 78
Figure 4-27. Normalized porosity in the empty room closure with clay seam. 78

Figure 5-1. Meshes used in the CRK room closure predictions. 83
Figure 5-2. Triaxial compression creep verification test. 84
Figure 5-3. Vertical room closure, CRK predictions. 85
Figure 5-4. Horizontal room closure, CRK predictions. 85
Figure 5-5. CRK room closure predictions. Coarse mesh (left), mid mesh (center) and fine mesh (right). 86
Figure 5-6. Hydrostatic stress predictions in early room closure. 87
Figure 5-7. Strong scaling study for a mesh with 48,962 nodes and 24,038 hex elements. Analyses were run on Sandia's Uno compute server. 87

Figure 6-1. A circular room, rimmed with an excavation damaged zone, idealized as a bigger room filled with a commensurate amount of idealized rubble 90
Figure 6-2. The effect of increasing a circular room's diameter and filling it with a commensurate amount of idealized rubble. 91

Figure 7-1. X-ray imaging of WIPP DRZ core sample. 96
Figure 7-2. X-ray tomographic reconstruction of bucket of run-of-mine salt. The bucket is approximately 12" across. 97
Figure 7-3. Cross section view of run-of-mine salt with voxel size of 94 microns. 97
Figure 7-4. X-ray tomographic reconstruction of "dropped" DRZ core piece. 98
Figure 7-5. Decimeter volume of run-of-mine salt bucket, showing original grey levels (left), segmented solid phase (middle), and separated grains (right). 99
Figure 7-6. Frequency histogram of grain separates in Fig. 7-5, with grain size expressed in phi scale (log base 2 of grain size in mm). 100
Figure 7-7. Grain separates taken from the top of the run-of-mine salt shown in Fig. 7-2 and Fig. 7-3. 101
Figure 7-8. An example salt clast geometry from the WIPP site in blue together with the convex meshes that approximate it in red. The green arrows indicate regions where the convex meshes deviate somewhat from the clast shape. 102
Figure 7-9. An alternative perspective of the same clast (blue) and convex meshes (red) shown in Fig. 7-8. 102
Figure 7-10. Rubble pack that resulted from depositing 1750 clasts with the shape shown in Fig. 7-8 into a cylindrical container. 103
Figure 7-11. Trimmed portion of the rubble pack shown in Fig. 7-10. Left: 3D geometry of trimmed region. Right: a vertical cross section along the pack x-axis. 103
Figure 7-12. Connected volumes shown in different colors, for the extension fractures in the DRZ core piece shown in Fig. 7-1A. 104
Figure 7-13. Triangular CFD mesh of WIPP DRZ core piece fracture. 104

Figure 7-14. Flow simulations of dry air transport through DRZ fracture using mesh shown in Fig. 7-13 with COMSOL Multiphysics. The left figure shows velocity (although not evident in the image, the interior of the volume shows velocities of 1.0e-8 m/s for the boundary conditions chosen). The right figure shows simulated stream lines, depicting a central flow pathway and several "dead-end" portions of the fracture volume. 105

Figure A-1. Room geometry, boundary conditions, and mesh used to investigate initial room shape and size on viscoplastic room closure. (2-to-1 rectangular room shown) 116

LIST OF TABLES

Table 2-1. Salt model parameter values. 33

Table 4-1. Numerical setting of the notched bar compression test 57
Table 4-2. Numerical setting of room closure study 60
Table 4-3. Discretization refinement for sharp cornered models 60
Table 4-4. Normalized CPU time by p processors of four different discretization. 61
Table 4-5. Discretizations of the empty room model in creep-damage modeling 63

Table 5-1. Discretizations used in the CRK empty room closure simulations 82
Table 5-2. Stable time increment and performance of CRK compared to FEM using the selective deviatoric hexahedral element. The discretization contained 48,962 nodes and 24,038 elements and 1 CPU on Sandia's Uno compute server was used. 88

1. INTRODUCTION

Author: Benjamin Reedlunn*

1.1. Background

The Waste Isolation Pilot Plant (WIPP) in southeast New Mexico is an operating geologic repository for defense-related transuranic nuclear waste. Waste containers are shipped from various waste generating sites across the United States to WIPP, where they are disposed about 660 m beneath the surface in a bedded salt formation known as the Salado (see Fig. 1-1). Rock salt (sodium chloride) is well suited to nuclear waste isolation for four important mechanical reasons. (1) Intact salt, without cracks, is virtually impermeable to fluid flow. (2) Cracks in salt heal with sufficient confining pressure and time, thereby closing off potential flow pathways. (3) Salt slowly viscoplastically flows in the presence of shear stress, such that underground rooms close in around the waste over time. (4) Salt is a good thermal conductor, which can be helpful for heat-generating waste. (Transuranic waste generates a negligible amount of heat, so this last advantage is not important for the WIPP.)

The United States Department of Energy has tasked Sandia National Laboratories to assess the WIPP's performance over the regulatory period of 10,000 years. If the repository is left undisturbed, Sandia's WIPP Performance Assessment (PA) shows that radionuclide release rates to the accessible environment are essentially zero, so the PA primarily focuses on the impact of a potential human intrusion event (US DOE 2014b). One scenario the PA frequently considers is an oil drilling operation accidentally drills a borehole from the surface into the repository, and continues drilling to penetrate a hypothetical pressurized brine pocket underneath the repository. (No brine pockets are known to exist underneath the WIPP, but pressurized brine has been found in the vicinity of the WIPP (see Section 2.1.3.3 of US DOE (1996)).) If that brine pocket has sufficient pressure, brine may migrate up the borehole over time, possibly flood the repository, and aid radionuclide transport to the highly permeable Culebra dolomite layer (see Fig. 1-1). Furthermore, cellulose and metal will degrade and corrode inside the repository if they come into contact with brine. These chemical reactions will generate gases that will be unable to escape the repository if the oil drilling operation subsequently seals off the borehole. A second human intrusion could then intersect a repository pressurized with gas and brine, increasing the likelihood of a radionuclide release.

To demonstrate that the risk of a radionuclide release due to a human intrusion is acceptably low, the PA must have accurate estimates of the permeability and porosity of the repository. If the permeability is nonexistent, then brine will only flood the immediate vicinity of the borehole and

*Sandia National Laboratories, P.O. Box 5800, Albuquerque, NM 87185, USA

transport a small to negligible amount of radionuclides to the biosphere. If brine can freely flow throughout the repository, then a much greater radionuclide release will be possible. The porosity of the repository also is important. A small storage volume coupled with a large amount of brine and gas will lead to high pressures. Higher pressures can drive brine and gas into regions of low permeability, and potentially drive brine and gas up a borehole to the earth's surface.

Sandia has models for the permeability and porosity of rooms filled with waste containers (Fig. 1-2a) and crushed salt (Fig. 1-2b) (Stone 1997; Camphouse et al. 2012). Although these filled room models have areas for improvement, they are based on science and engineering judgement. Sandia, on the other hand, does not have a model for the permeability and porosity of empty rooms as they close.

Room ceilings and walls at the WIPP have a propensity to collapse over time because salt cracks when exposed to shear stress without sufficient confining pressure. Cracks form in the excavation damaged zone (EDZ), also known as disturbed rock zone (DRZ), near the room due to the lack of stiff support (confining pressure). These cracks can lead to blocks of salt detaching from the surrounding rock formation. When blocks detach around filled rooms, Sandia has historically assumed the room contents support these blocks enough that the blocks still mate up with the surrounding rock formation as the room closes. When blocks detach around empty rooms, however, the blocks can fall several meters, land on the floor, and possibly break into smaller pieces, as shown in Fig. 1-3.

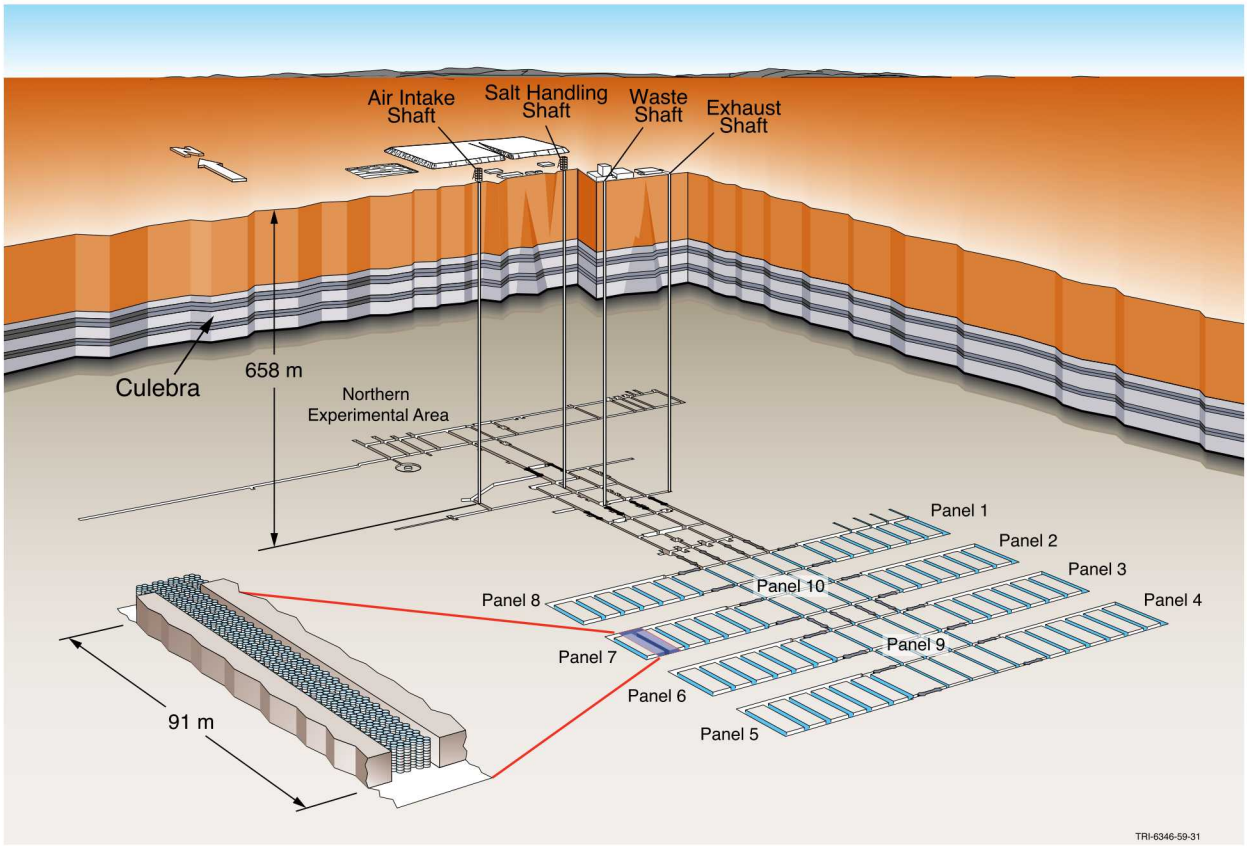

Figure 1-1. WIPP layout.

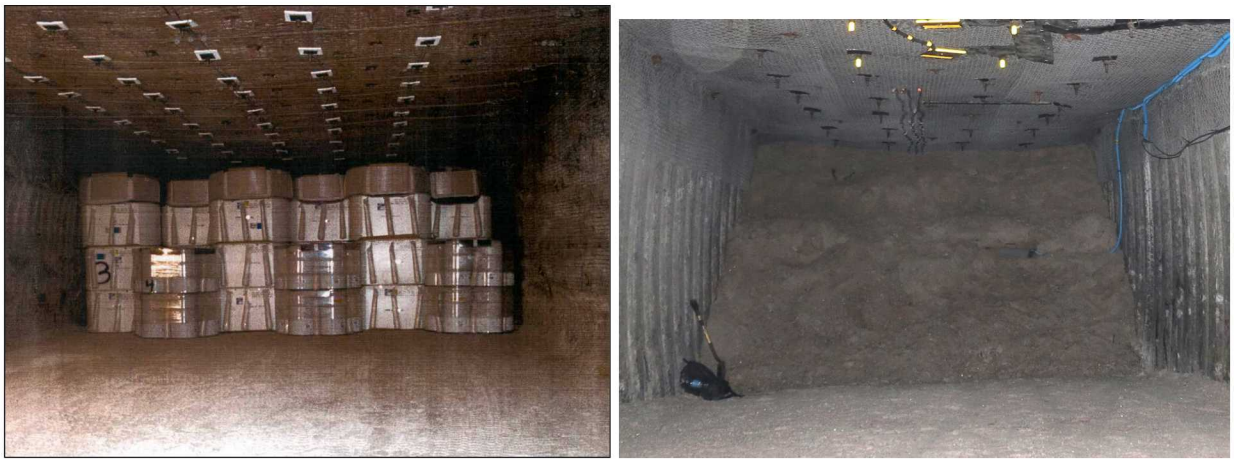

(a) Disposal room filled with waste and MgO **(b) Drift filled with crushed salt**

Figure 1-2. Photographs of filled rooms at the WIPP.

Roof falls can be largely prevented by installing rock bolts (see the ceilings in Fig. 1-2), which secure partially detached blocks to intact rock further from the room. These rock bolts are typically replaced every 3 to 5 years to ensure they remain competent, but personnel cannot install rock bolts in unsafe areas. The Northern Experimental Area (see Fig. 1-1) has been abandoned for decades and, without rock bolting, many roof falls have likely occurred in those rooms and access drifts. In addition, access to the WIPP underground was severely restricted for several years following the radiation release in Panel 7 and the fire of February 2014 (US DOE 2014a; US DOE 2015). This meant rock bolting was not possible throughout the repository, including the room and access drift depicted in Fig. 1-3. Nuclear Waste Partnership, the managing and operating contractor at the WIPP, currently plans to abandon the Northern Experimental Area, several rooms in Panel 7, and Panel 9 because of operational safety concerns (Carrasco 2019a), meaning these empty areas will be allowed to collapse and close naturally.

This decision to abandon portions of the WIPP, rather than fill them full of waste or crushed salt, raises the question, “How do the permeability and porosity of an empty room evolve over time?” The rubble piles in Fig. 1-3 undoubtedly have numerous flow pathways and gas storage sites. How much time will pass before the surrounding rock formation compresses a rubble pile to its final state?



(a) Lower horizon rubble pile in Panel 7, Room 4 (November, 2016)



(b) Upper horizon rubble pile in E300-S3650 access drift (September, 2016)

Figure 1-3. Photographs of rubble piles resulting from roof falls at the WIPP (Carrasco 2019b).

1.2. Relevant Physical Processes

Attempts to predict the permeability and porosity of empty rooms should consider the physical processes involved. This section presents processes that appeared important to the current authors at the onset of the project.

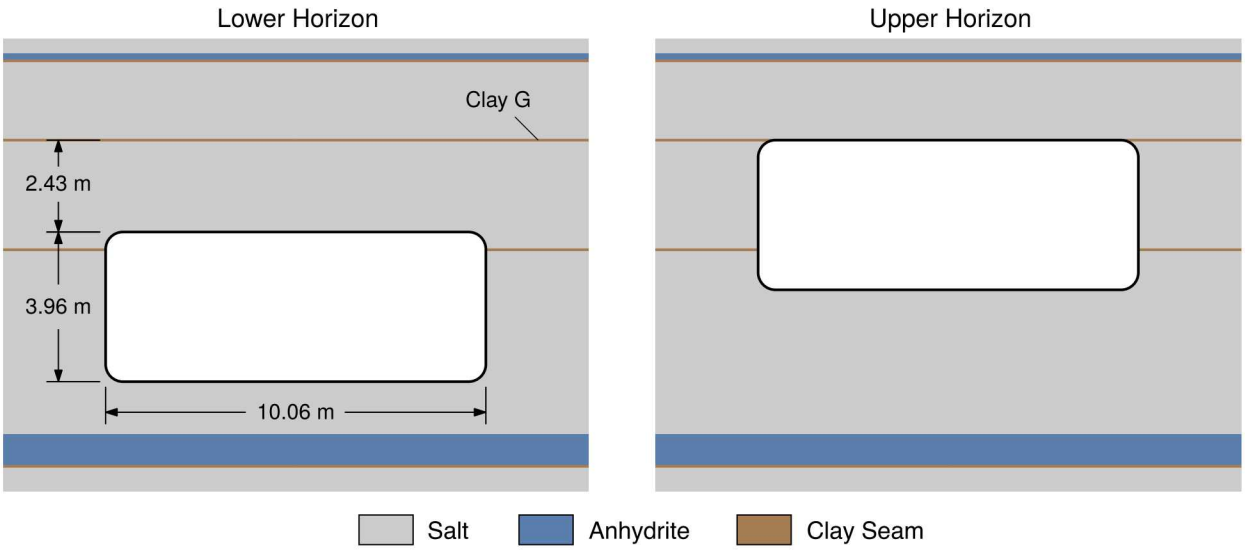

Figure 1-4. Locations of upper and lower horizon disposal rooms within an idealized stratigraphy.

To orient the reader who may be unfamiliar with the WIPP repository, a schematic the two disposal room horizons within an idealized stratigraphy is shown in Fig. 1-4. Most of the rock is salt (halite), but layers of anhydrite, and clay exist between the salt bedding planes. The anhydrite strata are sometimes referred to as marker beds (MB) because they are visually distinct from the neighboring salt. The clay layers are thin, usually less than 20 mm. The ceilings of WIPP disposal room panels 3, 4, 5, 6, and 10 are part of the lower horizon because they are about 2.43 m beneath Clay G, while the ceilings of disposal room panels 1, 2, 7, 8, and 9 are part of the upper horizon because they are coincident with Clay G.

1.2.1. Gradual Room Closure

The mechanisms of gradual room closure, without any roof falls, are the driving force for empty room closure. Roof falls reorganize the void space in the room, but the room actually closes because the surrounding salt viscoplastically flows, the clay seams slide, and the anhydrite strata deform and fracture. All these deformation processes depend on the stress field evolution around the room, which depends, in part, on the geometry of the room within the stratigraphy. The stress fields also depend on whether gas due to potential cellulose and metal degradation supplies a back pressure to the surrounding rock formation. An empty room closure model should ideally capture these dependencies.

Development of Sandia's model for gradual room closure at the WIPP has been sporadic over the years. Readers interested in the history should review Munson et al. (1987), Munson et al. (1989),

Munson (1997), Reedlunn (2016), and Reedlunn (2018b). Most recently, Appendix B in Reedlunn et al. (2019) compared the current model against the 4 to 8 years of closure measurements in a square cross-section room (Room D), a rectangular cross-section room (Room G), and a circular cross-section room (Room Q) at the WIPP. The model under-predicted the initial year of rapid closure by as much as 2×, but it reasonably predicted the closure rates after one year. Although it would engender confidence to capture the initial transient, closure rates following the initial transient are typically considered most important for long-term closure predictions.

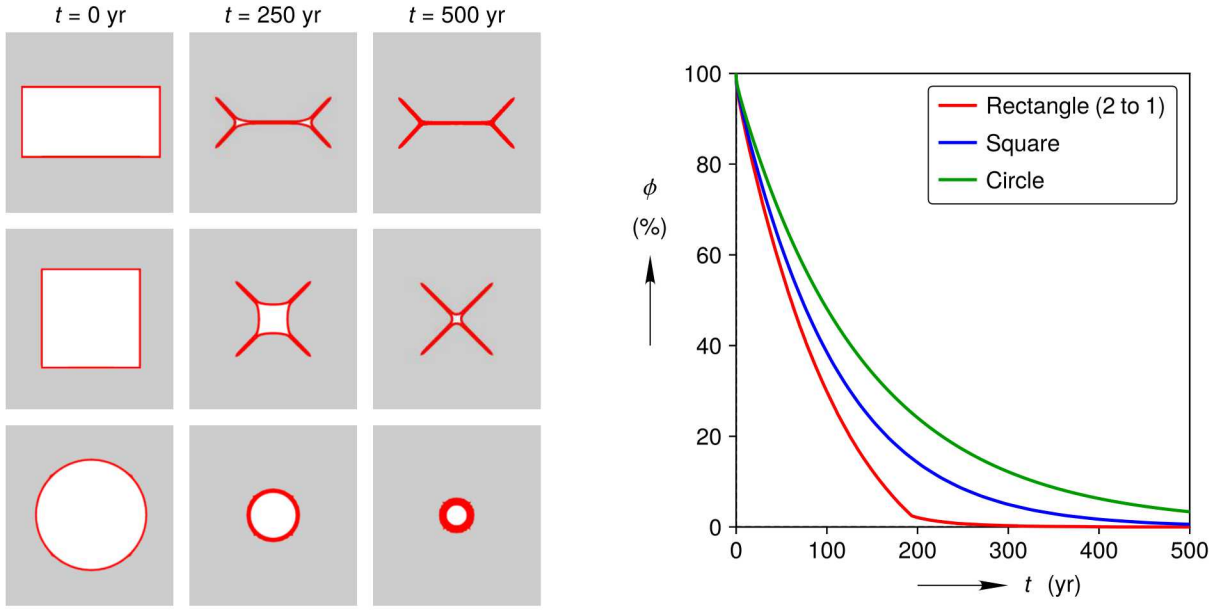

(a) Deformed room shapes at selected times **(b) Room porosity histories**

Figure 1-5. The effect of initial room shape on gradual room closure.

The initial room shape has an impact on the time required to gradually close a room. To quantify this effect, plane strain gradual room closure simulations were performed using a simulation setup similar to the Room D, G, and Q validation studies. (See Appendices A.1 and A.2 for further details of the model setup and numerical settings.) Three different room cross-sections, each with the same initial void volume V_0, were simulated while monitoring the current void volume V. The gas within each room was allowed to escape as the room closed, such that the gas provided zero back pressure. Fig. 1-5a depicts the room cross-sections at $t = 0$, 250, and 500 yr, where the layer of finite elements closest to the room has been colored red. The rectangular room closes into a "bow-tie" shape, the square room closes into an "x" shape, and the circular room simply becomes a smaller circle. Fig. 1-5b shows the room porosity $\phi = V/V_0$ plotted against time t for a more quantitative comparison. The room porosities all start at $\phi = 100$ %, rapidly reduce by at least 75 % in the first 200 yr, and then the porosity reduction rate slows down. The circular room requires about twice as long as the rectangular room to reach $\phi = 10$ %, but the circular room may require as much as five times longer to reach $\phi = 1$ %. Attainment of 1 % porosity or lower may be necessary for flow pathways to effectively close down.

1.2.2. Fracturing Around the Room

Another reason to consider the different room shapes in Fig. 1-5 is fractures in the rock surrounding a room change the effective shape and size of the room. Fractures form in regions of high shear stress and low confining pressure near the room, but that causes salt blocks to detach and shed their load to the surrounding rock salt. This load redistribution will cause further fracturing in new regions of high shear stress and low confining pressure, possibly starting the process anew. Eventually the process must stabilize, so it is reasonable to assume a rectangular or square room could transition towards a more circular shape, since a circle distributes the shear stress most evenly. See Chapter 6 for a simple analysis demonstrating how room size also affects empty room closure.

Fractures, of course, additionally lead to rubble piles, and the fracture network controls the size and character of the rubble pile. Roof falls tend to detach at anhydrite stringers or at clay seams, but both detachment modes occur no higher than the first clay seam above the room. As shown in Fig. 1-4, the distance from the lower horizon ceiling to the nearest clay seam (Clay G) is larger than the distance from the upper horizon ceiling to the nearest clay seam (Clay H). Accordingly, roof falls on the lower horizon tend to involve large blocks of salt (see Fig. 1-3a), while roof falls on the upper horizon tend to involve a number of smaller blocks that detach at anhydrite stringers (see Fig. 1-3b) (Kicker et al. 2017).

1.2.3. Rubble Pile Consolidation

To accurately capture rubble pile mechanics, a model would ideally include rubble pile reorganization, fracture, deformation, and healing. Unless the larger rubble pieces all mate up nicely with one another as the room closes, they will need to rearrange and break into smaller pieces to fill in the gaps between other rubble pieces. Rubble reorganization and fracture will likely reduce the bulk of the room porosity in the initial compaction stages. Later, however, when roughly hewn faces of rubble come into contact with one another, they will not mate up perfectly. Rubble pieces will need to deform to properly mate with neighboring rubble and squeeze out the last bits of porosity. This deformation would involve microcracking, elastic effects, dislocation based viscoplasticity, and pressure solution redeposition. Pressure solution redeposition might be accelerated when rubble breaks and releases moisture from brine pockets. Once rubble pieces experience low enough shear stress and high enough confining pressure, the microscopic fractures within the rubble will heal and the neighboring rubble pieces will fuse together.

The size of the rubble pieces that settle on the floor after a roof fall will likely be important in the initial compaction stage, because larger rubble pieces probably require more time to break up than smaller rubble pieces. Once the surrounding rock salt contacts the rubble pile, the pile will first rearrange, but larger rubble pieces will soon lock up and supply back pressure. This back pressure should reduce the shear stress in the surrounding formation and slow down the process of room closure. Eventually the surrounding formation should supply enough compressive pressure to the rubble pile to deform and break the bigger pieces into medium size pieces. Without back pressure, the surrounding formation's shear stress should increase again, allowing the process to

repeat until all the bigger pieces break into smaller pieces. When the rubble pieces are small enough, then room closure should be able to substantially reduce rubble pile porosity.

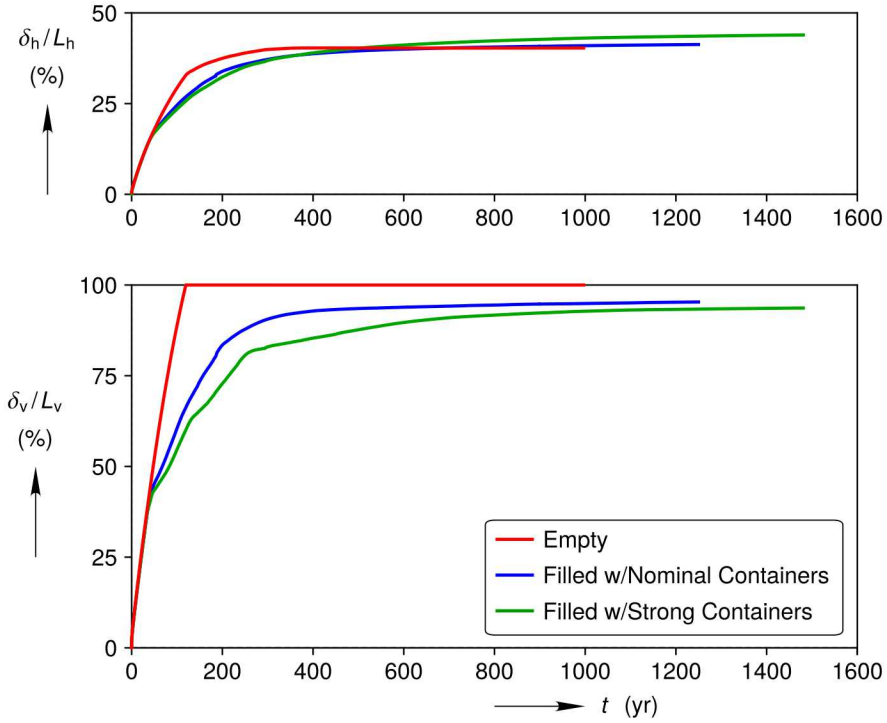

Figure 1-6. Horizontal and vertical closure percentages for an empty room compared against the same room filled with nominal or strong containers (modified from Reedlunn et al. (2019)).

Figure 1-6 demonstrates that room closure depends on the amount of back pressure supplied by the contents of the room. As discussed in Reedlunn et al. (2019), Fig. 1-6 plots the room horizontal closure δ_h normalized by the room width L_h and vertical closure δ_v normalized by the room height L_v against time t for three different cases: an empty room, a room full of nominal strength containers, and a room full of "strong" containers with increased yield strengths. Containers are obviously not the same as rubble, but the following principle still applies. Increasing the resistance of the room contents (increasing the back pressure) increases the time required to asymptotically reach the final compacted state.

1.2.4. Rubble Pile Permeability

The permeability of the rubble pile will intimately depend on the character of the flow network within the pile. Many small, rough, tortuous, cracks will give lower permeability than a few large, smooth, straight, pathways of equivalent volume. Similarly, a highly interconnected flow network will have higher permeability than a set of nearly isolated pores of equivalent volume. We may know whether permeability increases or decreases upon varying a single variable, while holding all other variables constant, but quantitative sensitivities likely depend on interactions between variables. For example, changing the mean effective path diameter by 10 % will play a bigger role

with small, long, tortuous, paths than large, short, straight paths. A permeability model should ideally include all of these effects and their couplings.

1.2.5. Crushed Salt Models versus Rubble Pile Models

Crushed salt has much in common with a rubble pile, so one might ask, "Why not model a rubble pile using the same methodology as crushed salt models?" Crushed salt models, such as that proposed in Callahan (1999), handle much of the complexity discussed above in a semi-empirical, implicit, manner. This approach is possible because the diameter of a crushed salt grain is at least 10× smaller the diameter of a typical triaxial compression sample and 400× smaller than the height of a disposal room at WIPP. One can test crushed salt samples in a laboratory under a wide variety of loading conditions, while measuring sample porosity and permeability. One can then use the results to parameterize a macroscopic, homogenized, model appropriate for disposal room scale simulations. The rubble pieces in Fig. 1-3, however, are far too big to be tested in any triaxial compression cell of which the authors are aware. Furthermore, even if the smaller rubble in Fig. 1-3b could be tested in a laboratory, the rubble pile and the access drift would probably still lack sufficient scale separation. The gradients in stress, strain, porosity, and permeability due to the rough room surfaces pushing on the rubble pile would likely be the same scale as the rubble pieces themselves.

1.3. General Research Plan

The previous section aimed to convey that empty room closure involves a series of interconnected processes. Permeability depends on the flow pathway geometry; the flow pathways depend on how the rubble pile compacts; the rubble pile evolution depends on the initial rubble pile character; and the initial rubble pile character depends on the fractures surrounding the room. Moreover, although empty rooms close due to viscoplasticity of the surrounding rock formation, fracturing around the room and back pressure from the rubble pile affect the surrounding formation's viscoplastic response. The effects are coupled.

In light of these dependencies, Sandia is striving to build an empty room closure model that includes as many of the relevant physical processes as practically possible. This is, of course, an ambitious endeavor and approximations will likely be made to make the model tractable. Even if the model does not capture all processes perfectly, including them allows one to turn each off and on to determine how important a given process is. In this manner, one could use the high-fidelity model to develop a reduced order model with a scientific basis behind it rather than unexplored assumptions. The remainder of this section describes, on a conceptual level, how the model might capture each process and how one might validate the model's predictions.

The Munson-Dawson (M-D) model (Munson 1997; Reedlunn 2018a) (also known as the Multi-Mechanism Deformation model) serves as a good starting point for the viscoplasticity of the surrounding rock mass and rubble, but it may be worth revisiting. The Room D, G, and Q validation studies showed the gradual room closure model captures the closure rates after one year, yet it fails to capture the magnitude of the first year of closure. One possible cause is the

M-D salt material model may not capture some aspects of transient creep, such as kinematic hardening. Although long-term closure rates are most important, short-term transient behavior may influence empty room closure. When fractures form in the surrounding rock mass, or when pieces of rubble come in or out of contact, the stresses in the salt redistribute, causing a new transient phase. Integrated over the total period of empty room closure, these transient effects could begin to approach the importance of steady-state creep.

Accurately predicting fractures around a room and the subsequent rubble pile formation may be a difficult venture. Several salt models include damage and fracture (see, for example, Chan et al. (1998), Günther and Salzer (2012), and Hampel (2015)), but Sandia has yet to implement or gain experience with those models. Once implemented, models can be compared against the lab scale room closure experiments proposed by Herrick et al. (2017). More significantly, fracturing around the rooms at the WIPP may depend heavily on the size and distribution of defects, such as anhydrite stringers, within the salt. One cannot possibly characterize all the defects in the ceiling of every empty room, so we may need to resort to stochastic descriptions. Once the roof fall lands on the floor, further fracturing into a rubble pile may also depend on defects within the salt. It may inform model development to perform drop tests on large diameter core extracted from the EDZ. In any case, the rubble piles in Fig. 1-3 and other observations at the WIPP can guide the roof fall modeling. If the model has to be tuned to represent reality, then we will at least have a tool to generate rubble piles that also incorporates how changing the room shape and size alters room closure.

Another avenue to generate synthetic rubble piles is to scan crushed salt samples using high-resolution X-ray micro-computed tomography. One could then increase the digitized grain sizes to represent a rubble pile, insert the rubble in random locations inside a disposal room, let the rubble settle due to gravity, and remove a volume of salt above the room equivalent to the synthetic rubble pile volume. Although this would be a less natural rubble pile creation process, it may allow us to quickly generate a large number of rubble pile realizations with different grain size distributions.

The flow pathways through the rubble pile will exist on multiple length scales. Macroscopic flow pathways, with characteristic dimensions of 10 mm or more, are likely too large for laboratory testing, so we will seek to explicitly represent them in the model. By simulating rubble rearrangement, fracturing, and deformation, the model will attempt to predict the length of time required to shut off those macroscopic reservoirs for gas and brine flow. The porosity and permeability of microscopic flow pathways, by contrast, will be modeled implicitly as internal state variables inside the salt constitutive model. This approach is currently used to model the EDZ and crushed salt because one can measure microscopic porosity and permeability on laboratory sized samples.

With an explicit representation of the macroscopic flow pathways and an implicit representation of the micro-permeability, we should be able to compute the effective permeability of the rubble pile using computational fluid dynamics. One can specify a fluid viscosity, specify a pressure gradient across the rubble pile, obtain a flow rate through the rubble pile, and compute an effective permeability. (See Section 4 in Martinez et al. (2017) for an example.) If we limit ourselves to flow of gases that do not interact with the salt, then the permeability simulations can be uncoupled from the rubble pile consolidation simulations.

Validation of the porosity and permeability predictions will be challenging because we cannot wait 100 to 1,000 years to observe the closure of an empty room at the WIPP. Instead, we plan to assume the physical processes are scale independent and scale the model of the rubble pile down to the size of a laboratory sized crushed salt sample. Laboratory tests on crushed salt have already been performed at elevated temperatures and compaction stresses to quickly approach intact salt behavior on the order of a year rather than a century. We would likely start with comparing the model simulations against crushed salt samples with a tight grain size distribution and graduate to more polydispersed samples. Sandia's involvement in the KOMPASS project (Kuhlman et al. 2019), which seeks to understand the behavior of crushed salt, could prove useful here. Validating against such crushed salt experiments, of course, assumes the physical processes are length scale independent and that we understand how the processes scale with stress and temperature. If these scaling effects cause irreconcilable differences between the model predictions and crushed salt measurements, another option is to validate against empty drift closure in old mines.

Extracting useful information from empty drift closure in old mines will have its own host of challenges. The geomechanics at the mine would likely be different than those at the WIPP. This means the mine's salt would need to be characterized, a material model would need to be calibrated, and a structural model would need to be validated against mine observations and measurements. In addition, measurements of porosity and permeability of the rubble pile within the closing drift would likely be difficult to obtain or non-existent. Nevertheless, full-size drift closure under conditions similar to drifts at the WIPP would not have the scaling effects that could hamper model validation against crushed salt experiments, so observations in old mines are worth considering. One possible case study is the closure of several empty ventilation drifts at the Teutschenthal Mine in Germany. See Section 6.3 for further discussion of the Teutschenthal ventilation drifts.

2. ASSESSMENT OF NUMERICAL METHODS FOR GEOMECHANICAL SIMULATIONS

Authors: Benjamin Reedlunn[†] and Jacob Koester[†]

The research plan outlined in Section 1.3 will require significant model development and validation efforts, but it also requires numerical methods appropriate for the physical processes. Several geomechanical processes in empty room closure can be challenging for numerical methods: fracture, pervasive contact, moderately large deformations (<100 % strain), the nearly incompressible deformation of intact salt, and healing. One cannot develop a model without a platform to test it on. As one might expect, every numerical method has strengths and weaknesses, so one should select methods whose strengths align with the problem of interest. Section 2.1 briefly describes a few candidate numerical methods, but the review is by no means exhaustive. Section 2.2 presents two problems used to assess the suitability of select methods.

2.1. Potential Numerical Methods

Fracture is a difficult process for many numerical methods. The fundamental difficulty is most materials macroscopically behave as a continuum as they deform, yet materials form discrete cracks when failure occurs. A given numerical method is expected to simultaneously capture continuously varying fields as well as discontinuities at cracks. These cracks, of course, can nucleate, propagate, and branch at any location within the material. One common issue with many methods is discretization structure dependence: cracks artificially follow discretization lines (see Fig. 2-1b), rather than their natural fracture path. An unstructured discretization permits a more natural fracture path, but it still contains preferred pathways. Another common issue is discretization size dependence due to material softening. Softening is used to create traction free crack surfaces, but it also causes the damage zone to localize within a few discretization units, which leads to fracture patterns that do not converge with discretization refinement. One can reduce or eliminate this tendency to excessively localize with a regularization scheme, but such schemes often add non-negligible computational expense.

The finite element method (FEM) is the most popular numerical method in solid mechanics for good reason, but it has difficulties with simulating fracture and severe deformations. Analysts frequently approximate cracks in the FEM by simply deleting elements once they reach a fracture criterion (see Fig. 2-1). Heavily deformed elements are also deleted to avoid polluting the rest of the analysis with non-sensical results. Although simple, this approach causes mass (and volume) loss (see Fig. 2-1a), which would artificially increase the porosity of the rubble pile with every

[†]Sandia National Laboratories, P.O. Box 5800, Albuquerque, NM 87185, USA

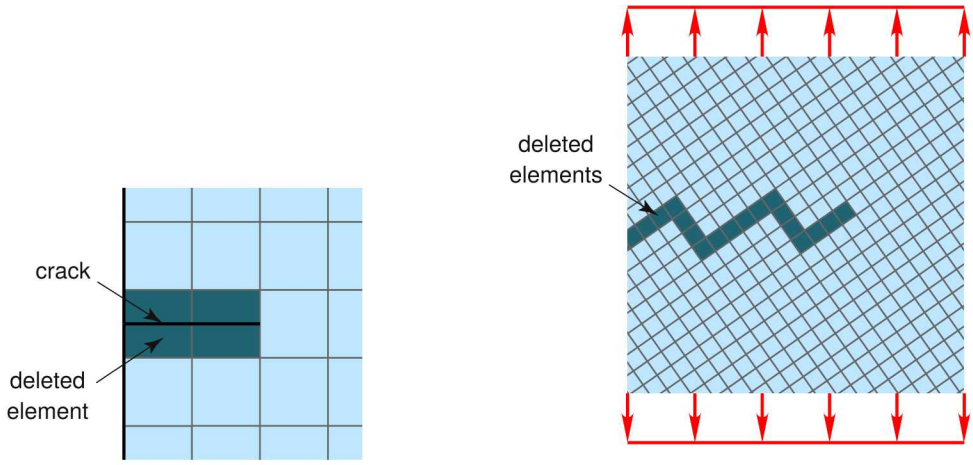

(a) Mass loss associated with element death

(b) Mesh structure dependence

Figure 2-1. Finite elements with element death.

fracture. Element death also struggles with simulating shear failure (or heavy distortion) under a compressive mean stress. A failed piece of salt should still be able to sustain compressive stress, but discarding an element leaves a void without compressive resistance. The surrounding material must then absorb an increase in stress, which can cause fractures to propagate when they might have otherwise been arrested.

Interelement crack methods avoid deleting elements by inserting cohesive zone elements in between continuum elements (see Fig. 2-2a), and forcing cracks to form at these cohesive zone elements. The user defines the cohesive zone element's behavior by specifying its thickness, normal stiffness k_n, shear stiffness k_s, and failure criterion. Once the failure criterion is reached, the cohesive zone element can be deleted without losing mass. The cohesive zone element's thickness also provides a softening length scale, obviating the need for a regularization scheme. Unfortunately, it is not trivial to determine the cohesive zone element's behavior from experiments on relatively homogeneous material without clear layering. In addition, each cohesive zone element adds to the model's computational expense. One can make the model relatively insensitive to the element's mechanical compliance and computational expense by selectively inserting cohesive zone elements, as shown in Fig. 2-2b, but this approach creates preferred fracture pathways and large indivisible blocks of continuum elements. Blanket insertion (see Fig. 2-2c), on the other hand, increases the number of fracture pathways and reduces the indivisible block down to a single continuum element, but increases computational expense and mechanical compliance. One could overcome these limitations if cohesive zone elements could be made rigid until cracks nucleated, but the robustness and accuracy issues with heavily distorted continuum elements would remain.

Many methods refrain from using continuum elements and discretize the material as a collection of points or "particles". The Discrete Element Method (DEM), Molecular Dynamics (MD), Peridynamics (PD), and variants of Smooth Particle Hydrodynamics (SPH) can be considered particle methods. The user specifies various particle-to-particle interactions, such as a normal

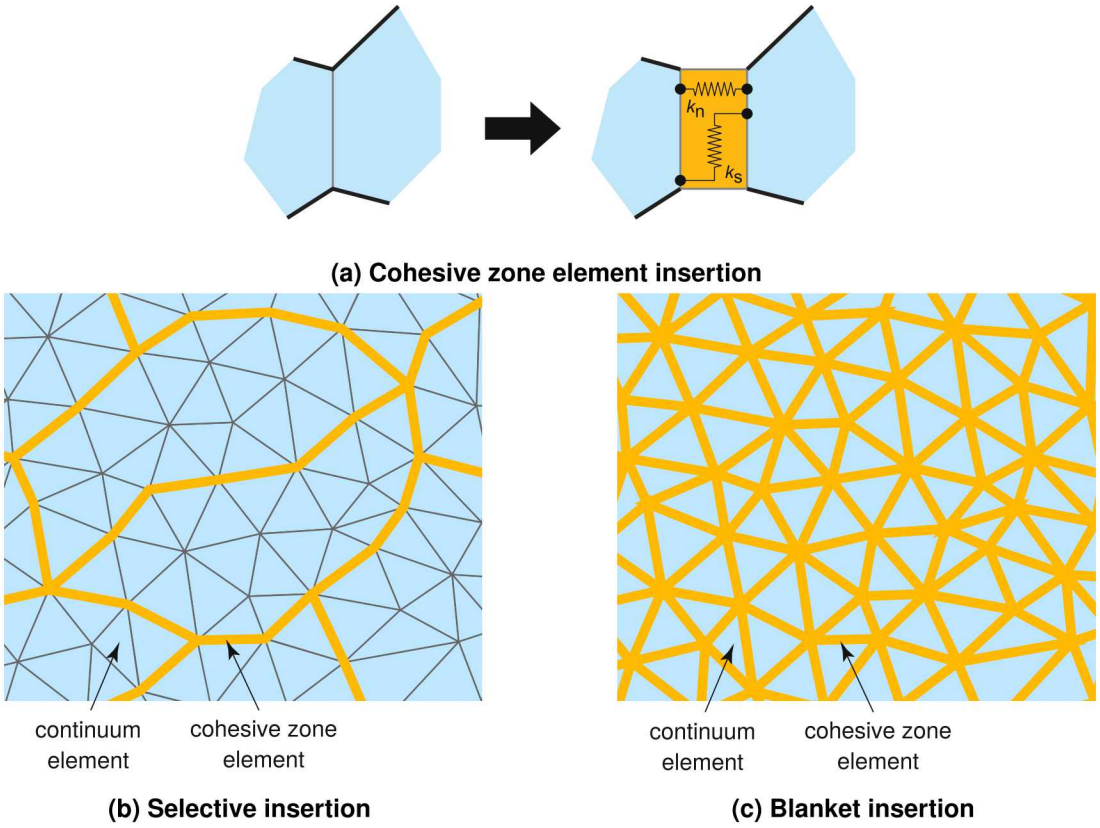

Figure 2-2. Finite elements with interelement cracks.

stiffness k_n, shear stiffness k_s, and failure criterion (see Fig. 2-3a) to allow the material to deform and fracture. When the particle-to-particle failure criterion is met, the particles simply separate, while preserving mass, as shown in Fig. 2-3b. Fracture pathways will still depend on discretization structure somewhat, but a fracture has many more potential propagation directions in Fig. 2-3b than in Fig. 2-2b. Particle methods also can handle severe deformations and healing more seamlessly than element methods. Unfortunately, constitutive models developed for solid continua often cannot be easily converted into particle-to-particle interactions. One must develop new material models and calibrate them against experiments, which is not trivial since an assembly of many particles behaves differently than a pair of particles.

Several meshless methods, such as the reproducing kernel particle method (RKPM) (Chen et al. 1996) and the material point method (MPM) (Sulsky et al. 1994), combine some advantages of element methods and particle methods. Like element methods, these meshless methods use a variational formulation and compute the strain, or strain increment, at a material point using shape functions, meaning these methods can use classical continuum-level material models. Like particle methods, these methods handle fracture without mass loss and without significant mesh structure dependence. They also more seamlessly simulate severe deformation and healing. Of course, the RKPM and MPM are not without drawbacks. Classical MPM suffers from a cell-crossing instability, but this can be resolved with a smooth background discretization, as is done in the Immersed IGA Meshfree method (Bazilevs et al. 2017b; Bazilevs et al. 2017a).

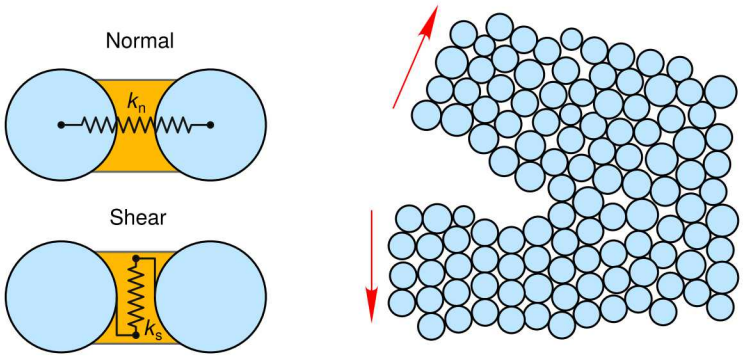

(a) Particle interactions **(b) Particle method fracture**

Figure 2-3. Particle methods.

Another potential issue is surfaces are implicitly represented as "mushy" boundaries rather than explicit discontinuities. This means fractured surfaces must sufficiently separate to stop interacting, contacting surfaces begin interacting before explicitly meshed surfaces would interact, and classical frictional sliding models are not easily implemented. Solutions to these surface issues have been developed (see Chi et al. (2015) and Homel and Herbold (2017), for example). In particular, Koester and Chen (2019) created the Conformal Reproducing Kernel (CRK) method, which is a variant of RKPM, with kernels that conform to the boundaries of a given material. A third potential issue is meshless methods are often reported to require longer run times than equivalently resolved element or particle methods.

We elected to continue assessing the RKPM, Immersed IGA Meshfree method, and CRK method over other approaches for several reasons. First, the mass loss and transfer of stress to neighboring elements are large drawbacks to element death. Second, the need to develop new material model formulations for cohesive zone elements and particle interactions methods creates a large barrier to even starting to use interelement crack methods or pure particle methods. Third, Sandia will likely continue to invest in meshless methods for other applications, so the WIPP geomechanics program should not need to fund all code development.

2.2. Assessment Problems

Two problems were devised to assess whether the RKPM, Immersed IGA Meshfree method, and CRK method are well suited to the challenges of simulating empty room closure. The teams were instructed to focus on capability demonstration, not intensive code development. Work on any fundamental issues that came to light was deferred to the future. Section 2.2.1 discusses the gradual room closure problem. Section 2.2.2 details changes to the gradual closure geometry to encourage the empty room to collapse. Section 2.2.3 covers the salt material model used in the assessment problems. Section 2.2.4 discusses the viscoplastic scaling technique to allow explicit time integration of the equations of motion.

2.2.1. Gradual Room Closure

This first problem was designed to evaluate how well the meshless methods could reproduce a simplified version of the gradual room closure model historically utilized by Sandia. To be clear, this problem did not include fracturing or roof falls. Sandia ran the simplified gradual room closure problem using the finite element implementation in Sierra/Solid Mechanics (2019), supplied the results to the meshless method teams, who then ran the same problem using their respective RKPM, Immersed Meshfree method, and CRK implementations. The meshless method teams were asked to measure room porosity, discretization convergence, and total run time normalized by the number of processors.

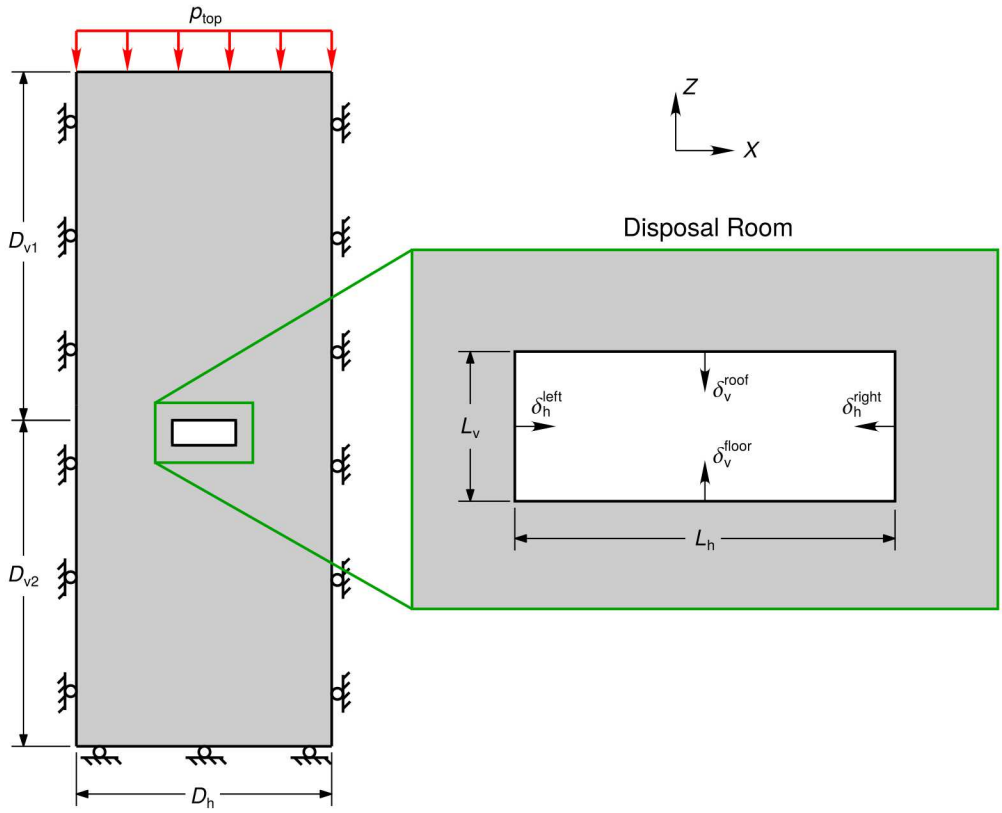

Figure 2-4. Gradual room closure simulation geometry and boundary conditions.

Figure 2-4 depicts the geometry and boundary conditions used in the gradual room closure problem. This setup was chosen to resemble the closure of a lower horizon disposal room, except the stratigraphy was simplified to pure salt. The boundary conditions involved rollers on three sides and a normal pressure of p_{top} = 13.57 MPa at the top. The disposal room's 91.44 m length in the Y-direction (into the page) was assumed to be long enough relative to the height and width of the room to be treated as plane strain. Each disposal panel at the WIPP consists of seven rooms placed 40.54 m apart, east to west. Here, the seven disposal rooms were treated as if they were an infinite array, such that only one disposal room with mirror boundary conditions D_h = 40.54 m apart needed to be modeled. The room ceiling was D_{v1} = 55.30 m and D_{v2} = 51.76 m from the top and bottom of the simulated domain, respectively. Any gas within the room was allowed to

escape without providing back pressure as the room closed. The as-excavated room width and height were $L_h = 10.06$ m and $L_v = 3.96$ m, respectively. The room corners were made square, instead of the actual rounded corners at the WIPP, in order to avoid severe distortions as the room closed. The horizontal displacement of the left wall δ_h^{left} and right wall δ_h^{right} at room mid-height, as well as the vertical displacement of the floor δ_v^{floor} and roof δ_v^{roof} at room mid-width are shown in Fig. 2-4. These were used to define the horizontal and vertical closure of the room as $\delta_h = \delta_h^{left} + \delta_h^{right}$ and $\delta_v = \delta_v^{floor} + \delta_v^{roof}$. The rock mass temperature was spatially uniform at $T = 300$ K.

The Sierra/Solid Mechanics (2019) finite element simulation used Coulomb friction with a friction coefficient of $\mu_s = 0.5$ for sliding contact between salt surfaces, while the meshless simulations assumed sliding between surfaces was frictionless for simplicity. As mentioned in Section 2.1, friction models are not trivial to implement in meshless methods. Fortunately, amount of sliding between surfaces was negligible in the gradual room closure simulations.

The salt surrounding a freshly excavated room has an unknown initial stress state, but one can solve for this stress state at $t = 0$ using various approaches. Sandia's FE and CRK simulations initialized all material points at $t = -10$ ms with a lithostatic stress that varied linearly from p_{top} MPa at the domain top to $p_{bot} = \rho\, g\, (D_{v1} + D_{v2})$ MPa at the domain bottom, where $\rho = 2300$ kg/m^3 and $g = 9.79$ m/s^2. Rather than delete elements to expose the room within the salt, a fluid pressure equal to the lithostatic pressure was applied to the walls of the room at time $t = -10$ ms, and then sinusoidally reduced to zero over 10 ms to simulate a nearly instantaneous room excavation. For $t > 0$ the fluid pressure was held to zero so that the room could naturally close. The IGA Meshfree simulations and RKPM simulations utilized alternative approaches to compute the initial stress state around the room, as discussed in their respective chapters.

Details of the numerical settings used to simulate the problem using the FEM in Sierra/Solid Mechanics (2019) can be found in Appendix A.3.

2.2.2. Room Collapse and Rubble Pile Consolidation

The second problem was designed to test how well the two meshless methods could simulate room collapse and rubble pile consolidation. Room collapse is beyond what can currently be simulated in Sierra/Solid Mechanics (2019), so no reference solution was supplied to the meshless method teams. The meshless method teams were asked to report room porosity, rubble pile shape/dimensions, discretization convergence, and total run time normalized by the number of processors.

The room collapse and rubble pile consolidation problem geometry and boundary conditions are shown in Fig. 2-5. Two differences between Figs. 2-4 and 2-5 are apparent. First, the room collapse problem added a clay seam $L_g = 2.43$ m above the room ceiling. Sandia has historically modeled clay seams as a pair of contacting surfaces, where sliding in the seam plane was captured with Coulomb friction with a $\mu_c = 0.2$ coefficient of friction. Any tensile loading normal to the seam plane caused the surfaces to separate, as seams typically are assumed to have negligible tensile strength. Adding the clay seam encouraged the beam of salt above the room to fracture and fall into the room, similar to the lower horizon roof fall in Fig. 1-3a. Second, the room

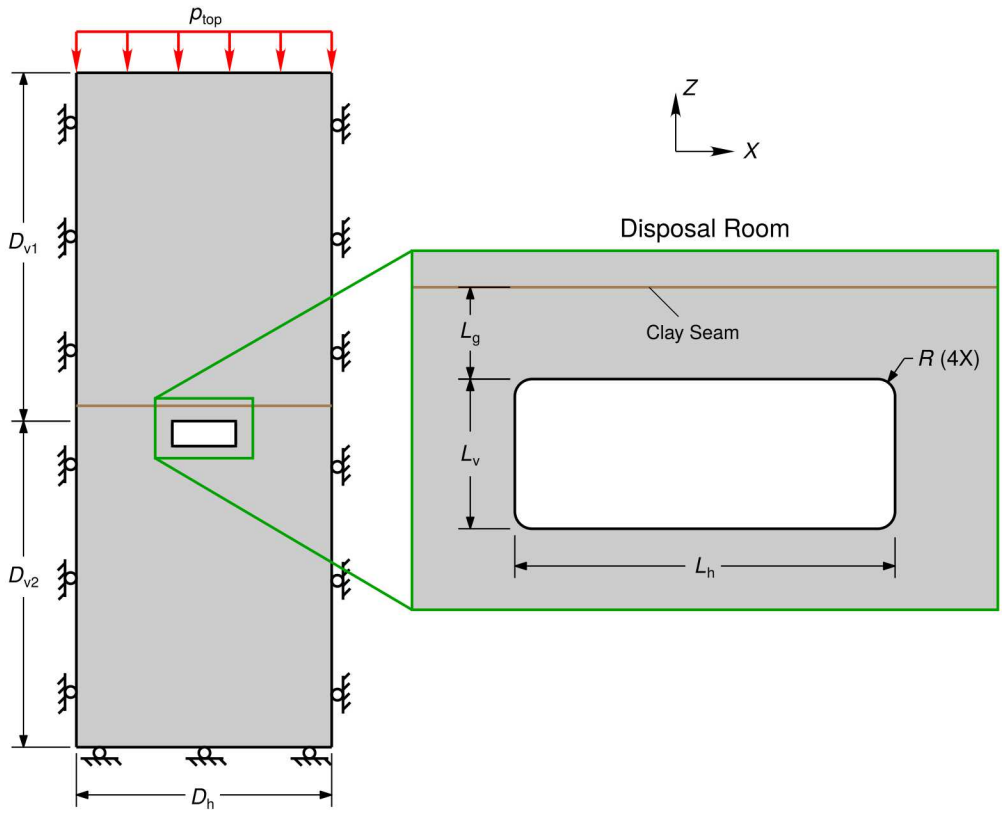

Figure 2-5. Room collapse and rubble pile consolidation geometry and boundary conditions.

collapse problem included rounded corners, each with a $R = 0.457$ m radius, instead of the sharp corners used in the gradual closure problem. The corners were rounded to avoid initiating cracks at a singularity, which would likely be sensitive to the discretization size.

Similar to the gradual room closure simulations, the collapse and reconsolidation simulations assumed sliding between surfaces was frictionless for simplicity. Unlike the gradual room closure simulations, however, the lack of friction in-between pieces of rubble likely reduced the back pressure supplied to the surrounding rock formation. Friction sensitivity studies would probably be a worthwhile area of future work.

The majority of the room collapse simulations utilized the two-dimensional, plane strain, geometry in Fig. 2-5, but the permeability through the plane of a two-dimensional geometry is practically meaningless. Therefore, the meshless method teams were also asked to run a single room collapse and rubble pile consolidation simulation with a room length of 10.06 m in the Y-direction. The discretization size was left up to the discretion of each team, but finer discretizations were, of course, preferred.

2.2.3. Salt Material Model

The salt behavior was simulated using an isotropic, hyperelastic, viscoplastic, continuum damage, model. The material model was designed to capture the essential physical processes, yet remain

relatively simple for numerical method assessment. Accuracy was not of paramount concern. Note that the following presentation follows the geomechanics convention that compressive stresses are positive and tensile stresses are negative. Also note that Section 2.2.3.1 presents the damage portion of the material model, but damage evolution was not permitted in the gradual room closure simulations.

2.2.3.1. Model Formulation

Continuum damage models compute a macroscopic stress tensor $\boldsymbol{\sigma}$, which is used by the momentum balance code, and a Kachanov stress tensor $\hat{\boldsymbol{\sigma}}$, which is typically only utilized inside the model (Kachanov 2013). One typically computes the Kachanov stress as $\hat{\boldsymbol{\sigma}} = \boldsymbol{\sigma}/(1-\omega)$, where $0 \leq \omega \leq 1$ is a scalar measure of damage, such that $\hat{\boldsymbol{\sigma}}$ roughly captures how damage amplifies the macroscopic stress on the remaining, undamaged, microstructure at a material point. The model herein, however, uses a slightly more complex approach to permit different behavior in tension and compression. The macroscopic stress is first decomposed into principal stresses σ_i and principal stress directions $\boldsymbol{e}_i$ as

$$\boldsymbol{\sigma} = \sum_{i=1}^{3} \sigma_i \boldsymbol{e}_i \otimes \boldsymbol{e}_i. \tag{2.1}$$

In this principal stress form, one can then define the Kachanov stress as

$$\hat{\boldsymbol{\sigma}} = \sum_{i=1}^{3} \frac{\sigma_i}{1-\omega_i} \boldsymbol{e}_i \otimes \boldsymbol{e}_i, \tag{2.2}$$

where ω_i is the principal damage corresponding to principal stress σ_i. All three principal damages are equal, unless one or more have exceeded the tensile damage limit ω^{t} or the compressive damage limit ω^{c}:

$$\omega_i = \begin{cases} \min(\omega, \omega^{\mathrm{t}}), & \text{for } \sigma_i < 0 \\ \min(\omega, \omega^{\mathrm{c}}), & \text{for } \sigma_i \geq 0 \end{cases}, \tag{2.3}$$

where ω is the isotropic damage variable when a tensile or compressive limit is not active. This formulation allows the material to reach complete tensile failure while still retaining some resistance to compressive stresses. The model presentation will return to the damage evolution equation after presenting the elastic and viscoplastic behavior.

The model decomposes the total strain rate $\dot{\boldsymbol{\varepsilon}}$ into an elastic strain rate $\dot{\boldsymbol{\varepsilon}}^{\mathrm{el}}$ and a viscoplastic strain rate $\dot{\boldsymbol{\varepsilon}}^{\mathrm{vp}}$:

$$\dot{\boldsymbol{\varepsilon}} = \dot{\boldsymbol{\varepsilon}}^{\mathrm{el}} + \dot{\boldsymbol{\varepsilon}}^{\mathrm{vp}}. \tag{2.4}$$

Dilation strain associated with damage is neglected for simplicity. The elastic behavior utilizes generalized Hooke's law in rate form, which is the following linear relationship between the elastic strain rate $\dot{\boldsymbol{\varepsilon}}^{\mathrm{el}}$ and the stress rate $\dot{\boldsymbol{\sigma}}$,

$$\dot{\boldsymbol{\sigma}} = C : \dot{\boldsymbol{\varepsilon}}^{\mathrm{el}}, \tag{2.5}$$

$$C = (B - 2/3\mu)\boldsymbol{I} \otimes \boldsymbol{I} + 2\mu \mathcal{I}, \tag{2.6}$$

where C is the fourth-order elastic stiffness tensor composed of the bulk modulus B, the shear modulus μ, the second-order identity tensor $\boldsymbol{I}$, and the fourth-order symmetric identity tensor $\mathcal{I}$. Damage likely reduces the elastic stiffness tensor, but this effect was ignored for simplicity.

Viscoplastic deformation of intact salt is isochoric and only occurs in the presence of shear stress. The model utilizes the von Mises stress as its equivalent Kachanov shear stress measure, defined as

$$\hat{\bar{\sigma}} = \sqrt{\tfrac{3}{2}\,\hat{\boldsymbol{\sigma}}^{\mathrm{dev}} : \hat{\boldsymbol{\sigma}}^{\mathrm{dev}}} \tag{2.7}$$

where $\hat{\boldsymbol{\sigma}}^{\mathrm{dev}} = \hat{\boldsymbol{\sigma}} - \hat{p}\,\boldsymbol{I}$ is the deviatoric Kachanov stress tensor and $\hat{p} = \mathrm{tr}(\hat{\boldsymbol{\sigma}})/3$ is the Kachanov pressure. The viscoplastic strain evolves according to an associated flow rule

$$\dot{\boldsymbol{\varepsilon}}^{\mathrm{vp}} = \dot{\bar{\varepsilon}}^{\mathrm{vp}} \frac{\partial \hat{\bar{\sigma}}}{\partial \hat{\boldsymbol{\sigma}}}, \tag{2.8}$$

where $\dot{\bar{\varepsilon}}^{\mathrm{vp}}$ is the equivalent viscoplastic strain rate. For simplicity, the model neglects transient creep and includes only steady-state creep. The expression for steady state creep involves two terms:

$$\dot{\bar{\varepsilon}}^{\mathrm{vp}} = \sum_{i=1}^{2} A_i \left(\frac{\hat{\bar{\sigma}}}{\mu} \right)^{n_i} \tag{2.9}$$

where the variables A_i and n_i are model parameters and $\bar{\varepsilon}^{\mathrm{vp}}$ is initialized to zero.

Many salt models employ the concept of a dilatancy boundary (see, for example, Chan et al. (1998), Günther and Salzer (2012), and Hampel (2015)). Salt responds viscoplastically under the dilatancy boundary (low shear stress and high confining pressure), and responds with a combination of damage, dilation, and viscoplasticity above the dilatancy boundary (high shear stress and low confining pressure). This model includes damage, but neglects dilation for simplicity, so the dilatancy boundary is referred to as the damage boundary. The damage boundary has the following Drucker-Prager form,

$$\hat{\bar{\sigma}}^{\mathrm{db}} = B_2\,(\hat{p} - B_1), \tag{2.10}$$

where B_1 and B_2 are model parameters. A plot of the boundary for $B_1 = -2$ MPa and $B_2 = 1$ is shown in Fig. 2-6.

The damage evolution equation is

$$\dot{\omega} = \frac{D}{\mu} \left\langle \hat{\bar{\sigma}} - \hat{\bar{\sigma}}^{\mathrm{db}} \right\rangle \dot{\bar{\varepsilon}}^{\mathrm{vp}}, \tag{2.11}$$

where D is a material parameter and ω is initialized at zero for intact salt. In words, this expression assumes an increment in damage is proportional to an increment of viscoplastic damage work. Damage can only evolve if $\hat{\bar{\sigma}}$ is above $\hat{\bar{\sigma}}^{\mathrm{db}}$, as reflected by the Macaulay bracket factor $\left\langle \hat{\bar{\sigma}} - \hat{\bar{\sigma}}^{\mathrm{db}} \right\rangle$.

Healing was neglected based on the presumption that any salt inside the rubble pile that experiences high enough pressure and low enough shear stress to heal is unlikely to be subsequently damaged and fracture again.

As discussed further in Chapter 8, the decisions to neglect transient creep (hardening), dilation, healing (damage reduction), and high rate behavior will all likely be revisited in the future.

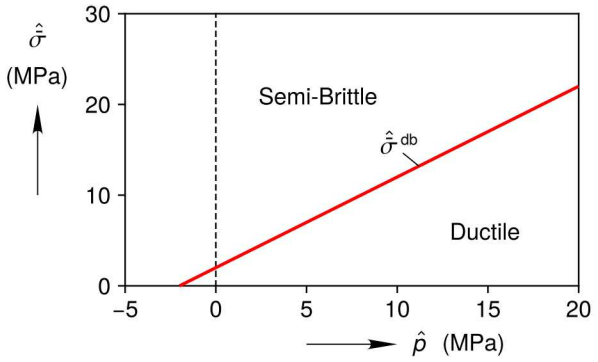

Figure 2-6. Damage boundary.

2.2.3.2. Parameter Values

The parameter values for the gradual room closure problem, the room collapse and rubble pile consolidation problem, and a material model verification test (discussed in the next section) are listed in Table 2-1. The elastic and viscoplastic parameter sets for the gradual closure and collapse problems were chosen based on the elastic and steady-state creep parameters in M-D model Calibration 3B (see Reedlunn (2018a)). Damage evolution was prohibited in the gradual closure problem by setting $D = 0$. The damage parameters in the room collapse problem were selected to resemble damaged salt behavior. To be more specific, the damage boundary parameters B_1 and B_2 were chosen to loosely capture the dilatancy boundary for WIPP salt (Düsterloh et al. 2015); the damage limits ω^t and ω^c were selected to allow the stress to approach nearly zero in tension, yet retain a large percentage of compressive strength; and the damage evolution rate D was chosen to ensure the room roof fell within a few years of room excavation. Accurate numerical predictions of room collapse and rubble pile consolidation will eventually require higher quality parameter selection methods, but the collapse parameters in Table 2-1 should suffice for the numerical method assessment pursued herein.

Table 2-1. Salt model parameter values.

Parameter Type	Parameter	Units	Gradual Closure	Collapse	Verification
Elastic	μ	GPa	12.4	12.4	12.4
	B	GPa	20.7	20.7	20.7
Viscoplastic	A_1	s^{-1}	2.154×10^{-6}	2.154×10^{-6}	1×10^{-2}
	n_1	–	1.595	1.595	2
	A_2	s^{-1}	1.693×10^{9}	1.693×10^{9}	0
	n_2	–	6.279	6.279	0
Damage	B_1	MPa	-2	-2	-2
	B_2	–	1	1	1
	D	–	0	5×10^{4}	3.5×10^{4}
	ω^t	–	0	0.999999	0.999999
	ω^c	–	0	0.5	0.5

2.2.3.3. Analytical Solution for Triaxial Compression Creep

The prevalence and simplicity of triaxial compression creep make it well suited as a material model verification test. In triaxial compression creep, a cylindrical specimen is subjected to a constant radial confining Cauchy pressure σ_{rr} and a constant axial Cauchy stress σ_{zz}, as shown in Fig. 2-7, while measuring the radial logarithmic strain ε_{rr} and axial logarithmic strain ε_{zz}. (Axisymmetric compression is perhaps a more appropriate name for these tests, because the hoop stress $\sigma_{\theta\theta}$ is equal to σ_{rr} and the hoop strain $\varepsilon_{\theta\theta}$ is equal to ε_{rr}, if the material is at least transversely isotropic, but triaxial compression is the common name.)

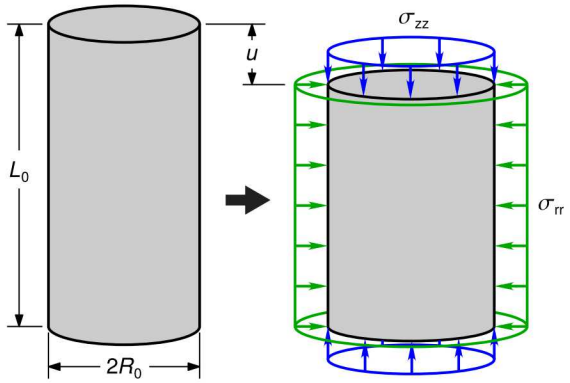

Figure 2-7. Triaxial compression schematic

The model in Section 2.2.3.1 affords an analytical solution under triaxial compression creep if the "Verification" parameter set in Table 2-1 is utilized and if one other condition is met. When the damage has not exceeded the tensile or compressive damage limits ($\omega_i = \omega$), then $\hat{\boldsymbol{\sigma}} = \boldsymbol{\sigma}/(1-\omega)$ and Eq. (2.11) becomes

$$\dot{\omega} = \frac{D}{\mu} \frac{\left\langle \bar{\sigma} - \bar{\sigma}^{\mathrm{db}} \right\rangle}{1-\omega} \dot{\bar{\varepsilon}}^{\mathrm{vp}} \tag{2.12}$$

where $\hat{\bar{\sigma}} = \bar{\sigma}/(1-\omega)$ and $\hat{\bar{\sigma}}^{\mathrm{db}} = \bar{\sigma}^{\mathrm{db}}/(1-\omega)$. When the stress state is held constant, then Eq. (2.12) can be analytically integrated to

$$\omega = 1 - \sqrt{1 - 2D \frac{\bar{\sigma} - \bar{\sigma}^{\mathrm{db}}}{\mu} \bar{\varepsilon}^{\mathrm{vp}}}. \tag{2.13}$$

Provided $n_1 = 2$ and $n_2 = 0$, one can then analytically integrate Eq. (2.9) to obtain

$$\bar{\varepsilon}^{\mathrm{vp}} = \frac{1 - \sqrt{1 - 4A_1 D t \dfrac{\bar{\sigma}^2 \left(\bar{\sigma} - \bar{\sigma}^{\mathrm{db}}\right)}{\mu^3}}}{2D \dfrac{\bar{\sigma} - \bar{\sigma}^{\mathrm{db}}}{\mu}}, \tag{2.14}$$

and utilize Eqs. (2.5) and (2.8) to obtain the total strain as

$$\boldsymbol{\varepsilon} = C^{-1} : \boldsymbol{\sigma} + \bar{\varepsilon}^{\mathrm{vp}} \frac{\partial \bar{\sigma}}{\partial \boldsymbol{\sigma}}, \tag{2.15}$$

where $\partial\bar{\sigma}/\partial\boldsymbol{\sigma} = -1/2\,\boldsymbol{e}_r \otimes \boldsymbol{e}_r - 1/2\,\boldsymbol{e}_\theta \otimes \boldsymbol{e}_\theta + \boldsymbol{e}_z \otimes \boldsymbol{e}_z$.

Plots of this analytical solution, as well as comparisons against numerically computed solutions are shown later in the report (see Sections 4.2.1 and 5.2.1).

2.2.3.4. Triaxial Compression at Constant Strain Rate

Geomechanicians frequently calibrate damage boundary and damage evolution parameters against constant strain rate triaxial compression tests. Although it was not possible to formulate a model capable of capturing such experiments within the time constraints of this project, it is still worthwhile to compare the model given in Section 2.2.3 against constant strain rate experiments.

Düsterloh et al. (2015) and Salzer et al. (2015) performed a large number of constant strain rate experiments on WIPP salt at various temperatures, strain rates, and radial confining pressures. Without delving into the details of the experiments, the results of a few such experiments are reported in Fig. 2-8 in terms of the Cauchy stress difference $\sigma_{zz} - \sigma_{rr}$ vs. the axial logarithmic strain change $\varepsilon_{zz} - \varepsilon_{zz}(t_0)$ from the onset of the constant strain rate application. All four experiments shown in Fig. 2-8 were performed at room temperature and a constant axial engineering (technical) strain rate of $\dot{u}/L_0 = 10^{-6}$ s^{-1}, but different radial Cauchy confining stresses. Some experiments included a brief unloading and re-loading to measure the elastic modulus, but these have been removed to improve legibility. As is commonly observed, larger values of σ_{rr} produce a greater stress difference $\sigma_{zz} - \sigma_{rr}$, at a given $\varepsilon_{zz} - \varepsilon_{zz}(t_0)$. (The small deviations from this trend are likely due to specimen-to-specimen variation.)

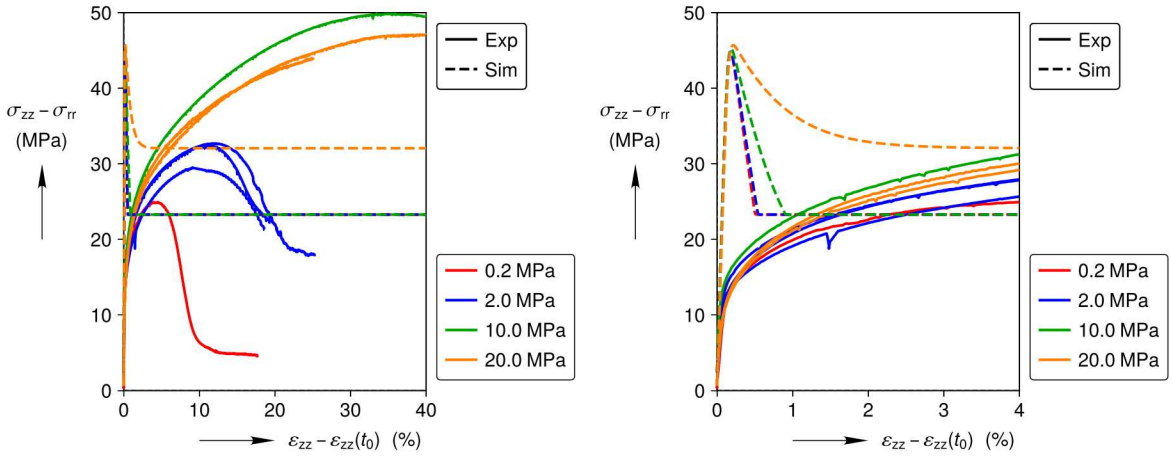

(a) Large strain behavior **(b) Small strain behavior**

Figure 2-8. Constant strain rate tests and model predictions at room temperature, a constant strain rate of 10^{-6} s^{-1}, and four different radial confining stresses.

As expected, the model poorly predicts the experiments in Fig. 2-8. (A short description of the model implementation used to generate the simulated results is given in Section 5.2.1.) The model predicted stress difference shoots up to a maximum of $\sigma_{zz} - \sigma_{rr} \approx 45$ MPa, well above the

measurements, at $\varepsilon_{zz} - \varepsilon_{zz}(t_0) \approx 0.2$ %. By omitting transient strain, the model behaves as if the material is fully hardened from the onset of the test. Had the material began in an unhardened state, $\sigma_{zz} - \sigma_{rr}$ would have risen more gradually with axial strain. After the peak at $\varepsilon_{zz} - \varepsilon_{zz}(t_0) \approx 0.2$ %, $\sigma_{zz} - \sigma_{rr}$ decays by different amounts due to damage accumulation. For $\sigma_{rr} = 20$ MPa, the stress difference stops evolving for $\varepsilon_{zz} - \varepsilon_{zz}(t_0) > 4$ % because $\hat{\bar{\sigma}}^{vp} = \hat{\bar{\sigma}}^{db}$. For the smaller σ_{rr} values, the stress difference stops evolving because $\omega = \omega^c$. Future efforts will likely focus on adding hardening and properly calibrating the damage evolution.

2.2.4. Viscoplastic Scaling

All three meshless method implementations investigated herein explicitly integrated the momentum balance equations. Explicit time integration requires a very small time step, typically on the order of 1 μs, for numerical stability. This makes explicit time integration well suited to simulating short duration events, such as car crashes, but anything that lasts longer than a few seconds is not practical. Rather than ask the meshless method teams to implement implicit time integration algorithms, we elected to use viscoplastic strain rate scaling to squeeze hundreds of years into a few seconds.

The notion of scaling the visocoplastic strain rate can be made more precise with a few definitions. Define the physical time as t, the momentum balance time utilized by the explicit time integration algorithm as t^{mb}, and the equivalent viscoplastic strain as $\bar{\varepsilon}^{vp}$. The viscoplastic scale factor $s = s(t^{mb})$ is defined as

$$s = \frac{\dfrac{\mathrm{d}\bar{\varepsilon}^{vp}}{\mathrm{d}t^{mb}}}{\dfrac{\mathrm{d}\bar{\varepsilon}^{vp}}{\mathrm{d}t}} = \frac{\mathrm{d}t}{\mathrm{d}t^{mb}}, \tag{2.16}$$

so one can calculate the current time from the scale factor history as

$$t = \int_{t_i^{mb}}^{t^{mb}} s \, \mathrm{d}\hat{t}^{mb} + t_i, \tag{2.17}$$

where t_i and t_i^{mb} respectively are the physical and momentum balance time at the start of the time period of interest.

The viscoplastic rate scaling had to be fast enough to reach the final container configuration in a reasonable amount of run time, but not so fast that inertial effects significantly altered the predictions. As documented in Section 2.3.2 and A.2.1 of Reedlunn et al. (2019), a viscoplastic rate scaling profile was selected by comparing explicit dynamic simulations of gradual room closure against a reference implicit quasi-static simulation. Successively slower s vs. t^{mb} profiles were compared to find the profile that approximated the quasi-static solution, yet still ran relatively quickly. The profile of the form

$$s = s_0 + s_1 \, t^{mb}, \tag{2.18}$$

where s_0 and s_1 are user defined constants, proved satisfactory since the room closes fastest immediately after excavation and slows down over time. Values of $s_0 = 10^{-2}$ and $s_1 = 2 \times 10^9$ s^{-1}

produced room closures that matched the quasi-static closure quite well, while $s_0 = 10^{-2}$ and $s_1 = 2 \times 10^{10}$ s^{-1} caused errors of about 5 % at $t = 50$ yr, but the errors largely disappeared once the ceiling touched the floor. The meshless method chapters each briefly mention their respective viscoplastic rate scaling settings, while Appendix A.3 covers the viscoplastic scaling utilized in the finite element simulations.

3. IMMERSED ISOGEOMETRIC ANALYSIS MESHFREE SIMULATIONS OF EMPTY ROOM CLOSURE

Authors: Georgios Moutsanidis[‡] and Yuri Bazilevs[‡]

3.1. Introduction

In the present work, we adapt an immersed framework, proposed and developed in Bazilevs et al. (2017b) and Bazilevs et al. (2017a) for air-blast fluid-structure interaction (FSI) applications, to carry out open-room closure simulations. The framework makes use of two discretizations, referred to as background and foreground meshes or grids. A fixed background Eulerian grid provides the basis functions for the approximation of the solution of the governing differential equations in the weak form. In the case of FSI, the background grid is responsible for producing a discrete velocity solution for the coupled system of equations. In the absence of a fluid (or gas), as in the present application, only the equations of solid mechanics are solved using the background mesh, which makes the resulting numerical formulation similar to a well-known material-point method (Sulsky et al. 1994). One of the distinguishing features of our approach is to use smooth (i.e., higher-order continuous) B-Spline functions, as in Isogeometric Analysis (IGA) (Hughes et al. 2005), for the background discretization. This additional smoothness renders the strain-rate approximation continuous across the elements of the background mesh and, as a result, naturally removes the well-known cell-crossing instability of classical material-point methods.

In the immersed formulation adapted to the open-room closure problem, the foreground grid presents a collection of Lagrangian particles that track the position of the solid object, store the history-dependent variables of the creep and damage models employed, and act as integration (or quadrature) points for the underlying variational form of the solid mechanics equations discretized on the background mesh. In more advanced versions of the framework we associate a meshfree (i.e., RKPM (Chen et al. 1996)) discretization to this collection of material particles, and use this discretization to approximate the solution of a phase-field equation governing the fracture behavior of the solid (Kamensky et al. 2018; Moutsanidis et al. 2018), however such regularization was not applied in the present work.

Finally, to treat the volumetric locking phenomena associated with the incompressible nature of plastic deformations (in this case, creep is modeled as plastic flow), we employ the $\overline{\boldsymbol{F}}$ approach recently developed in Moutsanidis et al. (2019) for the present immersed IGA-meshfree framework. Here, the dilatational strain rate is projected onto a lower-order function space to

[‡]School of Engineering, Brown University, 184 Hope Street, Providence, RI 02912, USA

reduce the number of dilatational constraints, and thus improve the quality of the pressure solution.

In all the immersed IGA-meshfree calculations presented, the background mesh makes use of C^1-continuous quadratic B-splines, and the dilatational strain rate is projected onto C^0-continuous linear B-Splines (equivalent to linear quadrilateral or hexahedral FEM). About three foreground Lagrangian particles per background-element parametric direction are employed in the calculations.

All simulations utilize the viscoplastic rate scaling described in Section 2.2.4 in order to squeeze hundreds of years into seconds. The initial viscoplastic scale factor is $s_0 = 10^{-2}$ in all cases, but different simulations utilize different values for the scaling ramp rate s_1, as noted in the sections below.

In addition, all simulations initialize material points at time $t = 0$ with a lithostatic stress state that varies linearly from $p_{\text{top}} = 13.57$ MPa at the domain top to $p_{\text{bot}} = 15.97$ MPa at the domain bottom. A simulation domain with a room and a lithostatic stress state, however, is not in static equilibrium. These out of balance stresses cause mechanical waves to travel through the simulation domain from the start of the simulation. Fortunately, the viscoplasticity of the salt cause the waves to quickly dissipate, because the viscoplastic strain rate factor s begins scaling up at $t = 0$.

3.2. Two-Dimensional Room Closure

First, we compute the room closure in two dimensions. We take advantage of the symmetric nature of the problem, and only half of the specimen is modeled. The boundary conditions are specified in Fig. 2-4, while symmetry conditions are applied along a vertical line of symmetry between the left and right sides of the domain.

3.2.1. Prototyping in FEniCS

In order to prototype our analysis model and quickly test different scenarios associated with the constitutive routines, we used a Lagrangian approach implemented in the open source finite element automation software FEniCS (Logg et al. 2012) and in combination with a newly developed nonlocal frictionless peridynamics-like contact model (Kamensky et al. 2019) to enforce contact at closure. FEniCS allows symbolic specification of variational problems in Unified Form Language (UFL) (Alnæs et al. 2014). These specifications are then compiled (Kirby and Logg 2006) into efficient routines suitable for high-performance simulations using the solver DOLFIN (Logg and Wells 2010). FEniCS performs the linearization automatically for implicit time integration. Triangular elements are used to discretize the problem in the mixed form. Continuous piece-wise quadratic approximation is employed for the kinematic variables, discontinuous piece-wise linear approximation is employed for the stress variable, and discontinuous piece-wise constant discretization is employed for the damage variable. It should be noted that FEniCS allows specification of a large variety of element types for different fields in

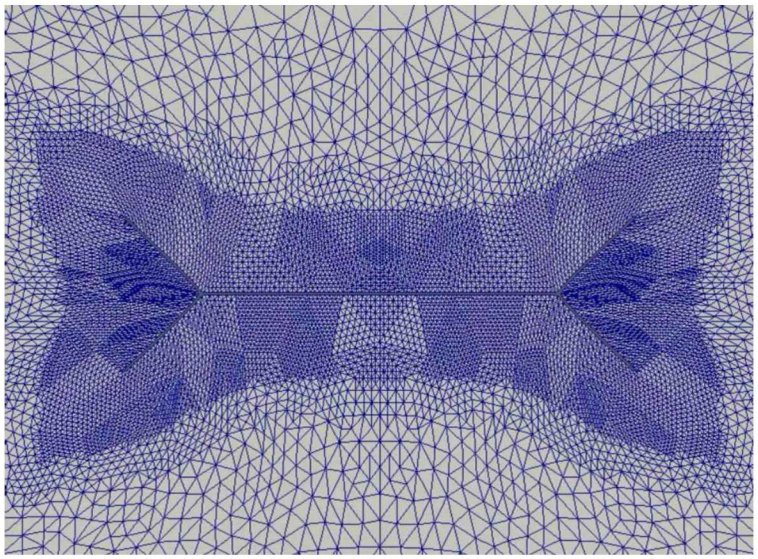

Figure 3-1. 2D room closure. Final configuration. Results with FEniCS.

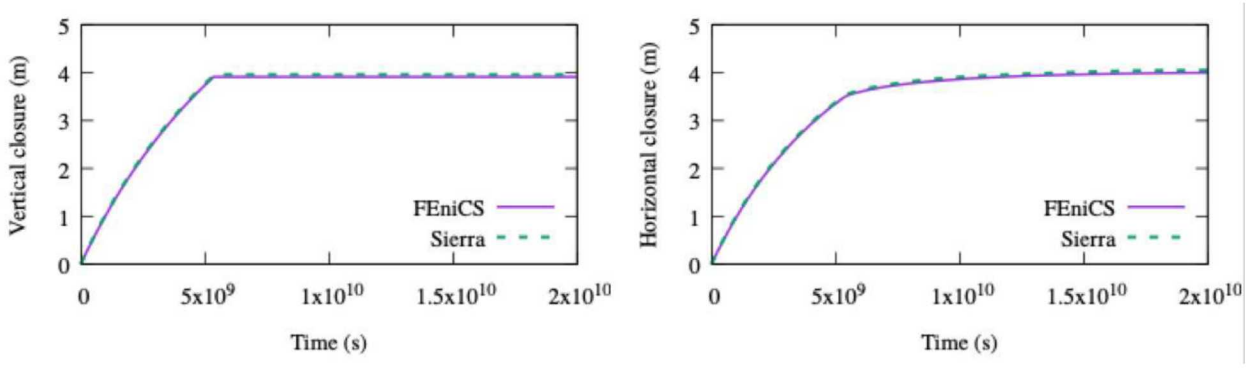

Figure 3-2. 2D room closure. Time evolution of vertical and horizontal closures for the Lagrangian computation compared against the Sierra computation.

the variational formulation in a simple manner. We employ the viscoplastic rate scaling described in Section 2.2.4 with a ramp rate of $s_1 = 2 \times 10^{10}$ s^{-1}. We also employ an implicit Euler method for time integration, for both the equations of motion and the constitutive model.

The constitutive model of Section 2.2.3.1 was used, and the input parameters are those specified in the "Gradual Closure" column of Table 2-1.

The final configuration of the two-dimensional room closure problem is shown in Figure 3-1, while the time evolution of the vertical and horizontal closures along with the Sierra results are provided in Figure 3-2. Excellent agreement between the FEniCS and the Sierra results is observed, suggesting the constitutive model was implemented correctly.

3.2.2. Immersed-Meshfree Analysis

After having figured out most of the issues related to the setup and the constitutive model via prototyping in FEniCS, we employ our immersed-meshfree framework to solve the room closure problem. The background domain has the same dimensions as the the foreground domain and, as a result, the boundaries of the background mesh are conforming to the boundaries of the foreground mesh. We consider three discretizations, labeled MN, at refinement levels $N = 1, 2, 3$. M1 has $13,400$ background elements and $64,600$ particles. M2 has $53,600$ background elements and $258,600$ particles. M3 has $214,400$ background elements and $1,033,800$ particles. We again employ a viscoplastic rate scale factor ramp rate of $s_1 = 2 \times 10^{10}$ s^{-1}.

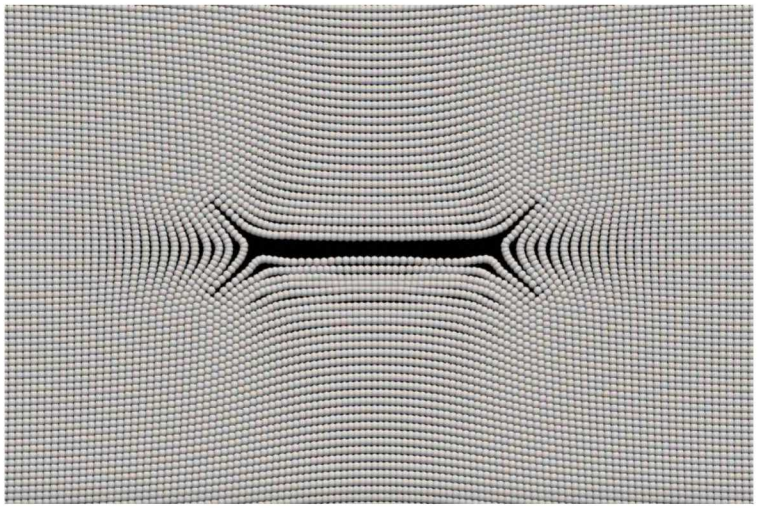

(a) Discretization M1.

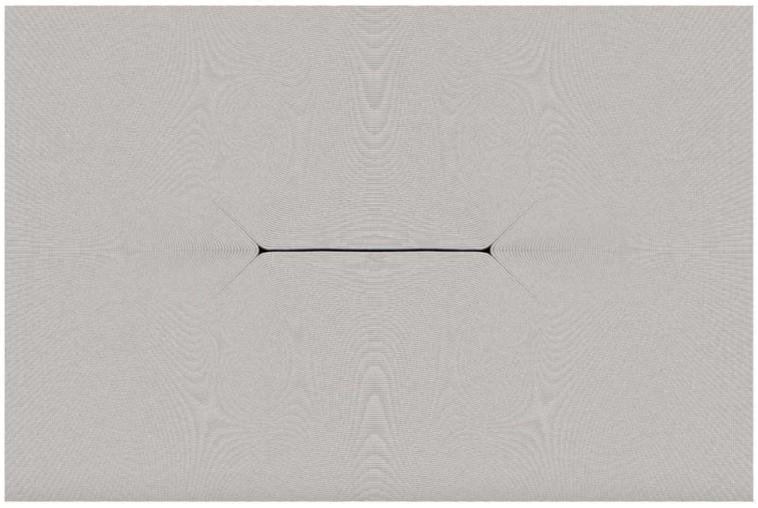

(b) Discretization M3.

Figure 3-3. Immersed 2D room closure. Final configuration for two different discretizations.

The final configuration for discretizations M1 and M3 can be seen in Figures 3-3a and 3-3b, respectively. As can be seen, there is a small gap between the floor and ceiling of the room. This is a result of the implicit contact present in the immersed-meshfree method under consideration

and, as can be seen, it reduces under mesh refinement. Curiously, the gap between the left/right side and the floor/ceiling of the room is far less than the gap between the floor and ceiling. Opposite sides of the closure at the left/right side and the floor/ceiling move at a much smaller relative velocity which reduces the amount of contact force and facilitates closure. In contrast, the floor and the ceiling move at a rather large relative velocity towards each other, and as a result the contact forces do not allow for full closure.

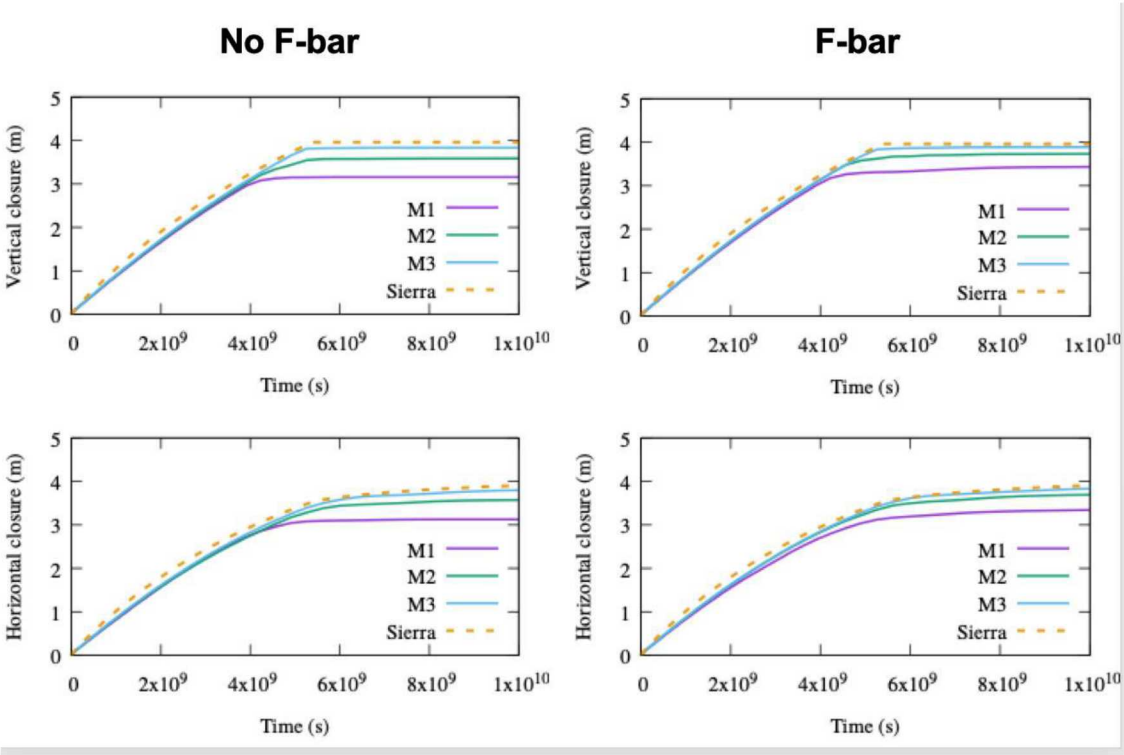

Figure 3-4. Immersed 2D room closure. Time evolution of vertical and horizontal closures for the three discretizations compared against the Sierra computation.

The time evolution of the vertical and horizontal room closures for the three discretizations can be seen in Figure 3-4. The Sierra results (see Appendix A.3) are also cited for comparison purposes. As can be seen, the immersed-meshfree results converge to the Sierra results under mesh refinement. Furthermore, the results improve with the use of the $\overline{\boldsymbol{F}}$ technique. This is expected since significant volumetric locking occurs if no treatment of near-incompressibility takes place, something which is more pronounced in the coarse disretization case.

We have also performed a scalability study to access the performance of the parallel implementation of our code. The strong scaling results for the coarse and fine discretizations are depicted in Figures 3-5a and 3-5b, respectively. The results are in terms of wall time per unit momentum balance time, and not physical time. The stable time step for the finest discretization is 2.5×10^{-5} and the total computation time is about 30 hr when 48 processors are used.

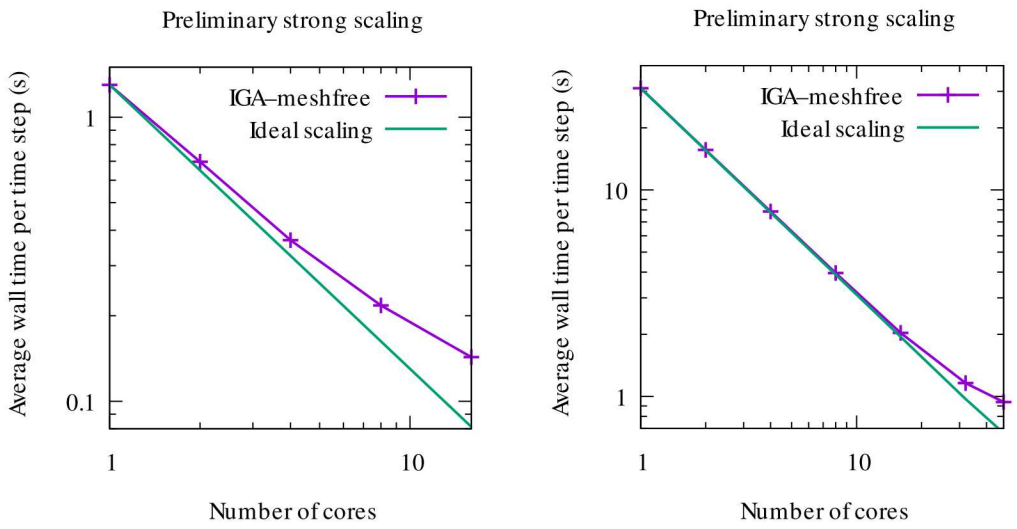

(a) Discretization M1 **(b) Discretization M3**

Figure 3-5. Immersed 2D room closure strong scaling.

3.3. Two-Dimensional Roof Fall

We carry out the roof fall calculations using the salt model parameter set in the "Collapse" column of Table 2-1. This parameter set includes elasticity, viscoplasticity, and damage. The model in Section 2.2.3 was implemented for damage and the damage ODE was integrated explicitly in time. The constitutive model implementation was not verified against an analytical solution as was done in Sections 4.2.1 and 5.2.1.

In order to drive the cracks to the roof and initiate a roof fall we also model a clay seam as shown in Figure 3-6. The clay seam is modeled as a continuum layer of salt, whose bulk and shear moduli in Table 2-1 are reduced by a factor of 10^{-4}. We found this level of stiffness reduction necessary to drive the cracks above the roof. The clay seam was initialized with $\omega = 0.9$ and lithostatic pressure at the start of the simulation. As will be shown later, the final results and collapse patterns are somewhat sensitive to the choice of clay-seam thickness.

3.3.1. Prototyping in FEniCS

As in the smooth room closure case, we first perform some prototyping in FEniCS. The results can be seen in Figure 3-7. The formulation is capable of capturing cracks on the roof top that travel towards the clay seam, as well as tensile cracking at the roof center. The computation does not advance more beyond this point due to element distortion and lack of nonlinear convergence. Nevertheless, enough experience was gained to translate the code implementation to the immersed framework.

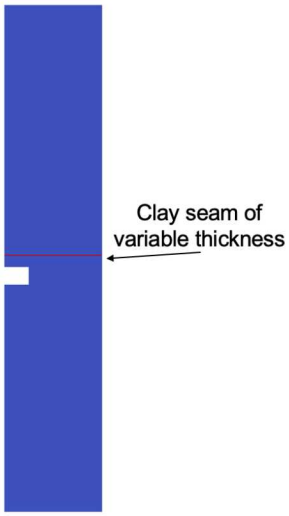

Figure 3-6. 2D roof fall. Clay seam.

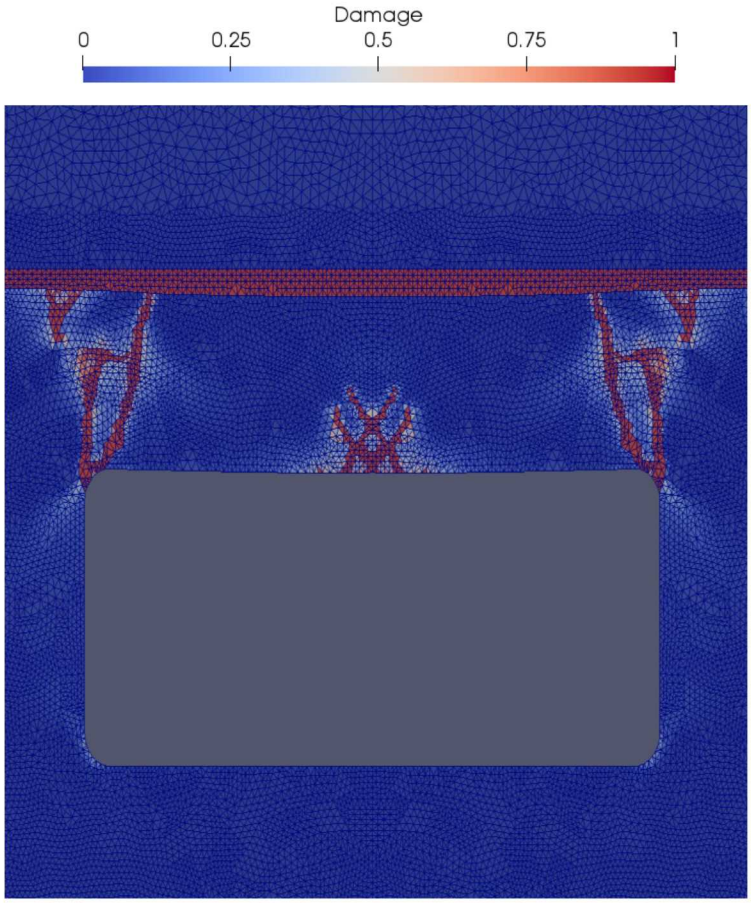

Figure 3-7. 2D roof fall. Results with FEniCS at 0.1 yr. Red - failed material; Blue - intact material.

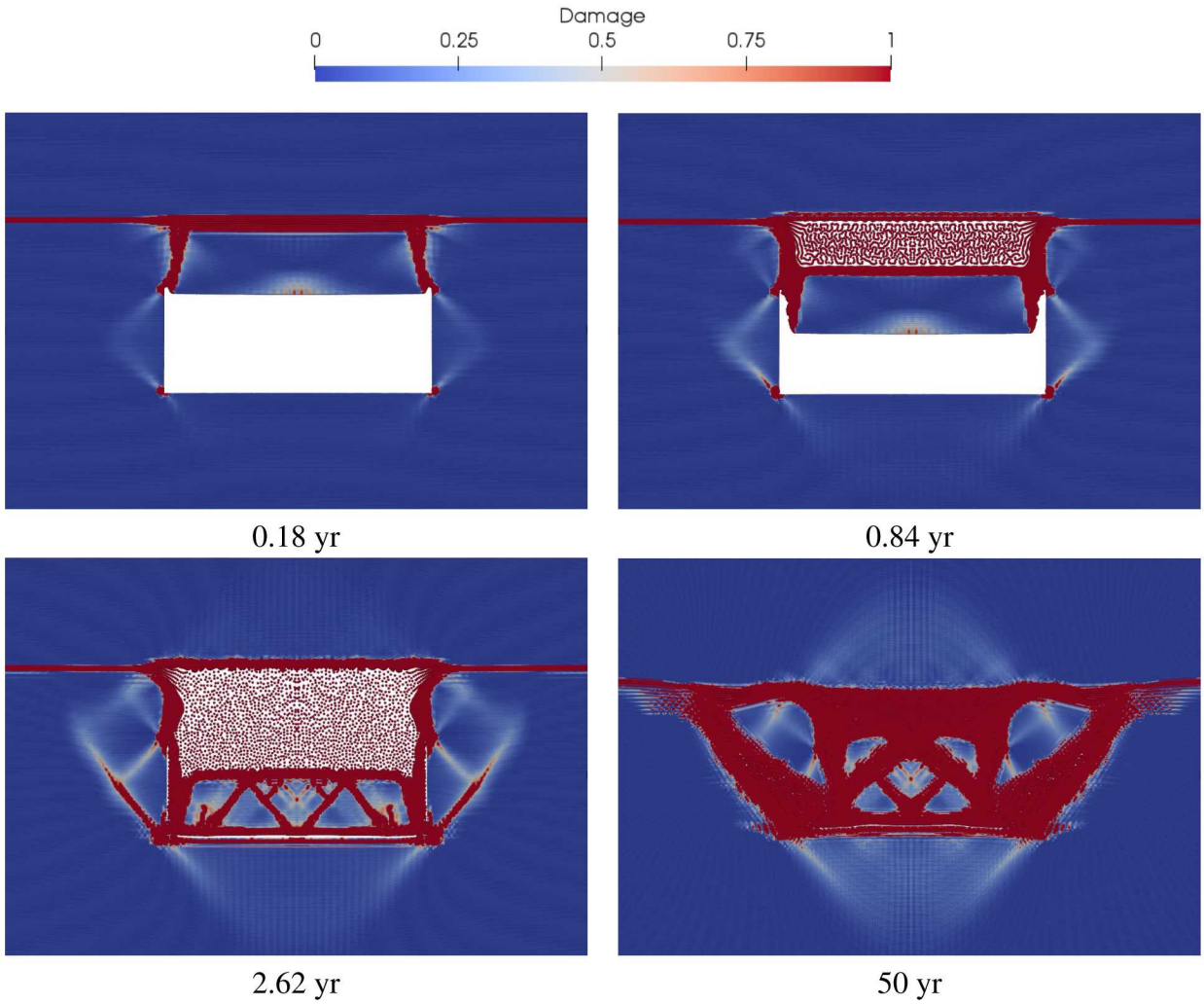

(a) Clay seam of initial thickness of 0.18 m.

Figure 3-8. Immersed 2D roof falls with two different clay seam thicknesses. Roof fall and evolution of damage until closure. Red - failed material; Blue - intact material.

3.3.2. Immersed-Meshfree Simulations

We perform the same roof-fall calculations using the immersed-meshfree framework. We employ a discretization with 214,400 background elements and 1,929,600 particles and we use a viscoplastic rate scale factor ramp rate of $s_1 = 2 \times 10^9$ s^{-1}. The simulation time until the full room closure is about 50 hr over 48 processors. We use two versions of the clay seam, one with thickness of 0.18 m and one with thickness of 0.15 m. The damage evolution and roof collapse for the two cases can be seen in Figures 3-8a and 3-8b. Although the roof seems to be falling somewhat faster than the free fall speed due to the elastic unloading of the weak clay seam, it can be seen that our framework is capable of capturing the fall without running into numerical issues, such as element inversions, as in pure Lagrangian FE-based approaches. Furthermore, it is observed that the immersed formulation predicts the fracture of a large falling roof block into smaller boulders, and, in addition, has no issues handling the subsequent room closure. The

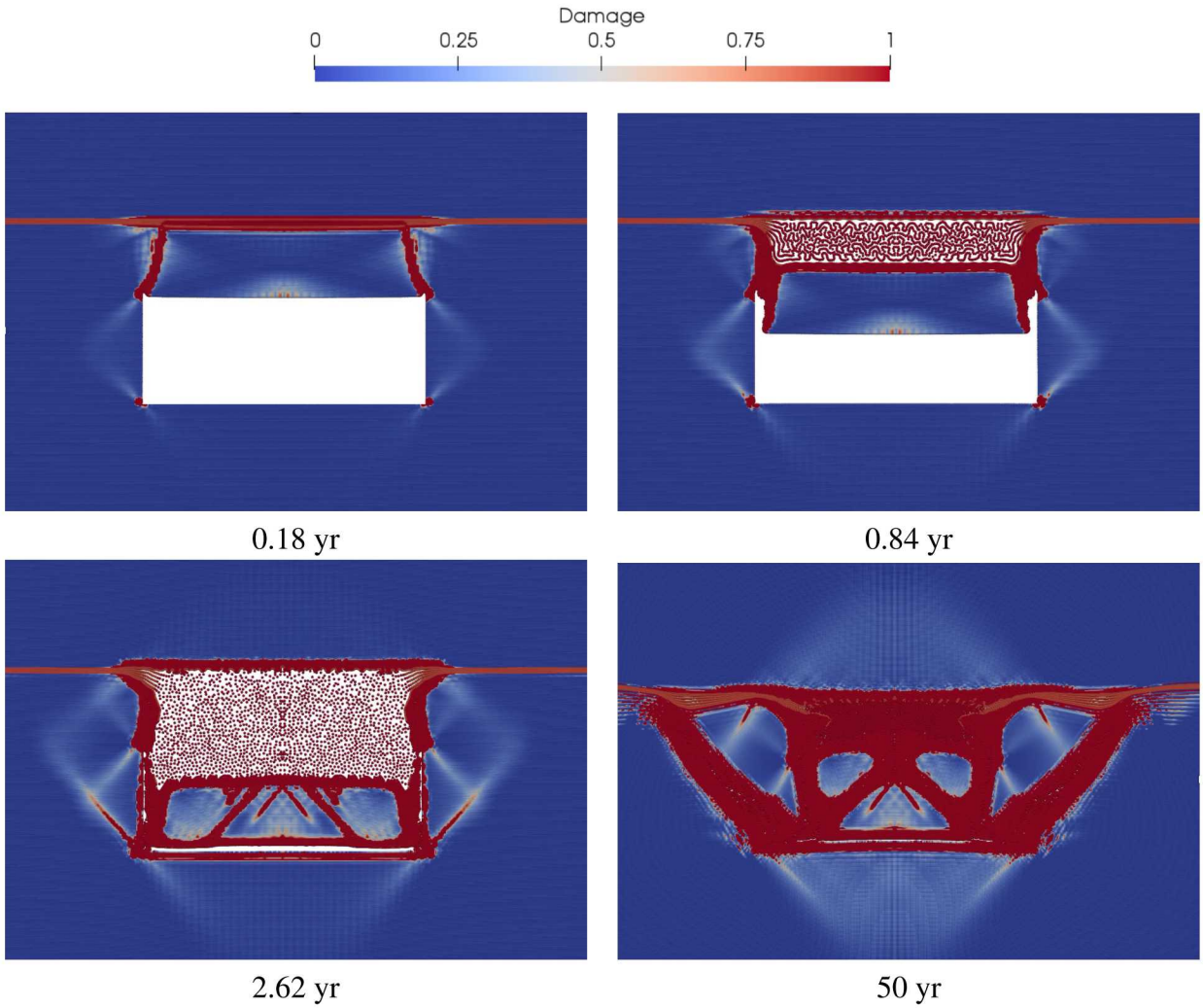

(b) Clay seam of initial thickness of 0.15 m.

Figure 3-8. (Continued) Immersed 2D roof falls with two different clay seam thicknesses. Roof fall and evolution of damage until closure. Red - failed material; Blue - intact material.

computations run to completion in a robust fashion and without divergence due to numerical instabilities.

The free fall time is in the order of 1 sec and the block in our computation falls in about 0.5 sec. This discrepancy is attributed to the elastic unloading of the clay seam that adds additional push to the material beneath it. We would also like to emphasize on the fact that the viscoplastic scaling was not slowed down during the roof fall, and as a result 1.66 yr of time passed while the block was falling. It should also be pointed out that during the fall there are no external forces acting on the block, and as a result creep does not grow. Therefore, we speculate that the behavior of the block during the fall is the same whether the viscoplastic rate is scaled down or not. In addition, not having slowed down the viscoplastic scaling during impact caused the damage to grow in the block $s = 4.1 \times 10^8$ times faster than it would have had $s = 1$ been enforced, since Eq. (2.11) has $\dot{\bar{\varepsilon}}^{\text{vp}}$ in it.

As mentioned before, the particles have some compressive residual stiffness and are not completely damaged in compression. In addition, in an immersed-particle computation like the present one, the particles communicate with each other through the background grid. As a result, the particles are not able to fully separate from each other and along with the presence of the residual compressive strength, we observe an artifact of damaged particles floating around. We do understand that this phenomenon is unphysical, however, we would like to point out that it does not really affect the outcome of the computation and it will probably go away with a more elaborate clay seam model.

It can be seen that the thicker clay seam produces more cracks in the block and more damage overall. This is expected since thicker clay seams unload and push the salt block downward more severely than thinner seams. This highlights the fact that the clay seam model can affect the subsequent behavior of the falling block.

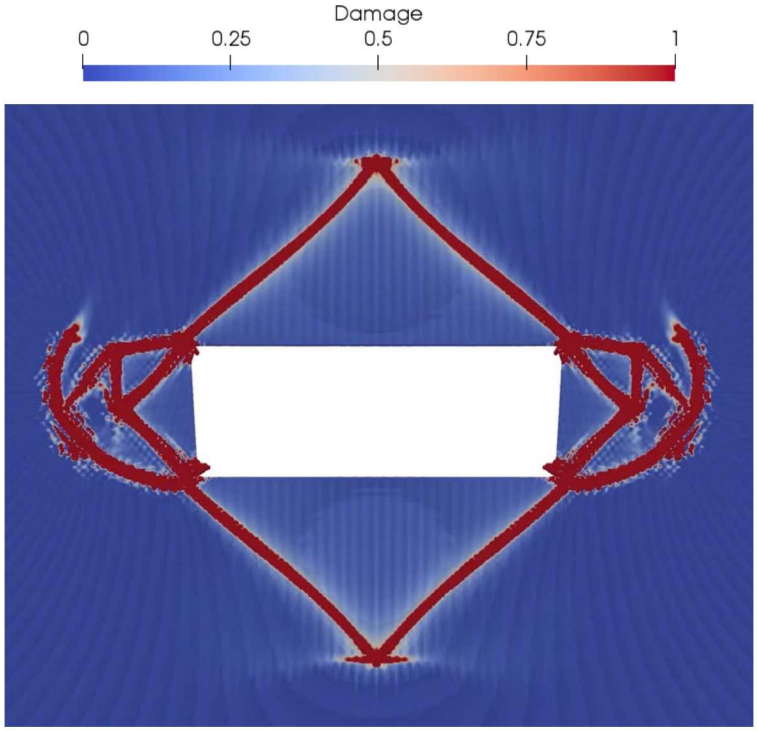

Figure 3-9. Immersed 2D roof fall at 2 yr without modeling the clay seam. Red - failed material; Blue - intact material.

In order to highlight even more the importance and sensitivity of the clay seam modeling, we also provide the results of a computation without the presence of the clay seam in Figure 3-9. As can be seen, the cracks form at an angle of about 45° relative to the room roof, compared to the simulations with the clay seam where the cracks form at about 75°. We attribute this difference to the elastic unloading of the clay seam pushing down on the beam of salt above the room in Fig. 3-8. Recall that the stresses in the clay seam were initialized to be lithostatic, not zero, and the stresses were not allowed to reach equilibrium before scaling up the viscoplastic strain rate. It is possible that had we allowed the stresses to reach equilibrium, the compressive stresses in the clay seam would have relaxed, and cracks with an angle closer to 45° would have formed.

3.4. 3D Smooth Room Closure

Here we present a first attempt at 3D room closure in order to demonstrate the framework's capability to handle large three-dimensional computations with relative ease. We extrude the geometry in the third direction in such a way to mimic the geometry in the horizontal direction. We employ a discretization of 100,000 background elements and 3,000,000 particles, and we use viscoplastic rate scale factor ramp rate of $s_1 = 2 \times 10^{10}$ s^{-1}. The final configuration can be seen in Figure 3-10a. Again, it can be seen that there is a gap between the surfaces of the room. This is reasonable since the discretization under consideration is relatively coarse and the implicit nature of contact in the present immersed-meshfree framework is tied to the quality of the discretization. As shown in the 2D case, the gap is expected to vanish under mesh refinement. We would like to point out that the presented 3D results serve the sole purpose of demonstrating our framework's capabilities and show that full 3D computations are within reach.

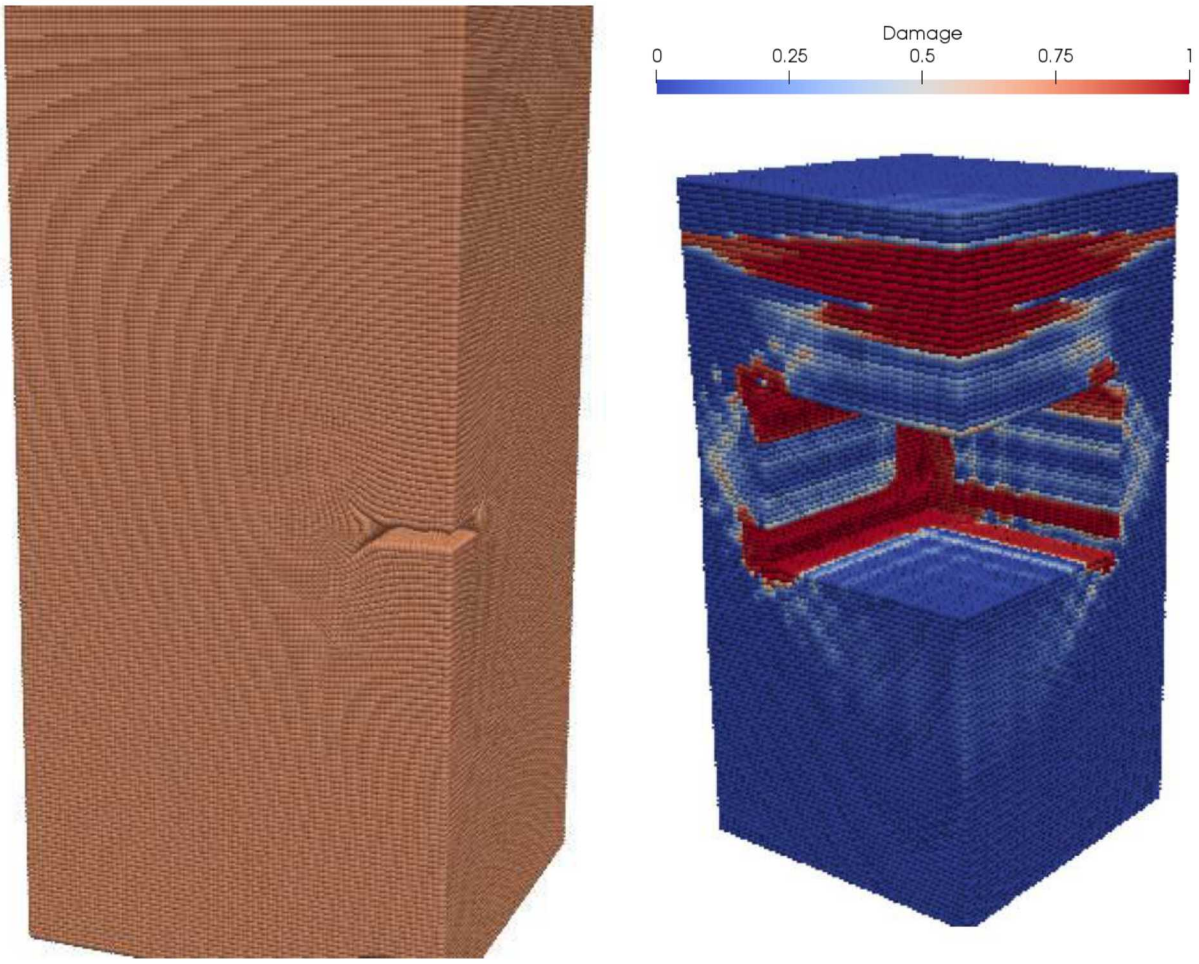

(a) 3D room closure at 190 yr.

(b) 3D roof fall at 1.7 yr. Red - failed material; Blue - intact material.

Figure 3-10. Preliminary 3D results.

Although an elaborate scalability study for the 3D cases was not performed, we would like to

point out the following:

- The stable time step for the current discretization is 5×10^{-5} while the wall time per momentum balance time is 10 sec when 48 processors are used.
- The wall time per momentum balance for a similar quality 2D discretization (discretization M1) is about 0.2 sec when 8 processors are used. This difference in the wall time per momentum balance is attributed to the fact that the 2D computation contains significantly fewer particles per processor, as well as to the fact that the number of operations per particle is increased by a factor of 3 in the 3D case.
- The wall time per momentum balance for a similar in size 2D computation (discretization M3) is about 1 sec when 48 processors are used. The difference between that 2D case and the present 3D case is the number of particles per processor (3× more in the 3D case) and the number of operations per particle (3× more in the 3D case).
- It can be inferred from the above that for the same number of particles and processors, the 3D computations are about 3× more expensive than the 2D ones, due to the extra number of operations per particle.

3.5. Three-Dimensional Roof Fall

Finally, we present our first attempt to simulate a three-dimensional roof fall. We employ a discretization of 900,000 background elements and 25,000,000 particles, and we use the viscoplastic rate scale factor of 2×10^{10}. The computation was run using 150 processors for about 40 hr. Due to excessive queue wait times on the high-performance computing cluster being used, the computation has not reached the end at the time this report is being compiled. However, preliminary results can be seen in Figure 3-10b, where the damage contours around the room are depicted. We would like to emphasize that the 3D results are preliminary and mainly serve the purpose of demonstrating capability. More complete 3D computations are left for future work.

3.6. Conclusions and Observations

The following conclusions and observations can be made:

- Immersed isogeometric-meshfree framework provides a good methodology for open room creep closure, with convergent quantities of interest for smooth closure.
- Near-incompressibility, arising due to the presence of large inelastic deformations, is addressed by means of a recently developed $\overline{\boldsymbol{B}} / \overline{\boldsymbol{F}}$ approach for immersed methods.
- Good parallel scaling is achieved for the immersed isogeometric-meshfree technique, which is important for larger, 3D problems. Current implementation can bring the speed of execution to about 0.1 s per time step. Further improvements can be achieved in several ways, such as using fully explicit time integration (the current generalized-α implementation performs three iterations per time step), improving the quadrature rule and

hence use fewer particles per background cell, and employing sophisticated mesh refinement approaches around the areas of interest (the current implementation uses uniform background and foreground discretizations).

- FEniCS is a good "prototyping" tool for various developments related to open-room closure, including constitutive modeling, non-local formulations, time scaling, etc.
- Clay seam modeled as a layer of softer material promotes roof fall. Roof falls as a single block and breaks up into smaller boulders. As the room continues to close, damage grows somewhat rapidly and tends to produce quite a bit of additional dilatancy after the roof fall. Smaller rocks are "ground away" by the surrounding moving "failed" material due to the remaining compressive strength.

3.7. Future Directions

3.7.1. Non-Local Damage Model

The current damage model being used belongs to the category of the so-called "local damage models". These models are well-known to exhibit a variety of shortcomings that emanate from the loss of ellipticity or hyperbolicity of the continuous problem, and lead to unrealistic damage patterns, stress oscillations, and non convergent results under mesh refinement (Peerlings et al. 2002). Various remedies have been proposed, including gradient-enhanced damage models (Peerlings et al. 1996) and phase-field approaches (Miehe et al. 2010). Peerlings et al. (1996) suggest driving damage with a smoothed strain, viz. $\tilde{\epsilon}$ such that

$$(\tilde{\epsilon} - \epsilon) - l_{nl}^2 \nabla^2 \tilde{\epsilon} = 0, \tag{3.1}$$

where l_{nl} is the non-local length scale parameter set by the user. Using Eq. (3.1) as our point of departure, we suggest driving damage with a smooth effective stress $\bar{\sigma}^{eff}$, viz. find smoothed stress $\tilde{\bar{\sigma}}^{eff}$ such that

$$(\tilde{\bar{\sigma}}^{eff} - \bar{\sigma}^{eff}) - l_{nl}^2 \nabla^2 (\tilde{\bar{\sigma}}^{eff}) = 0 \tag{3.2}$$

The above Partial Differential Equation (PDE) is an elliptic one, and although is it well suited for implicit time integration, it becomes problematic with the explicit time integration we use in the present work. Therefore, we suggest converting the elliptic stress-smoothing problem into a hyperbolic PDE that can now be discretized explicitly in time:

$$\rho_\sigma \ddot{\tilde{\sigma}} + D_\sigma \dot{\tilde{\sigma}} - l_{nl}^2 \nabla^2 (\tilde{\sigma}) + (\tilde{\sigma} - \sigma) = 0 \tag{3.3}$$

We need to choose a speed, c, that gives a tractable Courant-Friedrichs-Lewy (CFL) condition. We also need to choose an appropriate ρ_σ such that information propagates at speed c:

$$\rho_\sigma = l_{nl}^2 / c^2 \tag{3.4}$$

We finally need to choose a damping coefficient D_σ to avoid oscillatory/wave-like behavior of the smoothed stress:

$$D_\sigma \geq 2\sqrt{\rho_\sigma} \tag{3.5}$$

The described approach is similar to Moutsanidis et al. (2018), where an elliptic problem that describes the evolution of phase-field is converted into a hyperbolic one, and is expected to perform well in explicit analyses.

3.7.2. Time Scaling

One crucial factor in the above-mentioned framework is the use of the so-called viscoplastic rate scale factor that speeds up the evolution of the creep model. Although this approach is suitable for events taking place over the course of hundreds or thousands of years, clearly it can become problematic in very short duration events, such as the roof fall that takes about a second. In addition, time scaling clearly affects the rate of damage growth. In the present work we have not altered the viscoplastic rate scale factor during the fall of the roof. However, we suggest that more sophisticated approaches are studied in the future, where the viscoplastic rate scale factor will be scaled up or down accordingly, in order to better capture time discrete events such as a room fall, the impact, and the rock formation at the floor of the room.

3.7.3. 3D Computations

As we showed earlier, full scale three-dimensional computations are within our methodology's reach. Our framework is capable of handling computations with over 30 million particles, and we are confident that this level of refinement can produce high quality results both for the room closure and roof fall cases. In addition, it should be noted that in all the presented computations uniform discretizations were considered. Although high quality results were produced, this can be considered a waste of computational resources. The three-dimensional computations can further benefit from good mesh stretching techniques and mesh refinement only in the areas of interest (for example around the room), a technique that our research group has already started working on and has made considerable progress.

3.7.4. Constitutive Modeling

Constitutive modeling remains a key issue. Are the models adequate for producing correct fractures under impact conditions? Should additional mechanics, such as hardening, be modeled? Is there a good phase-field model that can simultaneously represent the underlying mechanics and deliver a formulation that is a-priori regularized? These questions remain open and very pertinent to the room closure problem.

4. REPRODUCING KERNEL PARTICLE METHOD SIMULATIONS OF EMPTY ROOM CLOSURE

Authors: Jonghyuk Baek[¶], Tsung-Hui Huang[¶], Xiaolong He[¶], Karan Taneja[¶], Haoyan Wei[¶], and Jiun-Shyan Chen[¶]

4.1. Introduction

Numerical simulations of room closure play an important role in predicting the waste isolation process at the WIPP. Traditional mesh-based numerical methods are ineffective in dealing with mesh entanglement related difficulties such as those occurring in large deformation and fragmentation problems. Thus, it is challenging for mesh-based methods to model rocks fracturing, separating, falling, piling, and compacting in the room closure process. Meshfree/meshless methods, on the other hand, proved to be suitable for modeling problems involving large deformation and fragmentation by effectively alleviating the issues related to mesh entanglement since the solution fields are approximated by scattered points without mesh connectivity. This project aims to assess the ability of Reproducing Kernel Particle Method (RKPM) to conduct the simulation of underground empty room closure in rock salt. The focus of this study includes the modeling of room closure with large creep deformation and roof falling with rocks fracturing, piling and compacting processes.

4.2. Model Setup

This project considers the closure of an empty room without nuclear waste. See Sections 2.2.1 to 2.2.4 for respective descriptions of the gradual room closure problem, the room collapse and rubble pile consolidation problem, the salt material model, and the viscoplastic rate scaling technique. A few deviations from Sections 2.2.1 to 2.2.4 are noted below.

Figures 2-4 and 2-5 depict the full width of the room and the full distance D_{h} = 40.54 m between rooms. Both problems have left-right symmetry, so only the right half of each geometry was modeled and rollers were placed along the line of symmetry.

Sliding contact between surfaces was assumed to be frictionless for simplicity.

[¶]Department of Structural Engineering, University of California, San Diego, La Jolla, CA 92093, USA

In order to introduce brittleness for modeling rock fracturing during impact processes, the damage evolution law in Eq. (2.11) is modified by including a portion of elastic strain rate for increased brittleness of material damage:

$$\dot{\omega} = \frac{D}{\mu} \langle \hat{\bar{\sigma}} - \hat{\bar{\sigma}}^{db} \rangle (\dot{\bar{\varepsilon}}^{vp} + \alpha \dot{\bar{\varepsilon}}^{el}), \tag{4.1}$$

where the equivalent elastic strain rate $\dot{\bar{\varepsilon}}^{el}$ is defined as

$$\begin{aligned} \dot{\bar{\varepsilon}}^{el} &= \sqrt{\dot{\boldsymbol{\varepsilon}}^{el} : \dot{\boldsymbol{\varepsilon}}^{el}} \\ \dot{\boldsymbol{\varepsilon}}^{el} &= \dot{\boldsymbol{\varepsilon}} - \dot{\boldsymbol{\varepsilon}}^{vp} \end{aligned} \tag{4.2}$$

and α is a brittleness parameter to introduce proper influence of elastic behaviour in damage evolution. Different values of α will be employed to investigate their influence on the induced brittleness.

Finally, Section 2.2.4 described the viscoplastic rate scaling and mentioned two potential values for the ramp rate s_1. In this study, a ramp rate of $s_1 = 2.0 \times 10^{10}$ s^{-1} is utilized for expediency.

4.2.1. Triaxial Compression Test

To verify the implementation of the creep-damage model in Sec. 2.2.3, a triaxial compression creep test, as described in Section 2.2.3.3, is conducted. The model is under stress-driven compression with input stress components $\sigma_{rr} = \sigma_{\theta\theta} = 5$ MPa and $\sigma_{zz} = 18$ MPa constantly applied. The material constants used for this triaxial compression test are listed in the "Verification" column of Table 2-1. In addition, $\alpha = 0$ to match the model given in Section 2.2.3.1. In Fig. 4-1, the analytical solutions for $\boldsymbol{\varepsilon}$ and ω are respectively labeled as $\boldsymbol{\varepsilon}^{\text{exact}}$ and ω^{exact}, while the numeric solutions are respectively labeled as $\boldsymbol{\varepsilon}^{\text{h}}$ and ω^{h}. The evolution of all strain components and the damage variable agree well with the analytical solutions, which verifies the numerical implementation of the creep-damage model that will be implemented in our meshfree analysis code introduced in the next section.

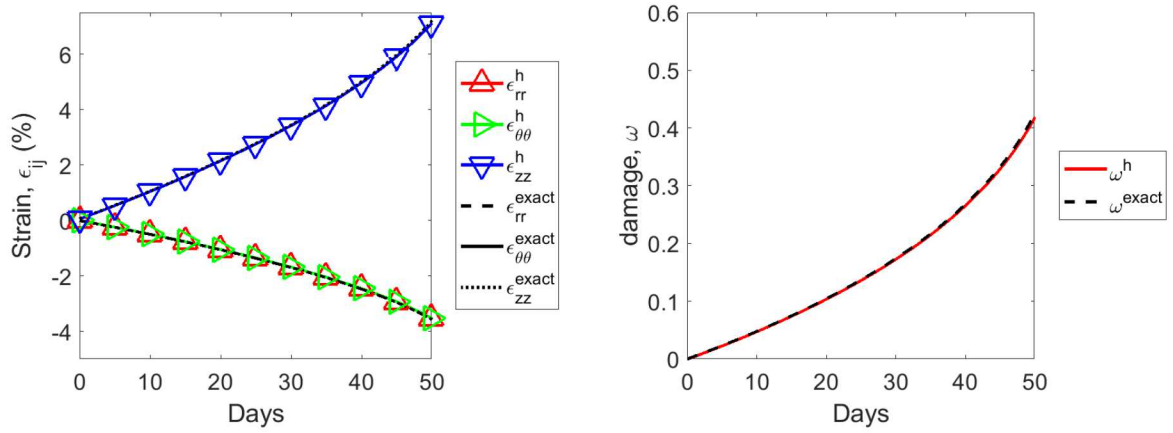

(a) Strain evolution **(b) Damage evolution**

Figure 4-1. A comparison between analytical and numerical solutions regarding the evolution of strain components and the damage variable in the triaxial compression test.

4.3. Numerical Approach

In this study, the empty room closure and roof falling problems are solved using the semi-Lagrangian reproducing kernel particle method (RKPM). The semi-Lagrangian RKPM is an effective numerical method for modeling large deformation and fragmentation problems for which FEM suffers from mesh distortion or mesh entanglement (Chen et al. 1996; Chen et al. 2017). In addition, RKPM provides controllable orders of continuity and completeness, independent from one another, which enables effective solutions of engineering problems involving high-order continuities or discontinuities. For effective numerical integration, the variationally consistent naturally stabilized nodal integration (VC-NSNI) (Chen et al. 2013) is employed for optimal convergence by enforcing variational consistency. The low energy modes are suppressed by introducing an implicit gradient type regularization (Hillman and Chen 2016). In order to consider the objectivity in the context of large deformation, the stress is updated by the Hughes-Winget algorithm (Hughes and Winget 1980) with a fully-implicit scheme for solving Eq. (2.9) ((Reedlunn 2018a)).

In the following subsections, we additionally introduce a damage regularization method and a pressure stabilization method to address the issues of discretization dependency and pressure oscillation, respectively.

4.3.1. Damage Regularization

In the stage of roof falling, the damage initiation and evolution are key processes to predict. However, without proper treatment, the damage pattern presents strong mesh/discretization dependency when the softening effect leads to the loss of ellipticity or parabolicity. Such an issue can be addressed by introducing the nonlocal strain tensor, $\breve{\boldsymbol{\varepsilon}}$, the stress tensor, $\boldsymbol{\sigma}(\breve{\boldsymbol{\varepsilon}}, \boldsymbol{\varepsilon})$, with a

linearly degraded stiffness, can be expressed as follows:

$$\boldsymbol{\sigma}(\breve{\boldsymbol{\varepsilon}}, \boldsymbol{\varepsilon}) = \sum_{i=1}^{3} (1 - \omega_i(\breve{\boldsymbol{\varepsilon}}))\hat{\sigma}_i(\boldsymbol{\varepsilon})\boldsymbol{e}_i \otimes \boldsymbol{e}_i, \tag{4.3}$$

where $\hat{\sigma}_i(\boldsymbol{\varepsilon})$ and $\omega_i(\breve{\boldsymbol{\varepsilon}})$ are the Kachanov stress tensor introduced in 2.2.3.1 and the damage variable calculated using the nonlocal strain tensor in i-th principal direction, respectively. In a generalized expression of the nonlocal strain in a 2-dimensional case, $\breve{\boldsymbol{\varepsilon}}(\boldsymbol{x})$, in Eq. (4.4), the high order gradients of the local strain, $\boldsymbol{\varepsilon}(\boldsymbol{x})$, introduce length scales which control the nonlocality of a numerical model (Chen et al. (2004)).

$$\breve{\boldsymbol{\varepsilon}}(\boldsymbol{x}) = \boldsymbol{\varepsilon}(\boldsymbol{x}) + \sum_{i+j=1}^{n} \alpha_{ij} \frac{\partial^{i+j} \boldsymbol{\varepsilon}(\boldsymbol{x})}{\partial x_1^i \partial x_2^j} \tag{4.4}$$

However, the direct use of Eq. (4.4) requires the computation of higher order gradients of shape functions, which is computationally expensive, as well as the introduction of additional boundary conditions, the meaning of which is physically unclear. To address such issues, in this study, we apply the reproducing kernel strain regularization (RKSR) developed in Chen et al. (2004) where the gradient type nonlocal relationship is embedded in a RK shape function, which ensures discretization-independent and convergent computation with relatively small computational cost.

4.3.2. Pressure Projection

The large viscoplastic deformation caused by creep makes the material nearly incompressible. In numerical simulation, such incompressibility may lead to severe yet unphysical oscillation in the pressure field, which makes the numerical solution unreliable. Also, because the damage boundary is a function of pressure, the computed damage evolution can be inaccurate. In order to address such an issue, we introduce a pressure projection method where the displacement-based pressure field is projected onto a lower order space. As shown in Fig. 4-2, a set of NP nodes, S_N, is further divided into two sets: a master node set, $S_{MN} = \{\boldsymbol{x}_I | \boldsymbol{x}_I \in \Omega\}_{I=1}^{NMN} \subset S_N$, and a slave node set, $S_{SN} = \{\boldsymbol{x}_I | \boldsymbol{x}_I \in \Omega\}_{I=1}^{NSN} \subset S_N$, where NMN and NSN are the number of master nodes and the number of slave nodes, respectively. $S_{MN} \cup S_{SN} = S_N$ and $S_{MN} \cap S_{SN} = \emptyset$. While S_N is used as the displacement nodes and the integration points, S_{MN} is used as pressure nodes, i.e., the projected pressure, $\tilde{p}(\boldsymbol{x})$, is

$$\tilde{p}(\boldsymbol{x}) = \sum_{I=1}^{NMN} Q_I(\boldsymbol{x})\tilde{p}_I, \tag{4.5}$$

where $Q_I(\boldsymbol{x})$ is an RK pressure shape function defined on a support of node I. In case that a linear basis is used for displacement shape functions, one can choose a constant basis for $Q_I(\boldsymbol{x})$ to project the pressure to a lower order space. The size of the support where $Q_I(\boldsymbol{x})$ is defined does not need to be the same as the size of the support where the displacement shape function, $\Psi_I(\boldsymbol{x})$, is defined. The projected pressure is computed by minimizing the following functional:

$$\psi(\tilde{p}_I) = \|\tilde{p}(\boldsymbol{x}) + \frac{1}{3} tr(\boldsymbol{\sigma}(\boldsymbol{x}))\|_{L_2(\Omega)}^2, \tag{4.6}$$

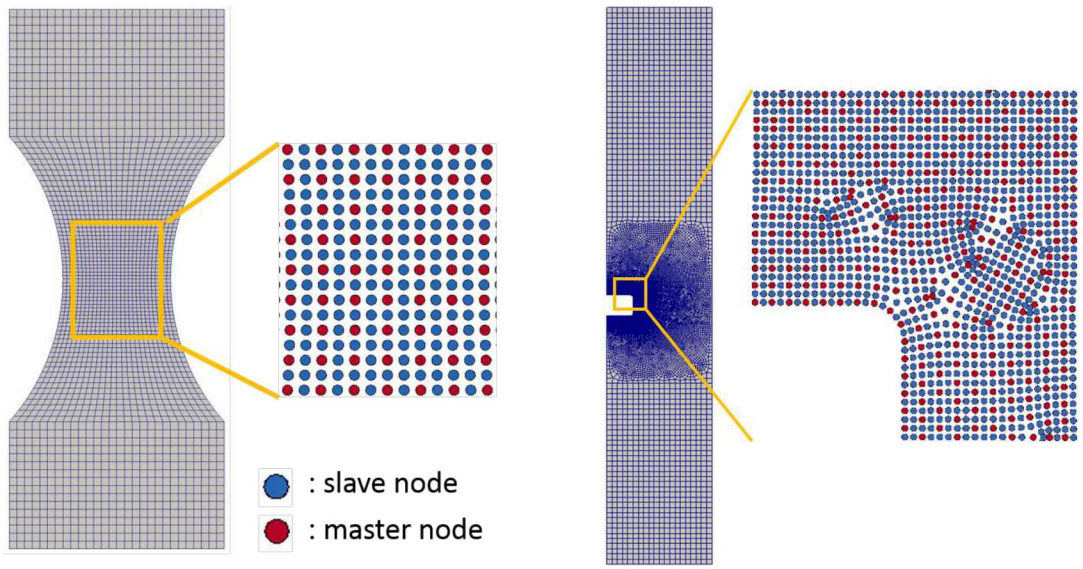

(a) notched bar, regular discretization (b) room model, irregular discretization

Figure 4-2. Master-slave nodal distribution in (a) notched bar compression test, and (b) room model with rounded corners.

where $\boldsymbol{\sigma}(\boldsymbol{x})$ is the displacement-based stress tensor. With $\mathbf{Q}(\boldsymbol{x}) = [Q_1(\boldsymbol{x}), Q_2(\boldsymbol{x}), \ldots, Q_{NMN}(\boldsymbol{x})]$ and $\tilde{\mathbf{p}} = [\tilde{p}_1, \tilde{p}_2, \ldots, \tilde{p}_{NMN}]^T$, one can obtain a matrix equation of the L_2 minimization problem in Eq. (4.6) as follows:

$$\tilde{\mathbf{K}}\tilde{\mathbf{p}} = \mathbf{z}, \tag{4.7}$$

where $\tilde{\mathbf{K}} = \int_\Omega \mathbf{Q}^T(\boldsymbol{x})\mathbf{Q}(\boldsymbol{x})\,\mathrm{d}\Omega$ and $\mathbf{z} = \frac{1}{3}\int_\Omega \mathbf{Q}^T(\boldsymbol{x}) tr(\boldsymbol{\sigma}(\boldsymbol{x}))\,\mathrm{d}\Omega$. In order to efficiently solve Eq. (4.7), we employ a lumping technique for $\tilde{\mathbf{K}}$:

$$\tilde{K}_{IJ}^{\text{lumped}} = \begin{cases} \sum_{L=1}^{NMN} \tilde{K}_{IL} & \text{for } I = J \\ 0 & \text{for } I \neq J \end{cases}, \tag{4.8}$$

which leads to

$$\tilde{p}_I = \frac{\frac{1}{3}\int_\Omega Q_I(\boldsymbol{x}) tr(\boldsymbol{\sigma}(\boldsymbol{x}))\,\mathrm{d}\Omega}{\int_\Omega Q_I(\boldsymbol{x})\,\mathrm{d}\Omega}, \tag{4.9}$$

with $\sum_{L=1}^{NMN} Q_L(\boldsymbol{x}) = 1$. The projected stress field is calculated by replacing the displacement-based pressure with the projected pressure as follows:

$$\tilde{\boldsymbol{\sigma}}(\boldsymbol{x}) = \boldsymbol{\sigma}^{dev}(\boldsymbol{x}) - \tilde{p}(\boldsymbol{x})\mathbf{I}. \tag{4.10}$$

4.3.3. Benchmark Problem: Notched Bar Compression Test

To verify the capability of damage regularization by RKSR and pressure stabilization by pressure projection method, a notched bar compression test is carried out, as shown in Fig. 4-3. Three

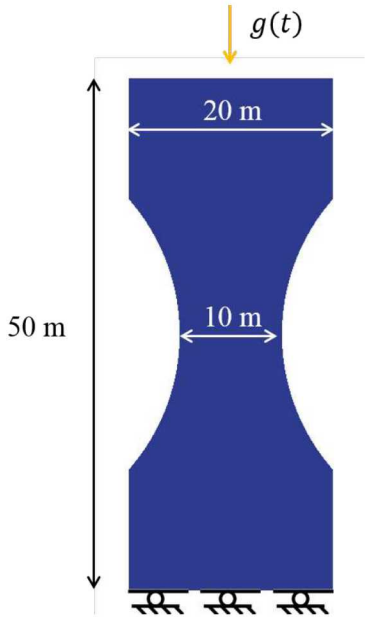

Figure 4-3. Notched bar compression test.

different discretizations are considered, with minimal nodal spacings of $h_{min} = 0.68, 0.34, 0.17$ m, denoted as M01, M02 and M03, respectively. A prescribed displacement $g(t)$ is applied to the upper boundary in the vertical direction, while the lower boundary is fixed. The prescribed displacement, $g(t)$, is defined as

$$g(t) = \begin{cases} \frac{v_0}{2}(t - \frac{T_0}{\pi}\sin(\pi\frac{t}{T_0})) & \text{for } 0 \le t < T_0 \\ g(T_0) + v_0(t - T_0) & \text{for } T_0 \le t \end{cases}, \tag{4.11}$$

with $T_0 = 0.5$ and $v_0 = 1.0$. The numerical setting for RKPM and RKSR is listed in Table 4-1. The creep-damage model introduced in Sec. 2.2.3 is employed with the material constants listed in the "Collapse" column of Table 2-1. Fig. 4-4 depicts the damage fields for each level of

Table 4-1. Numerical setting of the notched bar compression test

Basic RKPM setting
Lagrangian RKPM, SCNI
Linear basis
Normalized support size of 2.0
Cubic B-spline Kernel Function
RKSR Setting
Characteristic length scale, $l_c = 1.2$ m
Cubic B-spline Kernel Function
Second order basis

refinement with and without employing RKSR. It can be seen that the damage patterns of the un-regularized models differ as the domain is refined. By applying RKSR, however, the damage field is regularized such that the pattern and the bandwidth of the damage are consistent in each

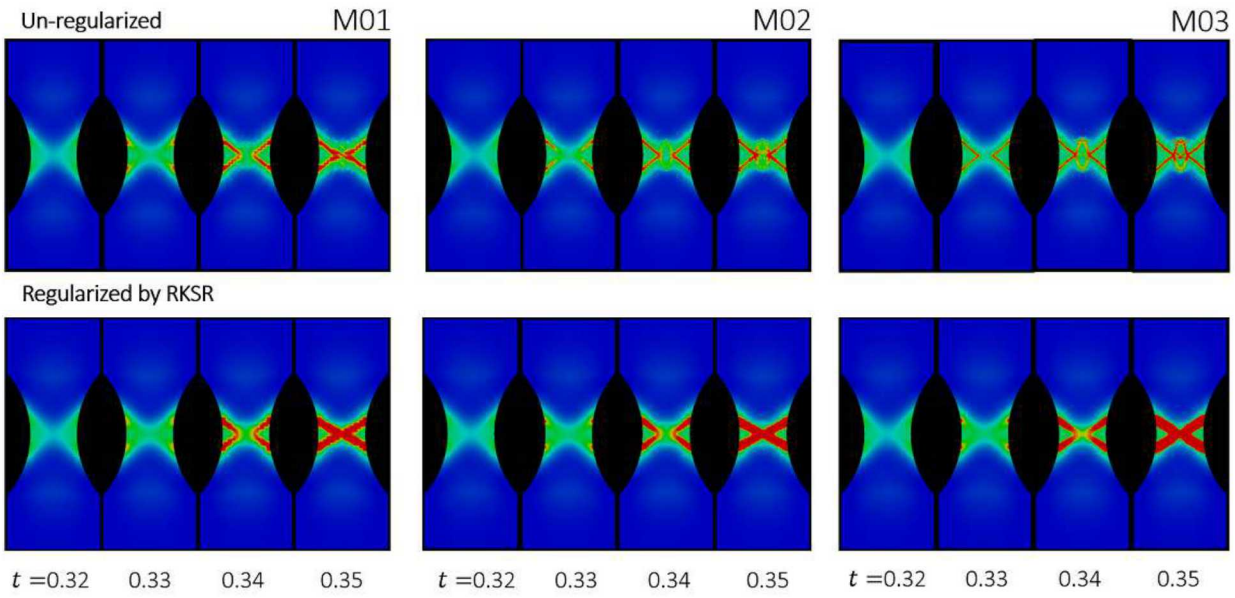

Figure 4-4. Damage fields of the notched bar under compression at different simulation time: (top) without RKSR and (bottom) with RKSR.

level of refinement. Then, with RKSR, we apply the introduced pressure projection (PP) method to the problem and a comparison of results is shown in Fig. 4-5. As shown in Fig. 4-5, the

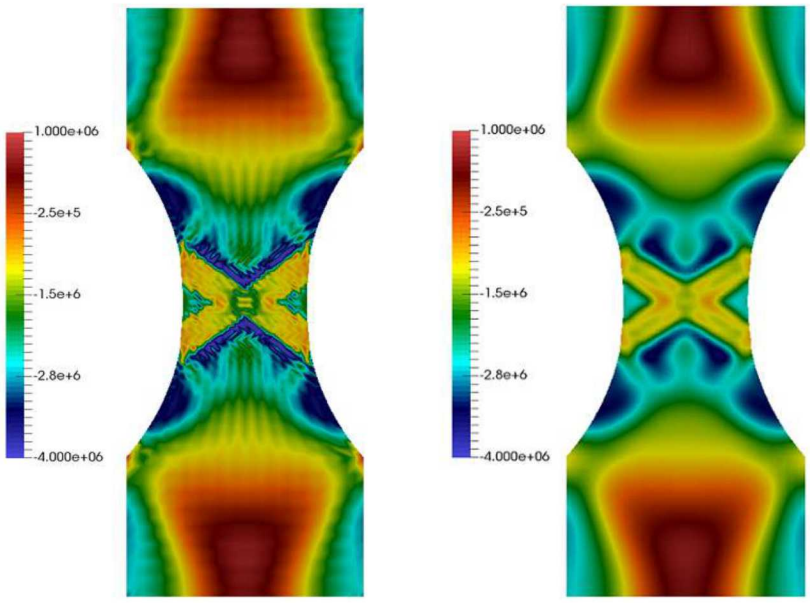

(a) RKSR without PP **(b) RKSR with PP**

Figure 4-5. Pressure fields of the notched bar under compression with M02 discretization: (a) without and (b) with pressure projection.

noticeable pressure oscillation is diminished, and Fig. 4-6 shows that the pressure fields are stabilized and consistent results are obtained in all three discretizations. Finally, to further assess

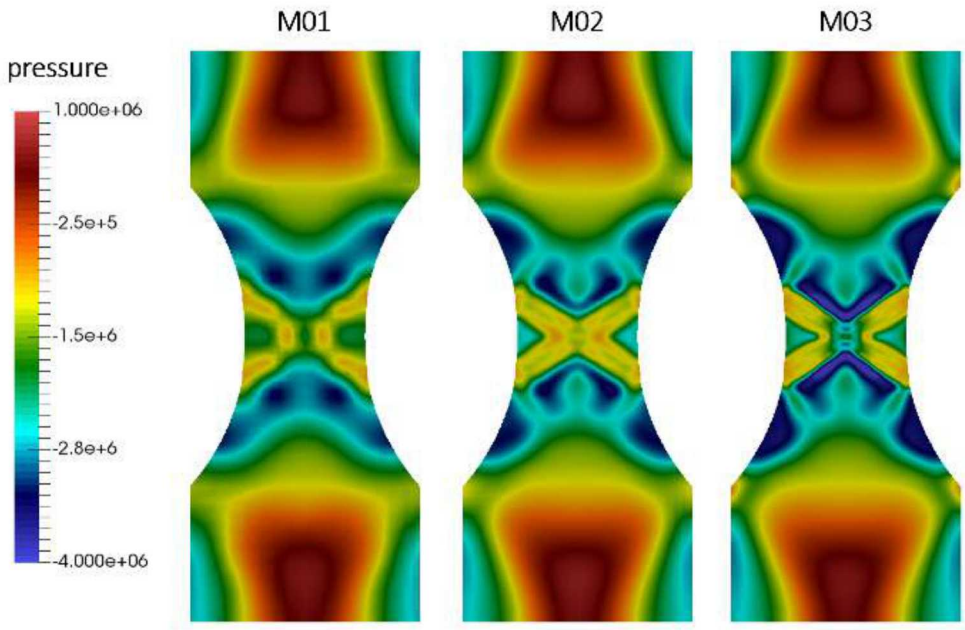

Figure 4-6. Pressure fields of the notched bar under compression with different discretizations.

the effects of the regularization with and without pressure projection, the force-displacement curves measured at the upper boundary of the bar are plotted in Fig. 4-7. RKSR reduces the mesh-sensitive response presented by the un-regularized models, which indicates that the same level of energy is dissipated by the damage evolution when RKSR is employed. RKSR in conjunction with pressure projection produces mesh-independent results as shown in Fig. 4-7.

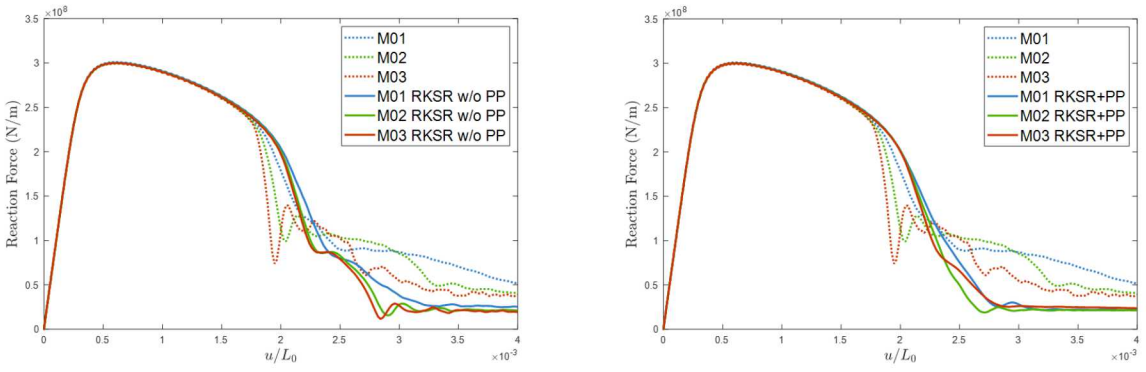

(a) Without pressure projection **(b) With pressure projection**

Figure 4-7. Force-displacement curves of the notched bar under compression, without and with pressure projection.

4.4. Modeling of Empty Room Closure and Roof Falling

In this section, the effectiveness of the proposed RKPM modeling framework is demonstrated through modeling of empty room closure and roof falling. The convergence, stability, and computational efficiency of RKPM modelings are also investigated. The details of the rock falling, piling, and compacting are conducted by introducing an adaptive time scaling scheme. The numerical settings for RKPM simulations shown in this section are provided in Table 4-2. **Note:** The employed in-house RKPM code, the Nonlinear Meshfree Analysis Program (NMAP)

Table 4-2. Numerical setting of room closure study

Numerical setting	Value/Rule
Normalized support size	2.0
Kernel function	Cubic B-Spline kernel
Order of basis	Linear
Time step size	10^{-5} (sec)
Quadrature rule	Semi-Lagrangian, VC-NSNI

(Chen 2001), is a 3-D explicit code. Hence, in this study, the models are discretized on the x-z plane with two identical layers of discrete nodes aligned in the y-direction to perform plane-strain simulations. The y-directional displacement is constrained to zero. The total number of nodes presented in this report include the discrete nodes in both layers.

4.4.1. Room Closure Modeling

4.4.1.1. Gradual Room Closure

The closure of a clay-seam-free room is first modeled by considering creep without damage evolution. Rooms with sharp corner geometry is considered in the following simulations, as shown in Fig. 2-4.

In the sharp corner room models, four discretizations are applied for the convergence test, and the models are denoted as MS01 to MS04 for the sharp corner models. The details of the discretization of each model are listed in Table. 4-3, where h_{min} denotes the minimum nodal spacing. As shown in Fig. 2-4, let L_h be the initial width of the room and $\delta_h(t)$ be the width

Table 4-3. Discretization refinement for sharp cornered models

h_{min}	Model	No. of nodes
0.4 m	MS01	11314
0.2 m	MS02	25198
0.1 m	MS03	57284
0.05 m	MS04	139030

change, L_v be the vertical height of the room and $\delta_v(t)$ be the height change, and $V_{\text{room}}(t)$ be the

current volume of the room at time t. The room closure is measured by the following quantities:

$$\begin{aligned} \text{Horizontal closure: } & \frac{\delta_h(t)}{L_h} \\ \text{Vertical closure: } & \frac{\delta_v(t)}{L_v} \\ \text{Normalized porosity: } & \frac{V_{\text{room}}(t)}{V_{\text{room}}(0)} \end{aligned} \tag{4.12}$$

In the case where the room boundary is undamaged and trackable, V_{room} is calculated by the contour integral of the nodes on the room boundary. As shown in Figs. 4-8, the closure behaviours at different levels of refinement are consistent. To verify the solution convergence, we compared the three measurements in Eq. (4.12) with the reference solution of the sharp-corner model provided by Sandia National Laboratories (see Section 2.2.1 and Appendix A.3), as shown in Figs. 4-9. The RKPM solution converges to the reference solution as the model is refined. The room closes at approximately the $150-160^{th}$ year.

Finally, the computational efficiency and parallel computation performance of the RKPM NMAP code are investigated by comparing the computational time (wall time) of the numerical simulations using the sharp-corner models, MS01 to MS04. Normalized CPU time, wall time per unit momentum balance time, of the simulations with different levels of refinement and processors are presented in Fig. 4-10 and Table 4-4, where NP denotes the total number of RK nodes and p is the total number of processors used in the simulations. For the room closure simulation of the sharp model, the total momentum balance time is 1 second and the momentum balance timestep size is 10^{-5} second, namely, each simulation takes 10^5 steps.

Table 4-4. Normalized CPU time by p processors of four different discretization.

	Number of nodes (NP)			
p	NP=11314	NP=25198	NP=57284	NP=139030
1	1.65×10^{-1}	3.75×10^{-1}	9.39×10^{-1}	$2.46\times10^{+0}$
2	1.16×10^{-1}	2.55×10^{-1}	6.00×10^{-1}	$1.47\times10^{+0}$
4	6.21×10^{-2}	1.39×10^{-1}	3.26×10^{-1}	8.38×10^{-1}
8	3.94×10^{-2}	8.83×10^{-2}	2.13×10^{-1}	5.56×10^{-1}
16	3.40×10^{-2}	7.69×10^{-2}	1.91×10^{-1}	4.97×10^{-1}
32	2.66×10^{-2}	5.99×10^{-2}	1.47×10^{-1}	4.02×10^{-1}

Unit: (second per unit moment balance time (10^-5 second))

To further investigate the parallel performance, the speedup and computational efficiency are studied, where the speedup is defined in Eq. (4.13) as

$$S_p = \frac{T_{serial}}{T_p}. \tag{4.13}$$

Here, S_p is the speedup with p processors, T_{serial} is the serial execution time per time step (normalized CPU time) associated with the RKPM sequential algorithm and T_p is the execution

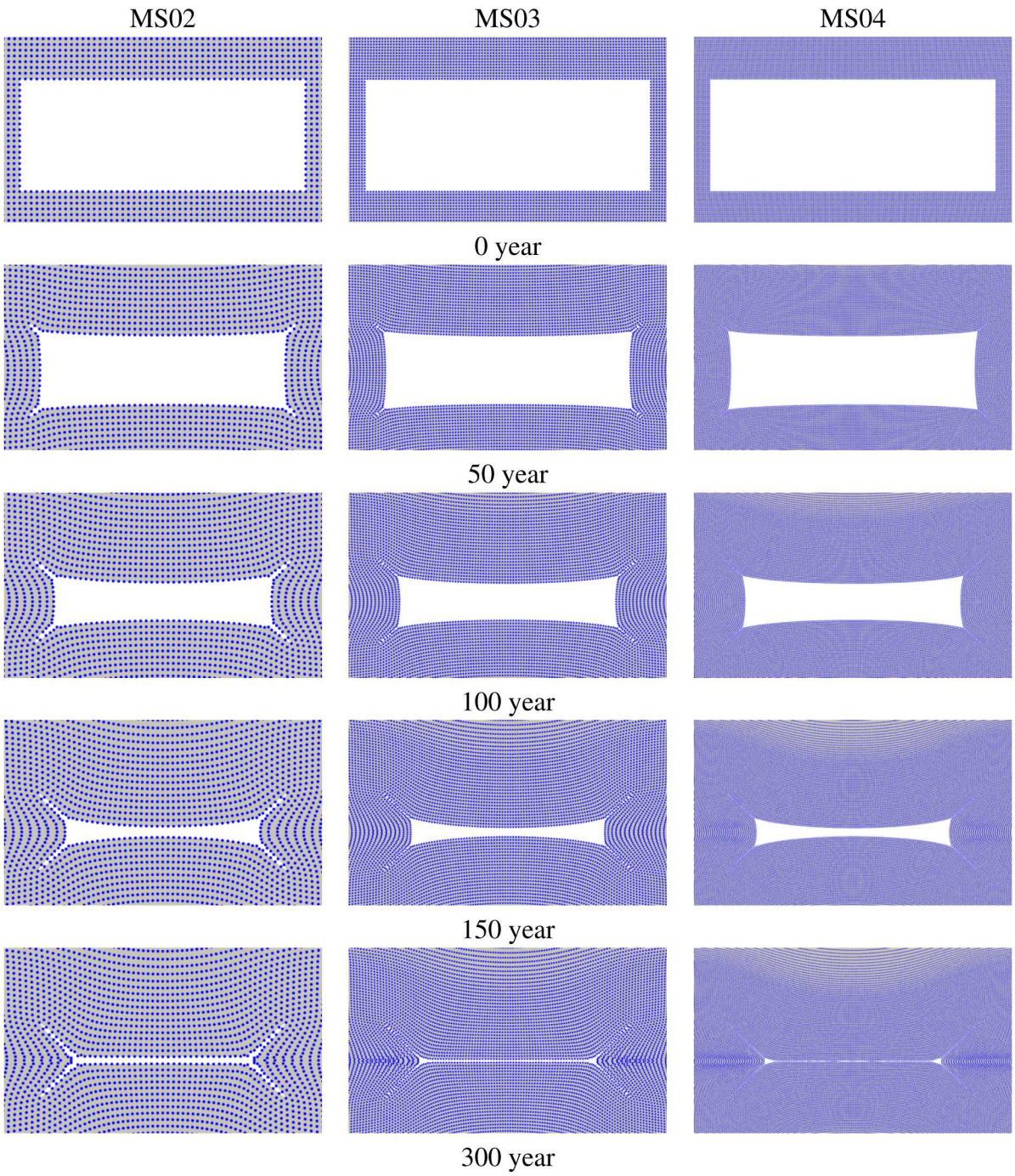

Figure 4-8. Nodal distribution of sharp-corner room closure under different discretizations.

time per time step associated with the parallel algorithm to solve the same problem by using p processors. The parallel computation performance of the proposed RKPM framework can be measured by comparing the speedup S_p with the ideal speedup curve $S_p = p$, as shown in Fig. 4-11. From Fig. 4-11, the RKPM parallel computation performance is independent of the discretization. However, the parallel computation speedup is not compatible with the ideal curve when more than 8 processors are employed. It is likely due to the use of a 3-D RKPM code with

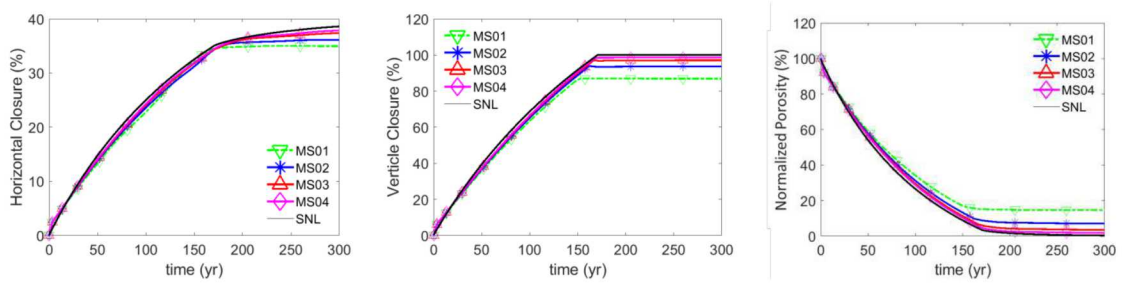

(a) Horizontal closure (b) Vertical closure (c) Normalized porosity

Figure 4-9. Room closure measurements for sharp corner model.

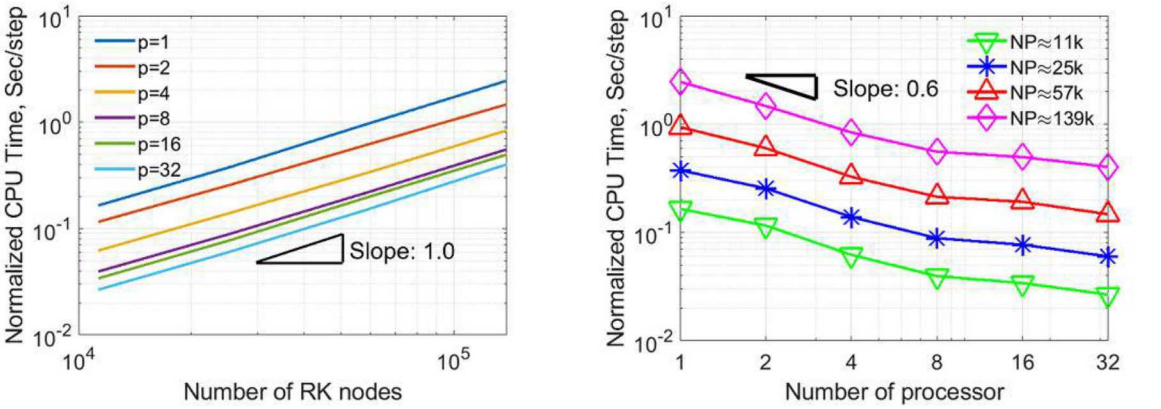

(a) Normalized CPU time vs. no. of RK nodes (b) Normalized CPU time vs. no. of processors

Figure 4-10. Computational efficiency of RKPM simulation. The details of the data of CPU time and discretization can be found from Table. 4-4. p is the number of processors employed in the simulation, and NP is the total number of nodes in the 2-layer discretization explained in Sec. 4.4.

2-layer discretized models such that 3-D shape functions and neighbor search are required, which significantly increases the computational time, compared to that of using a pure 2-D code with 1-layer models. The employment of simple node number partitioning instead of graph based domain partitioning algorithm is also responsible to this inefficiency. The improvement of the parallel algorithm will be considered in the future work.

4.4.1.2. Creep-Damage Modeling for Empty Room Closure

Table 4-5. Discretizations of the empty room model in creep-damage modeling

h_{min}	No. of nodes
0.2 m	24972
0.1 m	39566
0.05 m	54664

Following 4.4.1.1, the convergence study is performed using the rounded-corner model shown in Fig. 2-5 with the creep-damage model. A locally refined model is used in order to better capture

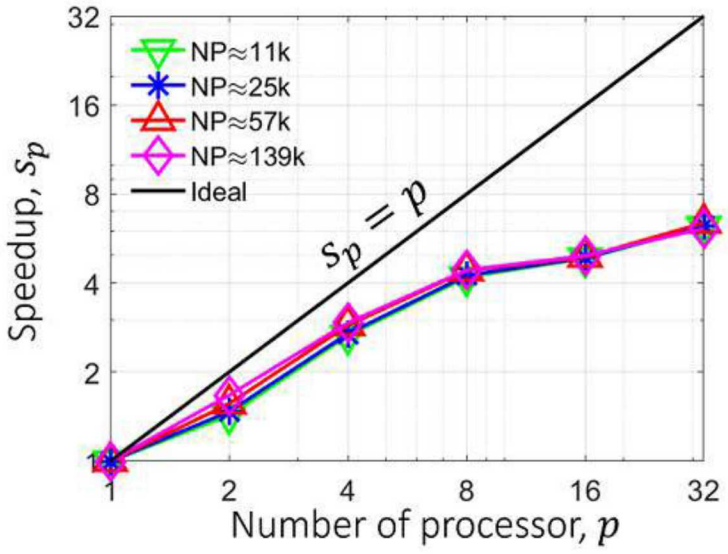

Figure 4-11. Speedup for sharp corner model under different discretization refinement.

damage evolution near the empty room. For this study, we consider three discretizations, with minimum nodal spacing h_{min} = 0.2, 0.1, 0.05 m. The total number of nodes are listed in Table 4-5. A characteristic length l_c = 0.15 m is employed for the RKSR damage regularization. From the numerical results shown in Fig. 4-12, the damage evolution and patterns are consistent under different discretizations, which shows an effective damage regularization by RKSR. Note that, in Fig. 4-12 and in the other figures in Chapter 4 that show damage field, ω is plotted, that is, the tensile and compressive limits ω^t and ω^c defined in Section 2.2.3.1 are not applied in the figures.

To investigate how damage evolves during the room closure, the progressive deformation of the model with h_{min} = 0.1 m is shown in Fig. 4-13. The damage is initiated at the room corners as shown in Fig. 4-12a, then forms a triangular block along the side wall in the third year. Afterwards, the damage starts to propagate above the roof and beneath the floor along the direction around 40-45 degrees angle with respect to the ceiling or the floor, and thereafter forms another two triangular blocks above the roof and beneath the floor in the 39th year. From the results in Figs 4-13d to 4-13f, the room is closed in around 80 years, without roof falling. This is because the room closes very fast due to high creep deformation rate caused by using a large time scaling factor, where the damages leading to roof falling are not captured. In order to model dynamical processes of roof separation, rock falling, piling, and compaction, the scaling of creep deformation rate needs to be significantly reduced when sufficient damage forms so that potential roof falling is captured. This can be done by employing an adaptive time scaling approach which will be introduced in 4.4.2.1. Finally, the room closure measurements in Eq. (4.12) are computed for this case as shown in Fig. 4-14. As can be seen, the results are consistent under all three discretizations.

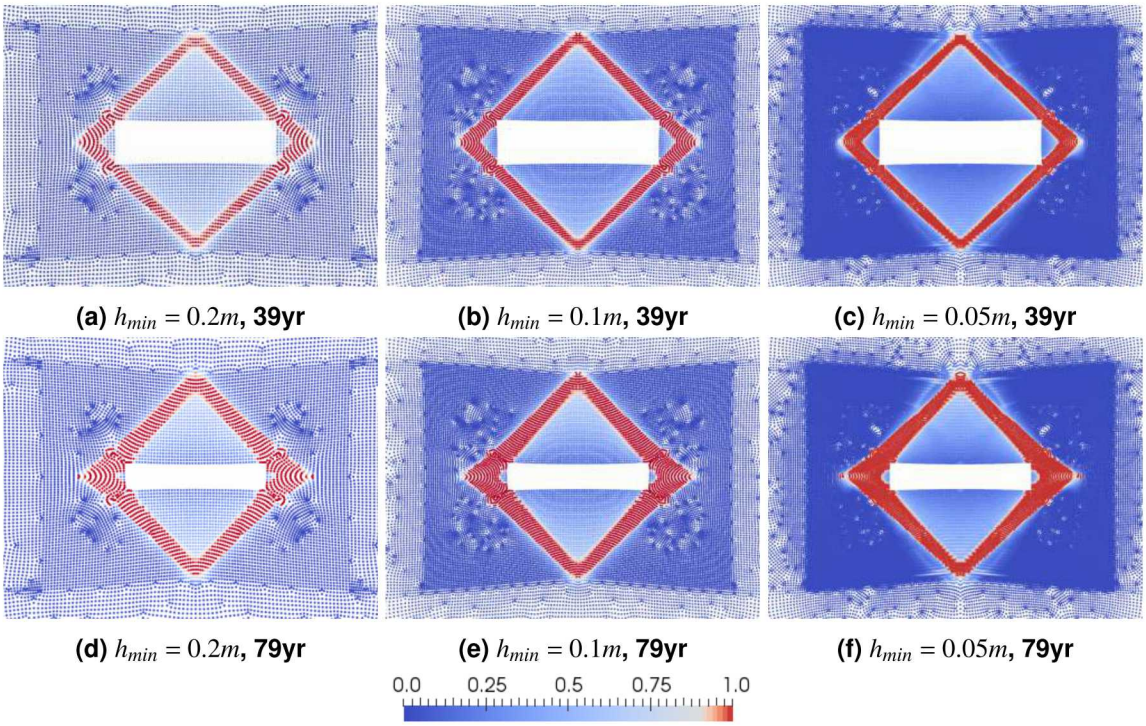

Figure 4-12. Damage distributions of room closure modeling under different discretizations.

4.4.2. Roof Fall Modeling

4.4.2.1. Adaptive Time Scaling

In the creep model shown in Sec. 2.2.3, a time scaling in Eqs. (2.16)-(2.18) is employed to enable quasi-static simulation using an explicit dynamic code. However, the numerical results discussed in Sec. 4.4.1.2 show that the creep strain is scaled up too quickly above the roof during the major damage initiation and evolution processes, and fail to capture the rock salt falling details. The process of roof collapsing and falling is a fast dynamical process occurring in seconds, while the whole room closure due to creep is a long-term quasi-static process lasting for hundreds, if not thousands, of years. Therefore, to capture the two processes with distinct time scales in the simulation, an adaptive time scaling approach is introduced and the time scaling factor is defined in Eq. (4.14) as

$$s = \begin{cases} s_0 + s_1 t^{mb} & \text{if } t^{mb} < t_1^{mb} \\ 1 & \text{if } t_1^{mb} \le t^{mb} \le t_2^{mb} \\ s_0 + s_1 (t^{mb} - (t_2^{mb} - t_1^{mb})) & \text{if } t_2^{mb} < t^{mb} \end{cases} \tag{4.14}$$

where t_1^{mb} and t_2^{mb} are starting and ending time of a simulation time period without time scaling so as to capture the fine time scale roof falling response. The values of $s_0 = 0.01$ and $s_1 = 2 \times 10^{10}$ 1/s are employed in this study. An example of a typical adaptive time scaling factor versus the simulation time (momentum balance time t^{mb}) is shown in Fig. 4-15b and the corresponding physical time versus the simulation time t^{mb} is shown in Fig. 4-15a. To avoid a sudden change in viscoplastic strain rate due to the time scaling factor s in Eq. (2.16), the scaling

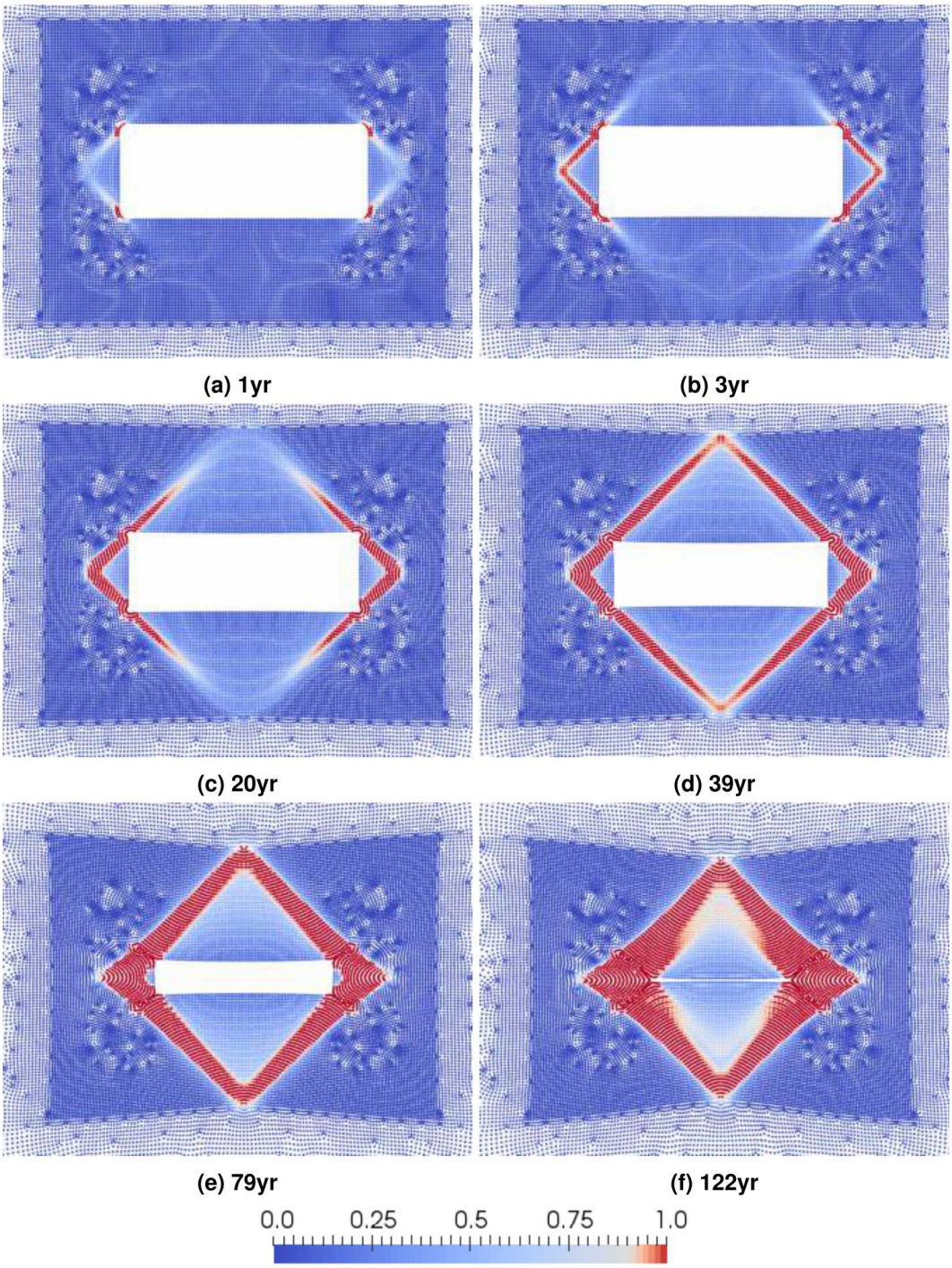

Figure 4-13. Damage field of room closure modeling at different time with $h_{min} = 0.1m$.

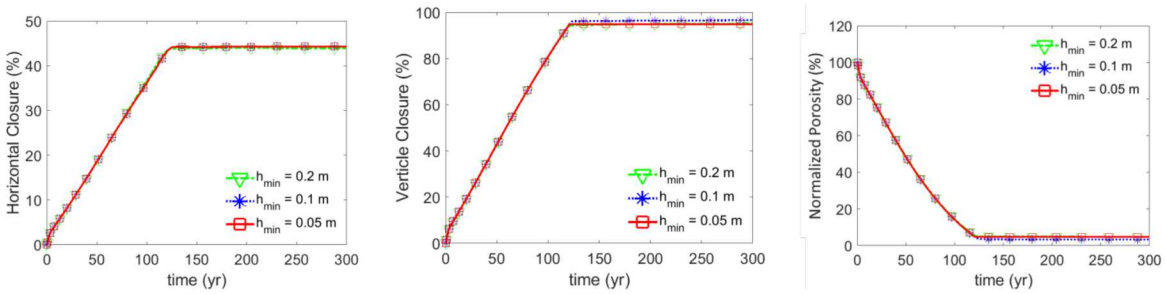

(a) Horizontal Closure **(b) Vertical Closure** **(c) Normalized Porosity**

Figure 4-14. Room closure measurements for creep-damage model under different discretizations.

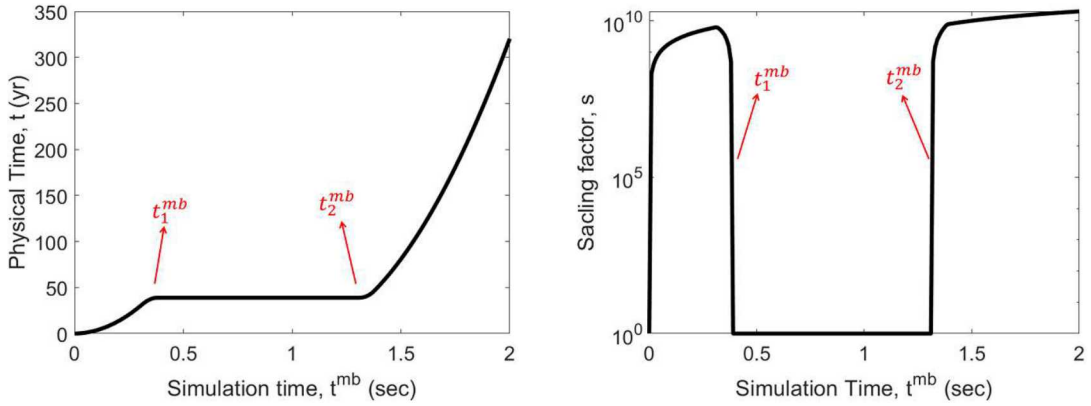

(a) t **v.s.** t^{mb} **(b)** s **v.s.** t^{mb}

Figure 4-15. Adaptive time scaling profile for modeling roof falling with $t_1^{mb} = 0.35$ **and** $t_2^{mb} = 1.35$**: (a) physical time** t **versus momentum balance time** t^{mb}**, and (b) corresponding scaling factor.**

factor near t_1^{mb} and t_2^{mb} are smoothly ramped as shown in Fig. 4-15. From the scaling profile in Fig. 4-15, we consider three stages in the room closure simulation, as depicted in Fig. 4-16. At the first stage in Fig. 4-16a, the room starts to close due to creep deformation, and damage bands form above the roof. Following the first stage, as shown in Fig. 4-16b, the roof begins to fall and the time scaling factor s scaled back to 1 to retain the inertia effect. Finally, after the roof falls and impacts the floor as shown in Fig. 4-16c, the room continues to close and the time scaling factor is scaled up again to accelerate the creep deformation process. From Eq. (4.14) and Fig. 4-16, t_1^{mb} and t_2^{mb} are taken to be the times when damage bands initiate to yield roof falling and the time when roof falling ends, respectively. In this study, t_1^{mb} and t_2^{mb} are determined empirically.

4.4.2.2. Roof Falling Without a Clay Seam

In this section, we focus on modeling the roof falling process without considering the influence of the clay seam. The numerical model ($h_{min} = 0.1$ m) and setting employed in 4.4.1.2 are considered here and the aforementioned adaptive time scaling is applied. Simulation tests show the damage zone with potential roof falling initiates at around the 39th year and the corresponding

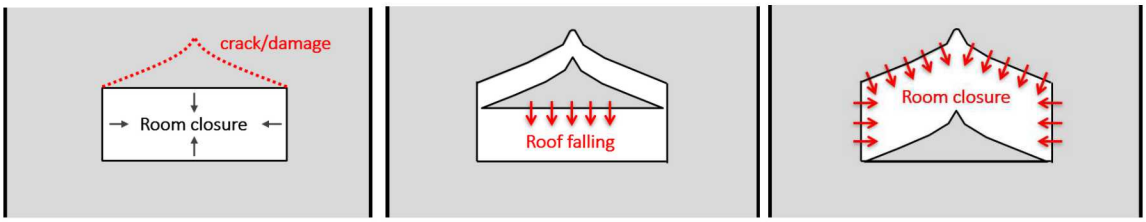

(a) Room closure (b) Roof falling (c) Room closure

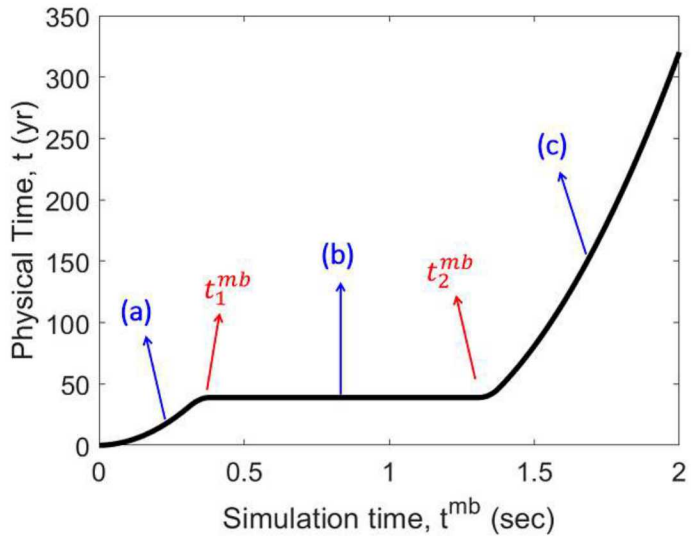

Figure 4-16. Typical three stages of room closure with roof falling in the WIPP.

simulation time is set as t_1^{mb}. To investigate the effects of the brittleness parameter, α in Eq. (4.1), on the roof falling process and the damage patterns after roof fall, α with four different values are considered and studied, i.e., $\alpha = 0$, 0.5, 2.0, and 3.0. The results with $\alpha = 0$ and 0.5 are nearly identical, so only the results with $\alpha = 0.5$, 2.0, and 3.0 are shown.

From the numerical results of roof falling shown in Fig. 4-17, the triangular block above the room falls at around the 39th year. The falling process takes around 0.7 to 0.9 seconds in these cases. The numerical results show that RKPM effectively captures the rock separation and falling processes, which poses challenges for mesh-based methods such as FEM. The comparison in Fig. 4-17 shows that using α with a smaller value ($\alpha = 0.5$) causes little damage when the roof impacts the ground, which could be due to the smaller brittleness introduced. The results of $\alpha = 2.0$ and 3.0 show that the roof-floor impact causes the rock to break into 3-4 pieces, and some damages accumulate beneath the floor and above the roof, as shown in the results at 0.9 second in Fig. 4-17. This could be due to the elastic wave propagation cased by the impact. The results also show that the case with larger α exhibits more diffusive damage pattern.

Following the impact, the time scaling factor scales back to speed up creep deformation and the room continues to close, as shown in Fig. 4-18, where the room with a larger value of α ($\alpha = 2.0$ or 3.0) closes slightly faster than the case with a smaller α ($\alpha = 0.5$). The reasons could be: (1) the damaged rock salt can rearrange and compress more easily than intact rock and (2) faster damage evolution in the rock salt with higher α value. Regarding (1), adding healing to the constitutive

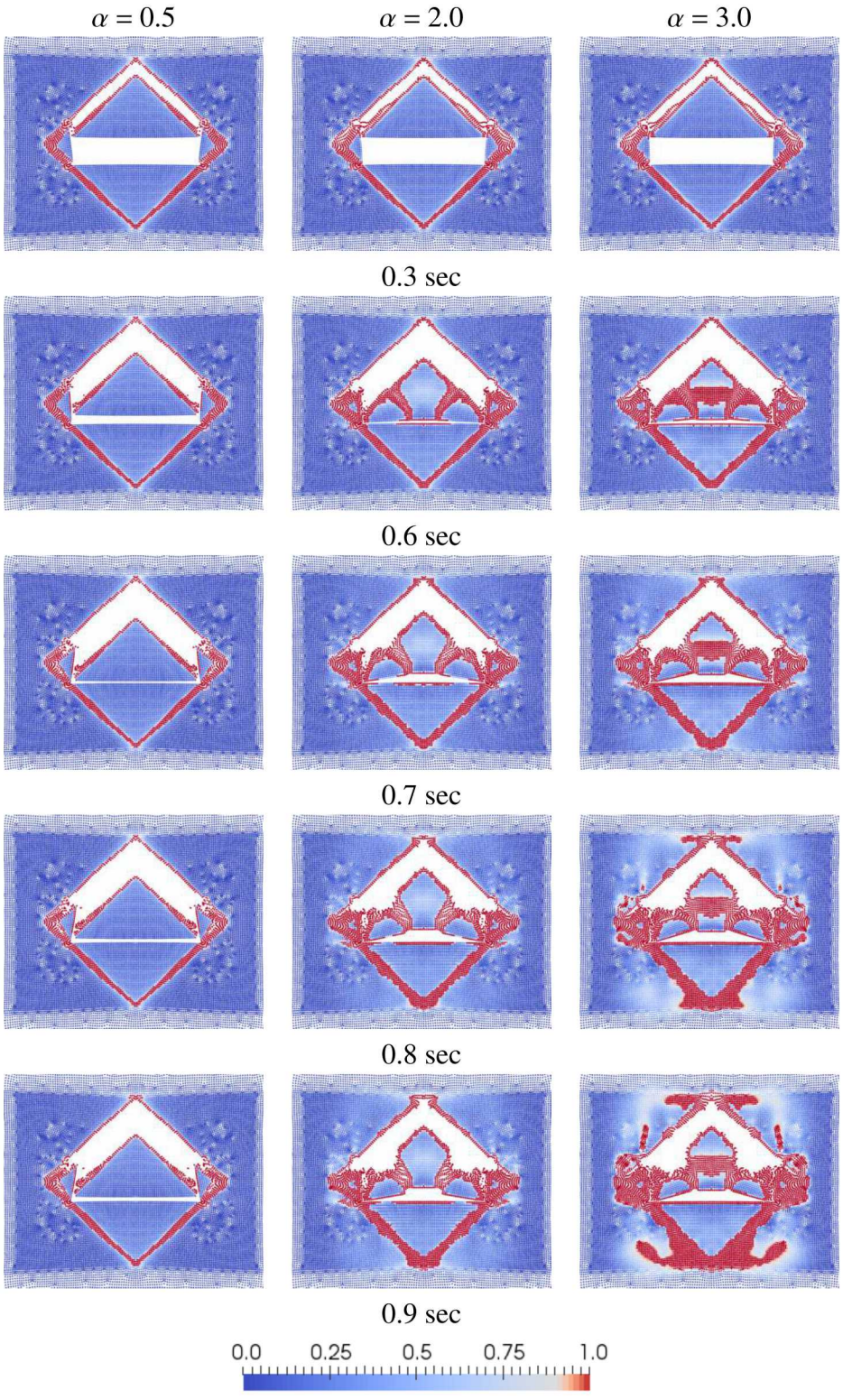

Figure 4-17. The roof falling process at the 39th year in empty room modeling with adaptive time scaling factor.

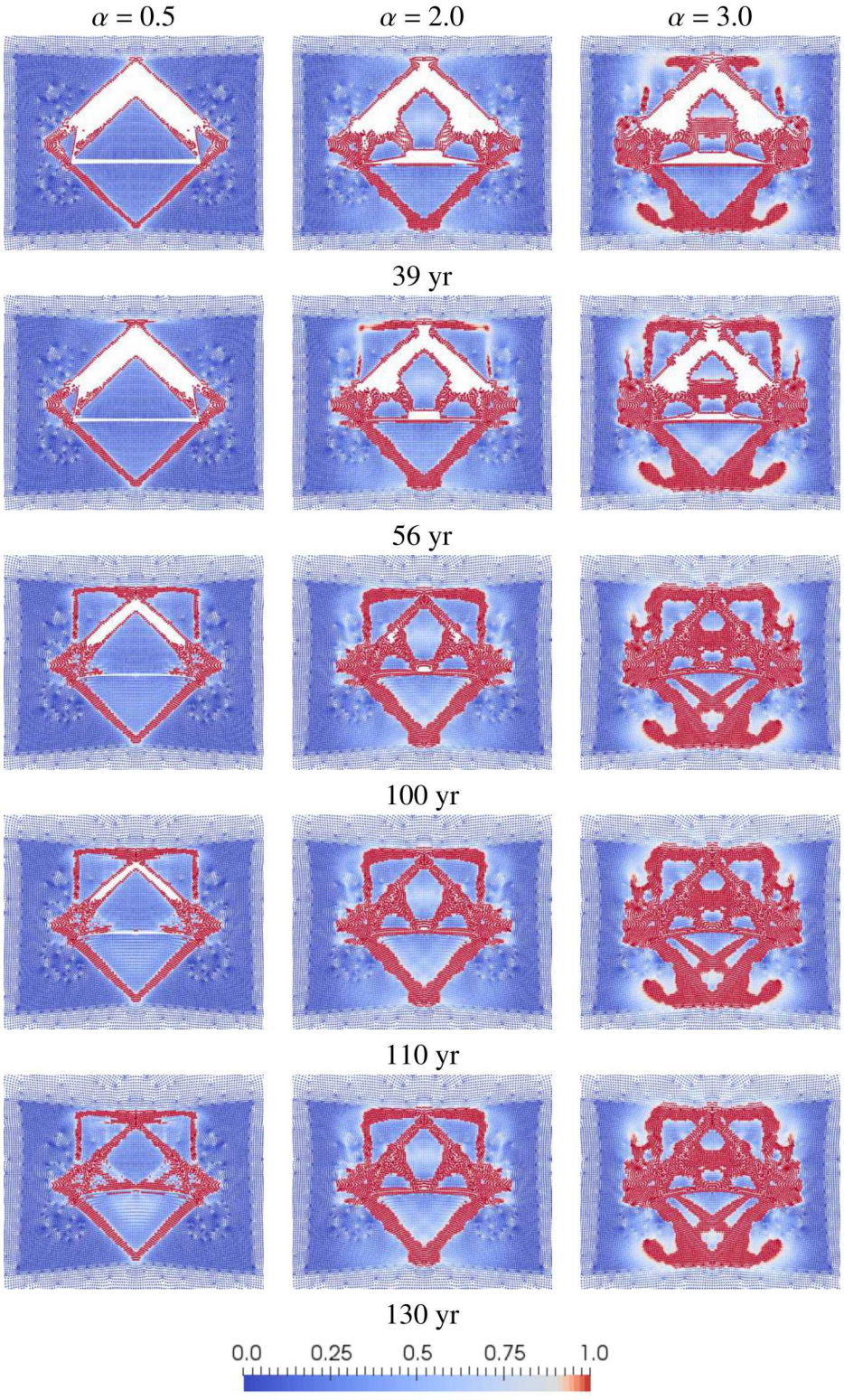

Figure 4-18. The room closure after the roof falling and impacting.

model could reduce the rubble pile's ability to rearrange and compress if sufficient hydrostatic pressure is attained prior to full reconsolidation. The results of the final closed-room configuration of these cases and their corresponding closure time are shown in Fig. 4-19. It is observed that several pieces of undamaged rock are surrounded by damaged rock after the compaction with more rock pieces found in the case with a larger value of α. The results in Figs. 4-17 and 4-18 demonstrate how the semi-Lagrangian RKPM is capable of modeling the failure mechanisms in the room-closure process, and how the material model can have profound influence on the predicted processes of rock fracturing, separating, falling, impacting, and compaction.

In these simulations, the closed room at the final stage contains a mixture of excessively damaged rock particles and undamaged portions of the roof, which makes it hard to employ Eq. (4.12) to measure the normalized porosity. Instead, we first consider the nodal volume $V_I(t)$ for I-th RK node at time t can be calculated by employing the deformation gradient $\mathbf{F}$:

$$V_I(t) = \frac{V_I(t_0)}{det(\mathbf{F}(\boldsymbol{x}_I))} \tag{4.15}$$

and then the normalized porosity can be calculated by considering the volume change of the RK nodes inside an enclosed domain during the deformation. The enclosed domain contains the empty room with all potentially damaged RK nodes during the simulation. In this case, a circular domain Ω_{cir} with a radius 8 meters is used, as shown in Fig. 4-20. From the Fig. 4-20, the normalized porosity in this case can be defined as

$$\text{normalized porosity} = \frac{V_{\text{cir}} - \sum_{I \in S_{\boldsymbol{x}}(t)} V_I(t)}{V_{\text{room}}(0)} \tag{4.16}$$

where V_{cir} is the volume of the domain Ω_{cir}, $V_{\text{room}}(0)$ is the initial empty room volume, and nodal set $S_{\boldsymbol{x}}(t) = \{I | \boldsymbol{x}(\boldsymbol{X}_I, t) \in \Omega_{\text{cir}}\}$. The room porosity calculated by Eqs. (4.12) and (4.16) give similar results for the case of a room without roof falls, but Eq. (4.16) produces a noisier normalized porosity versus time curve. Equation (4.12) only involves a contour integral of nodes on the room boundary, where the nodes are known a priori, while Eq. (4.16) involves nodal volume changes within the circular domain Ω_{cir}. The noise associated with Eq. (4.16) is likely due to nodes moving in and out of Ω_{cir} during the simulation.

From Fig. 4-21, it can be found that the normalized porosity is around 60% during the roof falling stage, and then the room closes at around the $130^{th}, 110^{th}, 100^{th}$ year in the case of $\alpha = 0.5$, 2.0, and 3.0, respectively. The evolution of the normalized porosities are consistent with the numerical results in Figs. 4-17 to 4-19.

4.4.2.3. Roof Falling with Clay Seam

As the existence of a clay seam could interact with the damage evolution and yield different failure mechanisms (see Figs. 4-17 and 4-22), it is important to investigate its effects on the damage evolution and roof fall. The clay seam is modeled as an initially damaged zone with a thickness of 0.2 m. (The mid-thickness is $L_{\text{g}} = 2.43$ m above the room ceiling.) In this study, the initial damage parameter of the clay seam is set to be 0.9 so as to reflect the lower strength in the

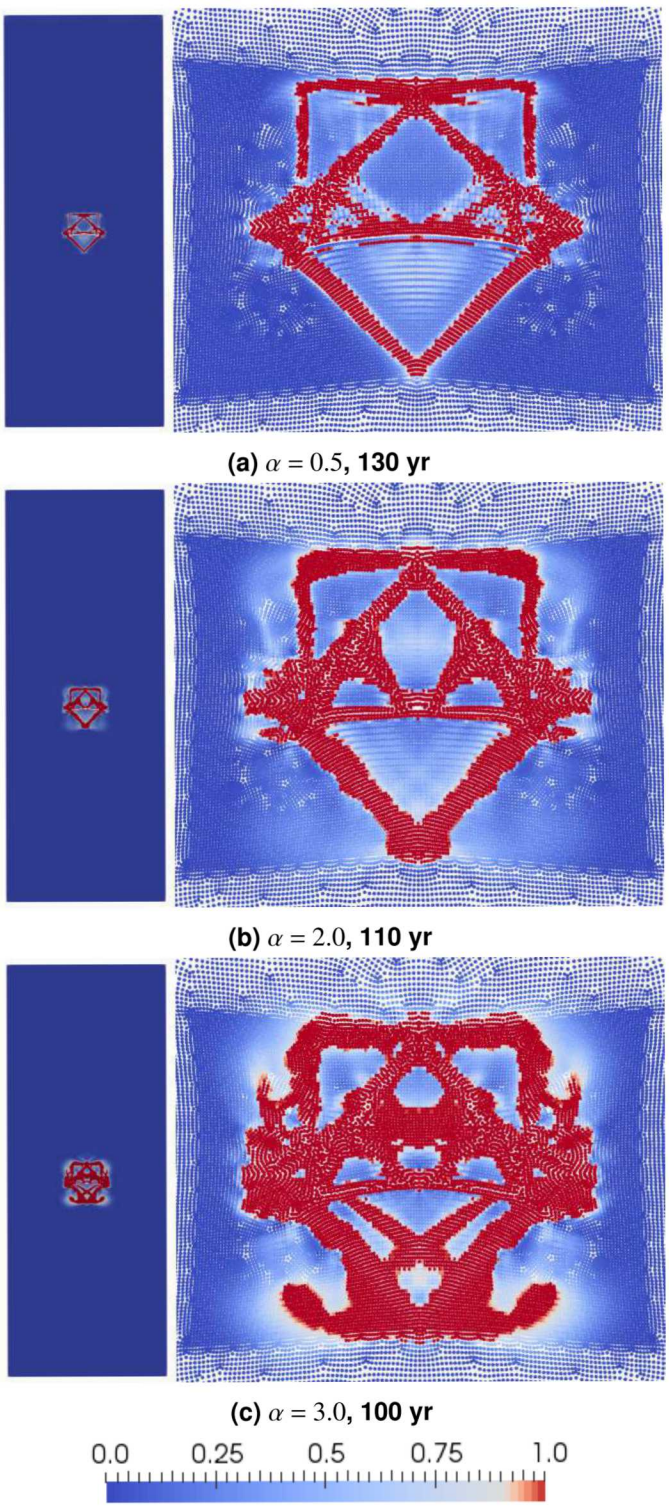

(a) $\alpha = 0.5$**, 130 yr**

(b) $\alpha = 2.0$**, 110 yr**

(c) $\alpha = 3.0$**, 100 yr**

Figure 4-19. Final room closure configuration and the corresponding closure time for the cases with (a) $\alpha = 0.5$**, (b)** $\alpha = 2.0$**, and (c)** $\alpha = 3.0$ **in Eq.** (4.1)**. The left hand side is the full view of the room model and right hand side is the zoom-in view of the room closure configuration.**

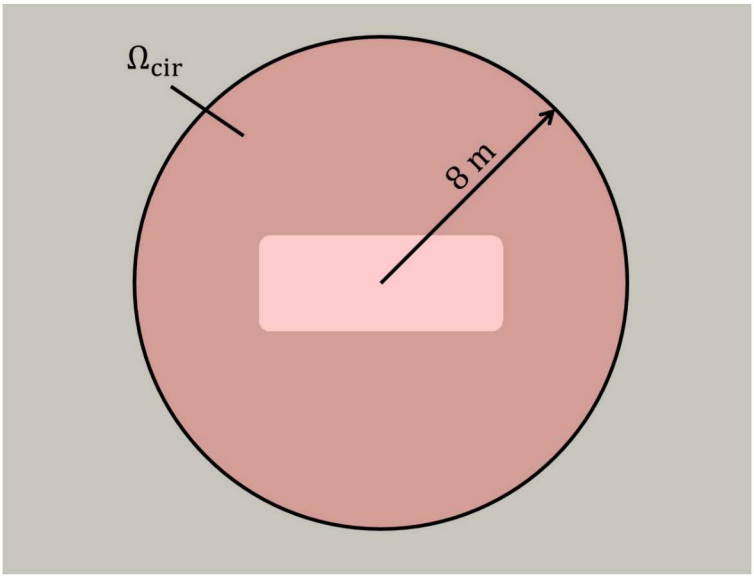

Figure 4-20. Circular area used to calculate the normalize porosity.

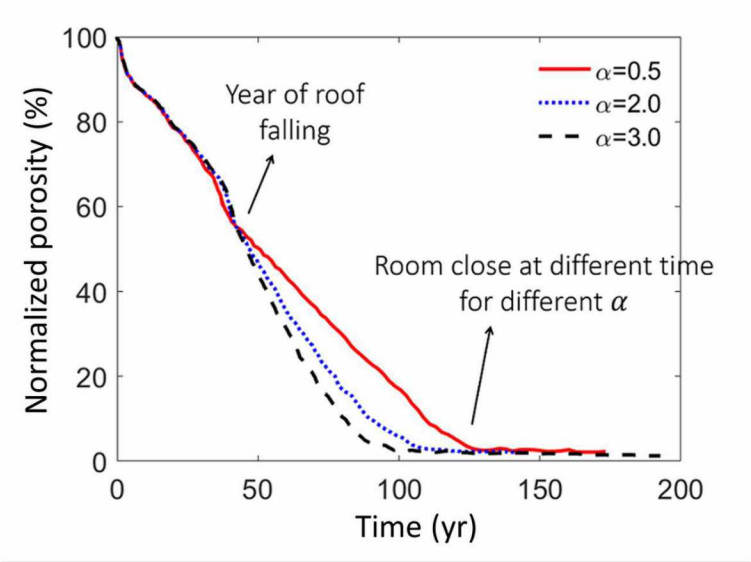

Figure 4-21. Normalized porosity in the empty room closure without clay seam, measured by Eq. (4.16)

clay seam compared to the neighboring salt. Fig. 4-22 shows the discretization of the room with a layer of clay seam in red (initial damage zone). Similar to the previous section, numerical simulations with a clay seam are carried out with α = 0.0, 0.5, 2.0, and 3.0. Except for the existence of the clay seam, the remaining numerical settings are the same as those employed in the cases without a clay seam in Section 4.4.2.2.

In order to obtain more accurate damage patterns under the influence of the clay seam, the stress is allowed to equilibrate before the viscoplastic rate is scaled up at time $t = 0$. During this stress equilibrium period, strong damping is applied and damage evolution is suppressed. First, the stress is initialized to zero in the entire domain. Second, the magnitude of the traction boundary

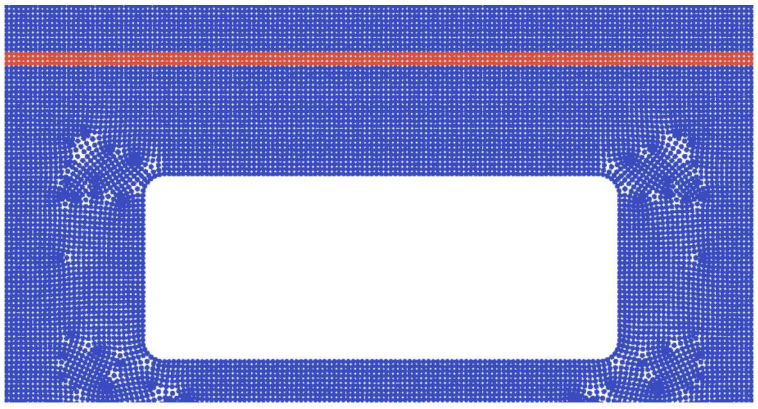

Figure 4-22. Discretization of empty room with clay seam model.

condition and gravity are gradually increased to their target values. Third, the traction boundary condition and gravity are held constant while the stress fields reach steady state.

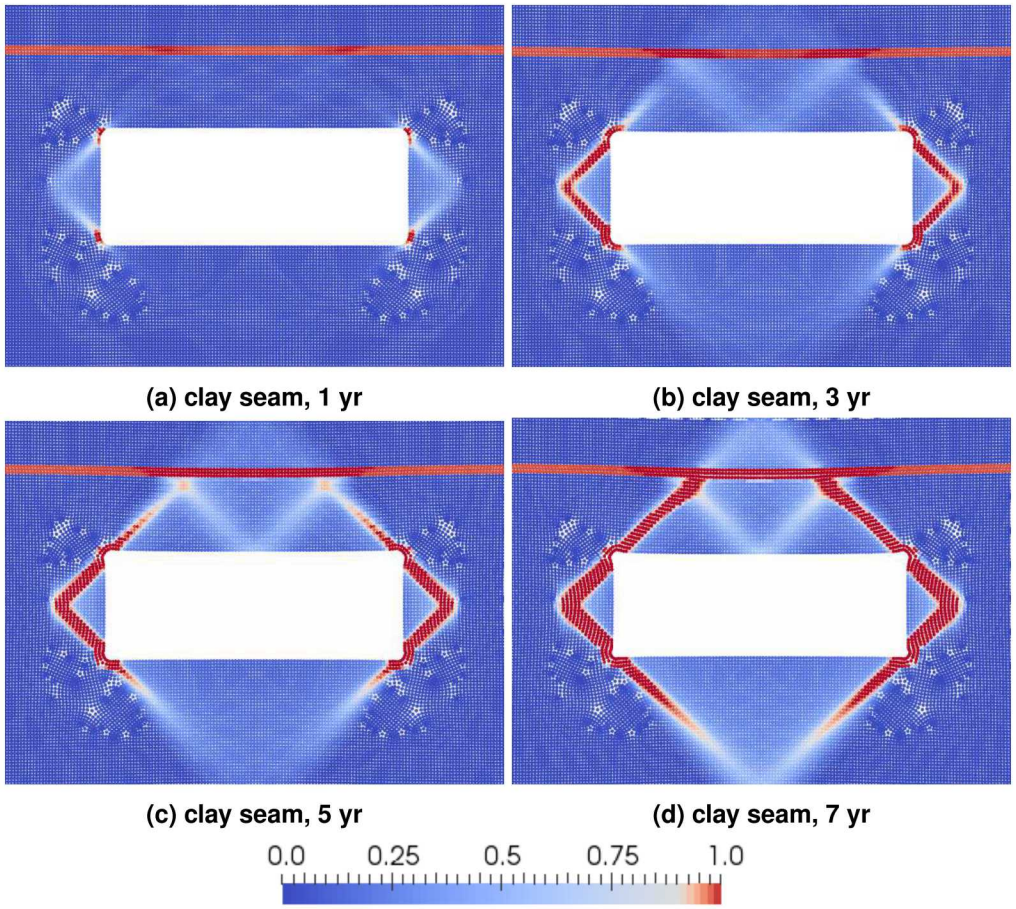

Figure 4-23. Damage propagation of modeling the empty room closure with clay seam and $\alpha = 0.5$.

The damage initiation process, prior to the roof fall, is shown in Fig. 4-23. Fig. 4-23 only depicts the results for $\alpha = 0.5$ because the other three values of α produce identical results before the roof fall hits the floor. The damage is initiated at the room corners, forms triangular damage zone at

the side wall, then the damage bands propagate above the roof and beneath the floor. The damage bands propagating above the roof intersects with the clay seam at approximately 7th year, as shown in Fig. 4-23d. Different from the clay-seam-free cases, a slightly damaged diagonal band is formed in the middle of the roof.

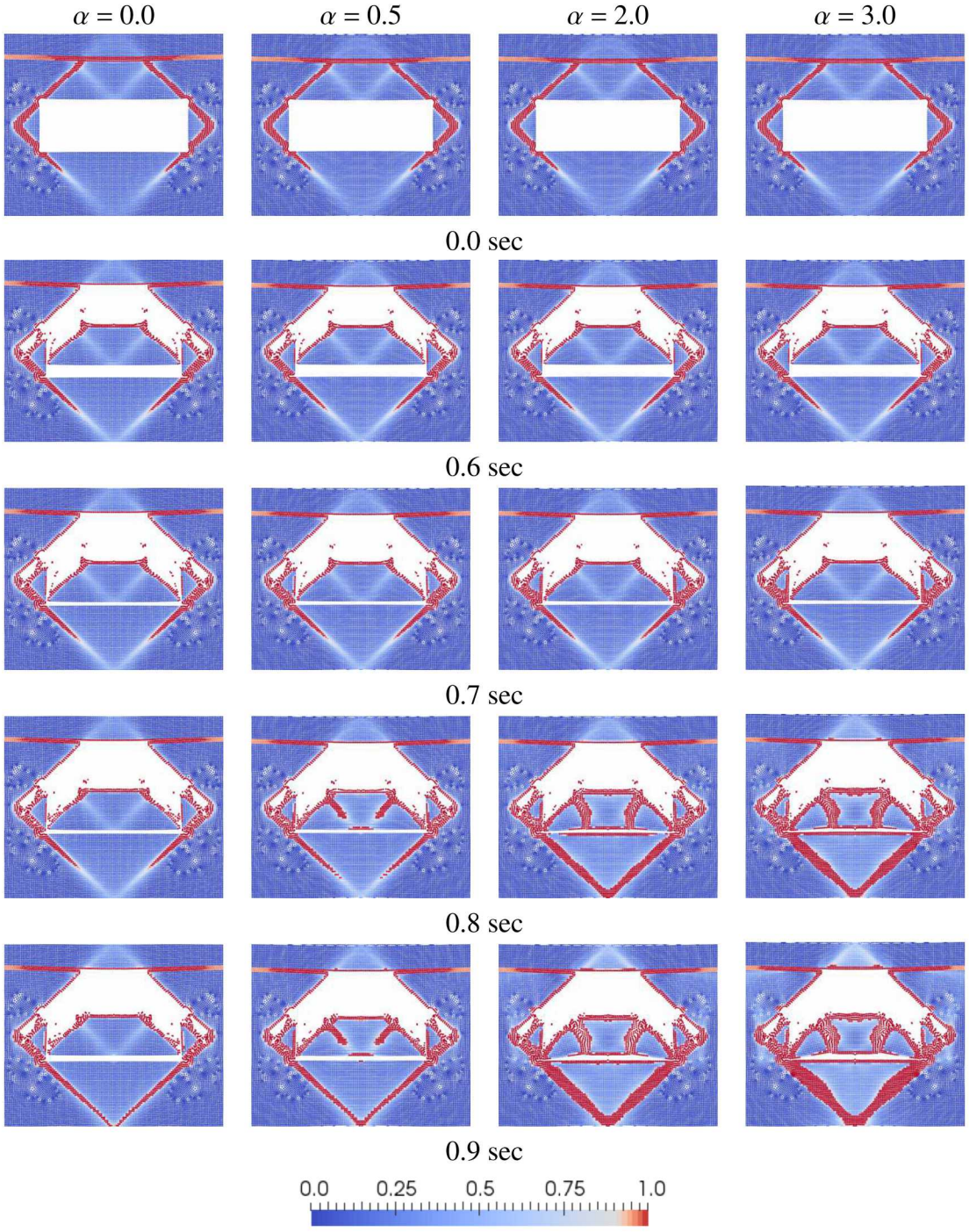

Figure 4-24. The roof falling process at the 7th year in empty room modeling with clay seam.

The roof falling processes in the clay-seam case of α =0.0, 0.5, 2.0, and 3.0 are shown in Fig.

4-24. Similar to the results of the cases without the clay seam, with a larger α (α = 2.0 and 3.0), more severe damage appears in the falling rock after the roof-floor impact. Compared to the results of the cases without the clay seam, the existence of the clay seam leads to faster damage evolution above the roof, earlier rock fall starting time, and more damaged bands in the falling rock, which subsequently results in more damage after impact with a smaller value of α (see the cases of α = 0.5 in Fig. 4-17 and Fig. 4-24.). These results of the clay seam model with more complicated damage patterns and roof falling behaviour again demonstrate the effectiveness and capability of the proposed RKPM framework.

Fig. 4-25 shows the room closure process after the roof falling in the clay-seam case of α = 0.0, 0.5, 2.0, and 3.0. Similar to the results of the cases without the clay seam, the room with a larger value of α (α = 2.0 or 3.0) closes earlier than the room with a smaller α (α = 0.0 or 0.5). The final closed-room configuration of these cases and their corresponding closure times are shown in Fig. 4-26. It is observed that several pieces of undamaged rock are surrounded by damaged rock after the compaction. The results show a consistent observation compared to the cases without the clay seam that the more damaged rocks the closed room has, the faster the room closes. Compared to the results of the cases without the clay seam, the existence of the clay seam leads to faster room closure, more severe rock damages, and more complicated compacting behaviour. These could possibly be due to the earlier roof fall starting time and rock sliding along the clay-seam layer.

Finally, we employ Eq. (4.16) to obtain the temporal normalized porosity of the cases with clay seam, as shown in Fig. 4-27. It can be found that the normalized porosity is reduced by 20% by creep-damage before the roof fall starts. After the roof falling, all the simulated rooms close around the $35^{th} - 40^{th}$ year. The evolution of the normalized porosity are consistent with the the numerical results in Figs. 4-24 - 4-26.

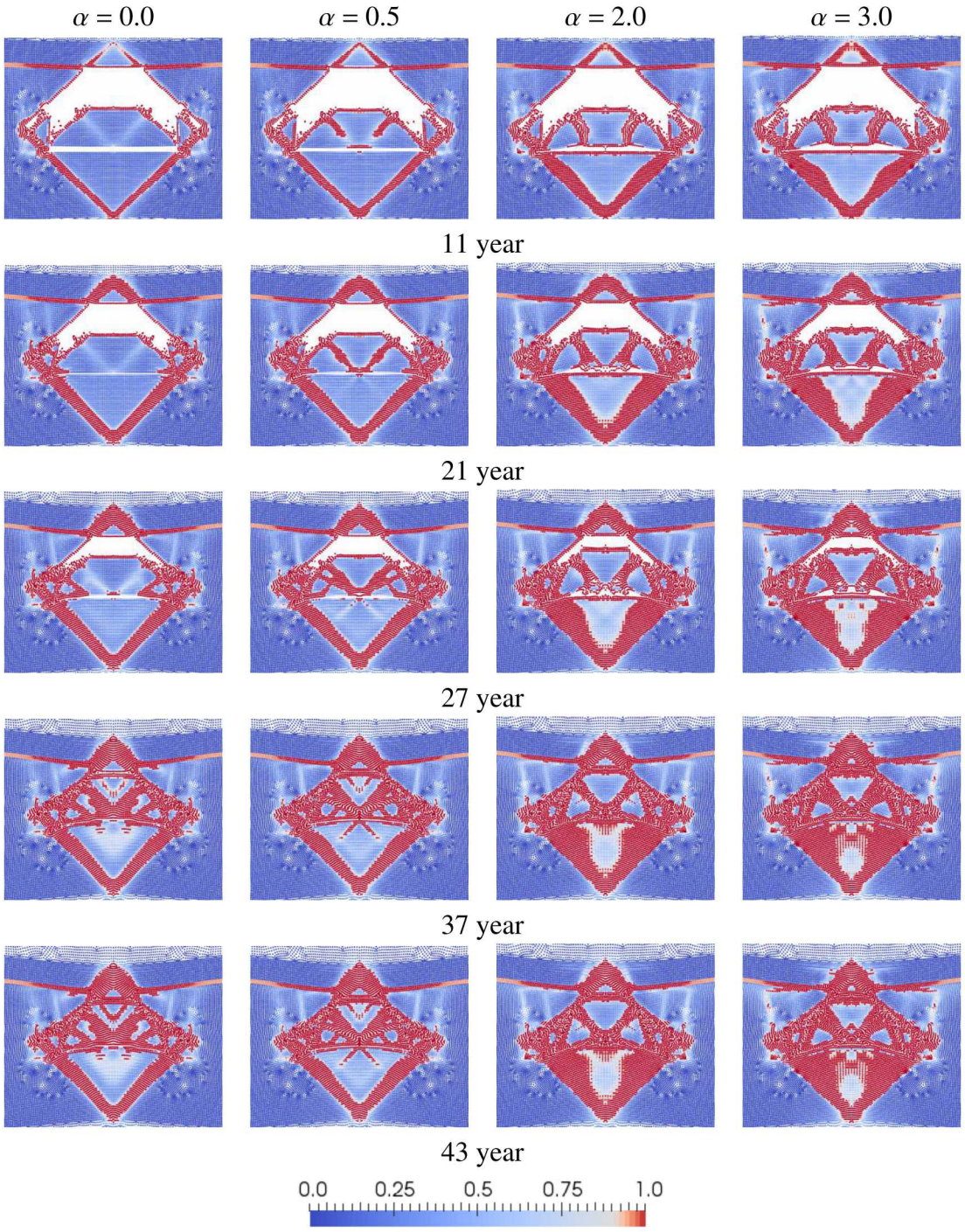

Figure 4-25. The room closure process following after the roof falling in the clay seam model

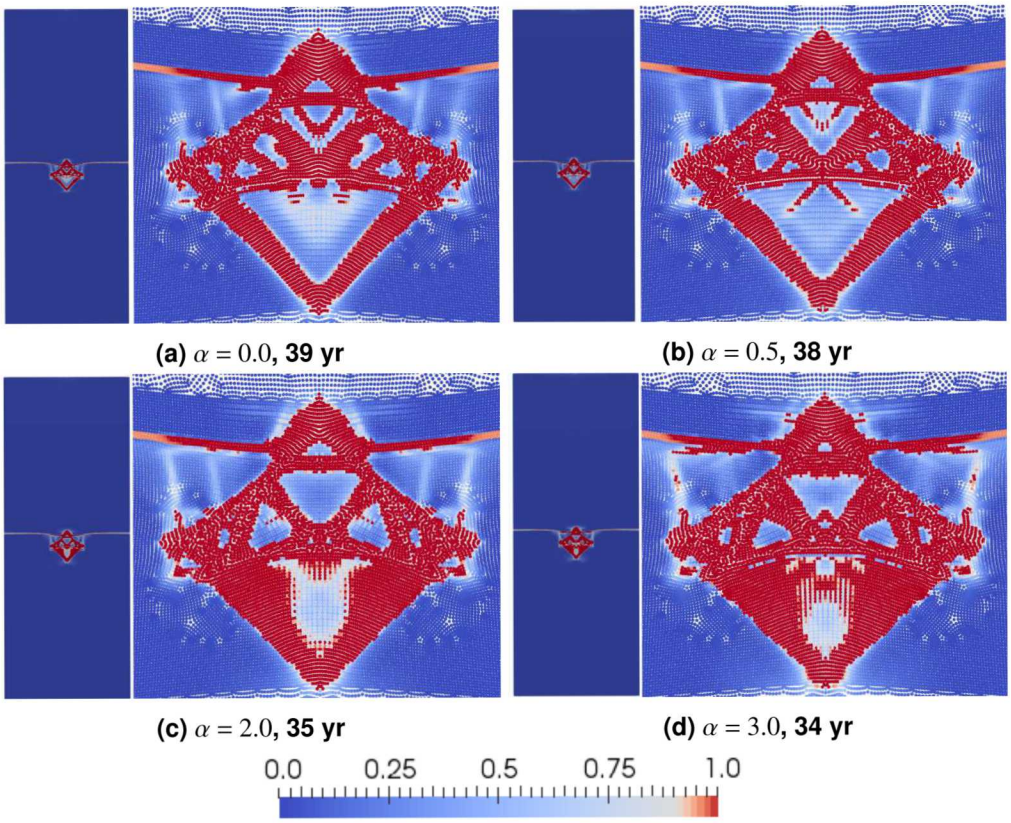

Figure 4-26. Final room closure configuration and the corresponding closure time for the cases with clay seam and (a) $\alpha = 0.0$, (b) $\alpha = 0.5$, (c) $\alpha = 2.0$, and (d) $\alpha = 3.0$. The left hand side is the full view of the room model and right hand side is the zoom-in view of the room closure configuration.

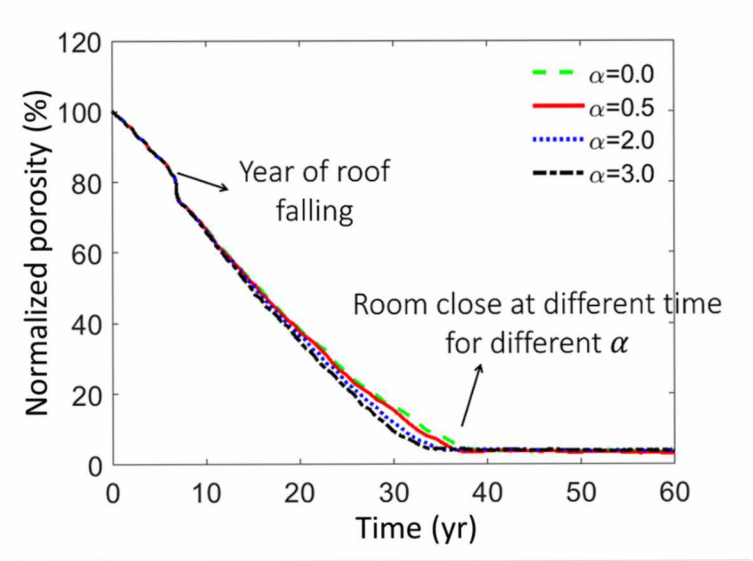

Figure 4-27. Normalized porosity in the empty room closure with clay seam.

4.5. Summary

In this study, a robust semi-Lagrangian RKPM based computational framework has been introduced and enhanced for creep-damage modeling of empty room closure and roof falling processes defined under the WIPP project. The domain of underground rock salt is discretized by meshfree nodal points, which naturally avoids numerical difficulties associated with mesh distortion or entanglement when large deformation occurs. For effective numerical integration, the variationally consistent naturally stabilized nodal integration (VC-NSNI) (Chen et al. 2013) is employed for optimal convergence by enforcing variational consistency. The low energy modes are suppressed by introducing an implicit gradient type regularization (Hillman and Chen 2016). In order to overcome the issue of spurious mesh dependency in modeling damage localization, a reproducing kernel strain regularization (RKSR) (Chen et al. 2004) is introduced. In RKSR, a gradient type regularization is embedded in a RK shape function, which ensures discretization-independent and convergent computation with relatively small computational cost. To address the issue of pressure oscillation, we additionally developed a new simplified pressure projection technique where the volumetric stress is projected onto a lower dimensional space to avoid Ladyzhenskaya-Babuška-Brezzi (LBB) instability. To demonstrate the RKPM capability of modeling roof falling and compaction, an adaptive time scaling approach is introduced to the simulation of room closure.

The effectiveness of the proposed meshfree framework for the creep-damage modeling is verified by solving a notched bar compression benchmark problem before performing room closure and roof fall simulation. The RKSR regularization and pressure projection methods improve the numerical accuracy and stability of the creep-damage model, as shown in the notched bar compression test, and a similar approach has been applied to simulation of room closure problems.

Compared to the reference solution of a creep-driven room closure problem provided by Sandia National Lab (SNL), the proposed RKPM has shown reliable solution. The computational efficiency in parallel computation are also investigated.

The contribution of the elastic strain rate on the damage evolution is introduced to the damage model to study the effects of the material's brittleness on the rock damage patterns during the roof-floor impact processes. The numerical results of simulation models with and without the clay seam consistently show that more pronounced damage is produced by the roof-floor impact when higher brittleness is introduced, which leads to faster room closure as shown in the normalized room porosity history. This could be attributed to the smaller resistance of widely damaged rock bed against creep deformation, which indicates the need to investigate effects of damage and healing of rock on creep and compaction.

The clay seam promotes the damage evolution in area between the roof and seam, leading to much earlier roof fall initiation (at approximately the 7th year) compared to the case without clay seam with the roof fall starting time at approximately the 39th year. Such an early initiation of roof falling, along with the rock sliding on the clay seam in the stage of creep, significantly shortens the room closure time from approximately 120 years to 35 years, again, as shown in the study of the normalized room porosity history.

In summary, the RKPM based simulations demonstrated its capabilities in modeling damage evolution, rock separation, roof fall, and compaction, which are difficult to be modeled by conventional mesh-based methods. This study shows a high potential for using the proposed computational framework and numerical algorithms for assessment of nuclear waste isolation at the WIPP.

4.6. Future Work

Based on the lessons learned from this preliminary study, and considering the multi-scale and multi-physics properties involved in the assessment of the nuclear waste isolation in geologic salt formations, we propose the following future works as a continuation of this effort.

- Employment of RKPM porous media formulation for simulation of brine transport through the rubble pile and excavation damaged zone (Wei et al. 2016).
- Node-based algorithms for computing porosity and permeability of damaged rock salt at various states of empty room closure.
- Development of the healing model of rock salt during compacting process.
- Three-dimensional simulation of the empty room closure.
- Investigation on the influence of rock salt heterogeneity on the roof falling and room closure failure mechanisms.

5. CONFORMING REPRODUCING KERNEL SIMULATIONS OF EMPTY ROOM CLOSURE

Author: Jacob Koester[‖]

5.1. Introduction

The Conforming Reproducing Kernel (CRK) method is a variant of the reproducing kernel particle method that is designed to improve the imposition of essential boundary conditions and the predictions for non-convex or multi-body domains (Koester and Chen 2019). It was recently developed in an LDRD project at Sandia that targeted an improved design-to-solution workflow (Koester et al. 2019).

As in Chapter 4, a reproducing kernel approximation is used. However, traditional kernel functions, typically defined using Euclidean metrics, are replaced with mesh-based functions. The mesh is used to provide boundary information, allowing functions to conform to the domain instead of bleed over boundaries or interfaces as in traditional RKPM. The mesh also provides a structure that is used for domain integration and for visualization.

The conforming reproducing kernel functions are constructed in the reference configuration and used in a total Lagrangian Galerkin formulation. Two domain integration techniques are commonly used, the stabilized conforming nodal integration (SCNI) (Chen et al. 2001) and an $\overline{\boldsymbol{F}}$ that was developed for improved predictions of nearly incompressible materials (Moutsanidis et al. 2019). The pinball method (Belytschko and Neal 1991) is used to enforce contact.

5.2. Model Setup

The CRK method was used to simulate empty room closures and compared to solutions using the selective deviatoric (SD) hexahedral element in SierraSM Sierra/Solid Mechanics (2019). Three discretization levels were simulated and the symmetry of the problem was utilized, see Table 5-1 and Fig. 5-1. The hexahedral meshes were used directly for the SD hexahedral simulations and were converted to tetrahedral meshes, using Cubit's 'htet' command, for use with CRK. Contact was considered to be frictionless.

The current CRK implementation explicitly integrates the equations of motion. Explicit time integration is typically used to simulate events that last less than a few seconds, but hundreds of years were required here. To accelerate the simulation, the viscoplastic scaling rate described in

[‖]Sandia National Laboratories, P.O. Box 5800, Albuquerque, NM 87185, USA

Section 2.2.4 was used with an initial value of $s_0 = 10^{-2}$ and a ramp rate of $s_1 = 2 \times 10^9$ s^{-1}. Explicit time integration was also used for the SD hexahedral FEM simulations with a simulation using implicit time integration on the fine mesh being completed for reference.

Table 5-1. Discretizations used in the CRK empty room closure simulations

Mesh	Nodes	Elements (for FEM analysis)
Coarse	3520	1674
Mid	13348	6503
Fine	52414	25864

5.2.1. Salt Model

The salt model described in Section 2.2.3 was implemented into LAMÉ (Scherzinger and Lester 2019). (Sierra/Solid Mechanics (2019) and CRK both utilize LAMÉ as their library of material models.) The model implementation uses forward Euler approximations to derivatives in order to explicitly integrate the ordinary differential equations in Section 2.2.3.1. If the time step size supplied to the model's numerical implementation exceeds the time step limit provided by equation (53) in Cormeau (1975), then the model uses the time step limit to sub-step through the total time step. Note that the time step limit in Cormeau (1975) is only strictly valid for elastic-viscoplastic models with secondary creep. Cormeau (1975), however, commented that the time step limit seems to work well in models with strain hardening, so we have assumed it also works well in models with damage.

A triaxial compression creep verification of the numerical implementation is plotted in Fig. 5-2. See Section 2.2.3.3 for a derivation of an analytical solution for the salt model's response to triaxial compression creep, and see the "Verification" column in Table 2-1 for the parameter set used in this verification. A tilde above a variable ($\tilde{\cdot}$) in Fig. 5-2 denotes the analytical solution for that variable, while a variable without a tilde above it ($\cdot$) denotes the numerical solution for the variable. At $t = 0$ d, σ_{zz} and σ_{rr} increase from 0 MPa and 0 MPa to 18 MPa and 5 MPa, respectively, causing $\bar{\sigma} = 13$ MPa and $\bar{\sigma}^{db} = 11.33$ MPa. This stress state is held for the next 50 days, leading to secondary and tertiary creep. The numerical and analytical solutions for the damage and total strain agree quite well.

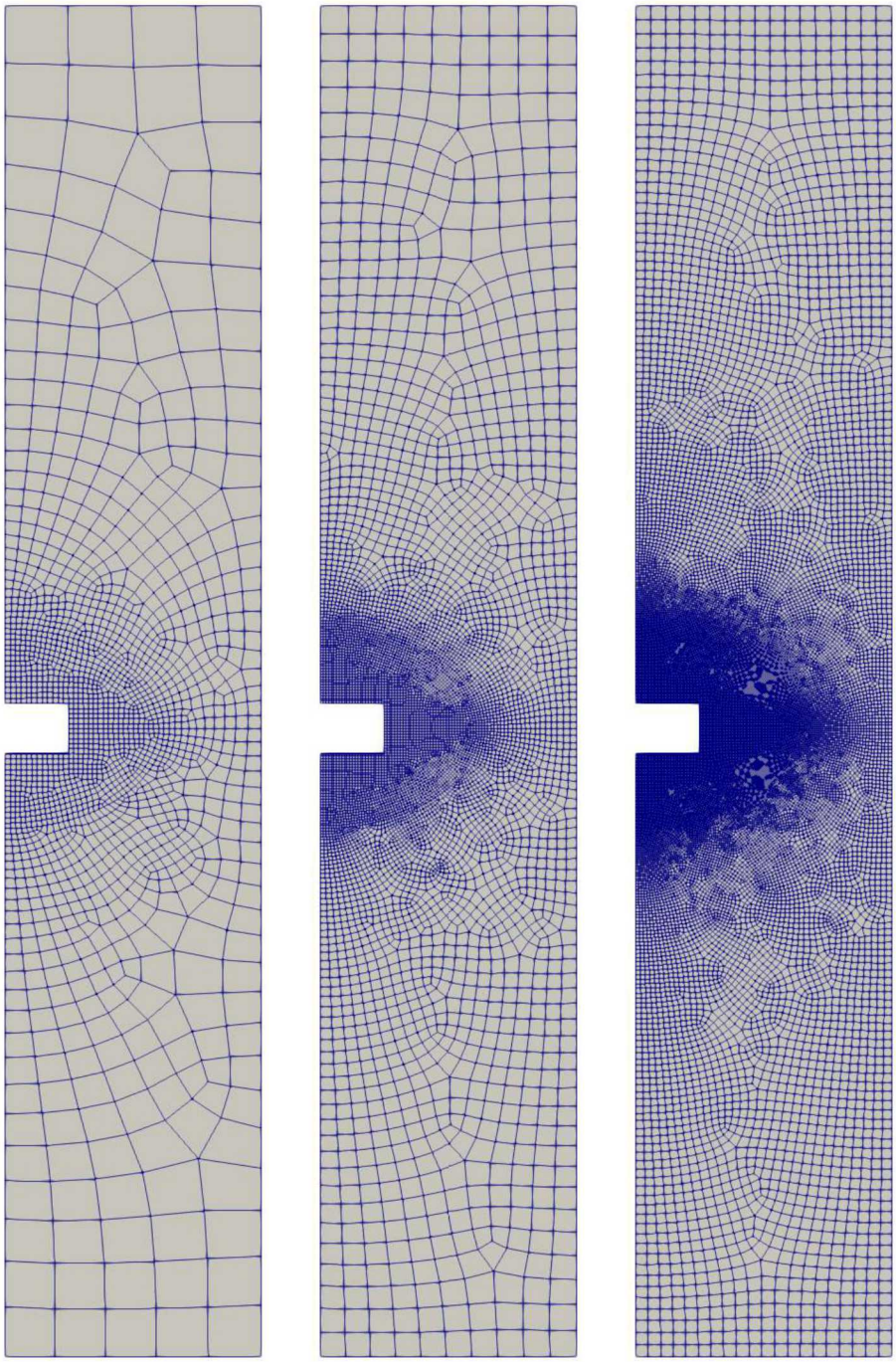

Figure 5-1. Meshes used in the CRK room closure predictions.

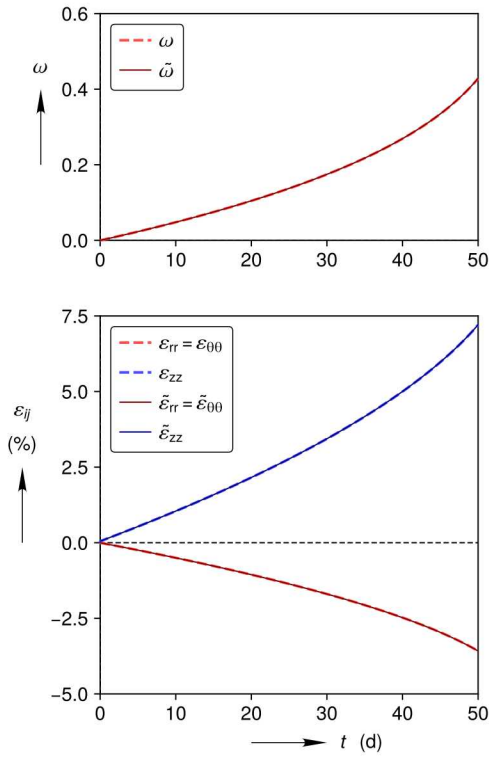

Figure 5-2. Triaxial compression creep verification test.

5.3. Results

CRK predictions for the vertical and horizontal room closures versus time are compared to SD hex solutions in Fig. 5-3 and Fig. 5-4. Images of the deformed room are also provided in Fig. 5-5. The different discretizations provide very similar predictions, showing the coarse discretization is already sufficiently converged. The predictions also agree with the reference solution. The pinball contact method provides an approximate yet explicit representation of the contacting surfaces. As a result, the surfaces are able to come together without the residual gap that is present with the immersed meshfree and semi-Lagrangian RKPM predictions provided in the previous two chapters.

Images of the hydrostatic stress field predictions are provided in Fig. 5-6. For nodal integration, conforming nodal domains are constructed using the barycentric dual of the input tetrahedral mesh. These domains are also used for the $\overline{\boldsymbol{F}}$ predictions where two nodal domains are used to represent one volumetric domain with each volumetric domain containing four deviatoric domains. The nodal integration technique shows nonphysical displacement and pressure oscillations. These oscillations are greatly reduced when using the $\overline{\boldsymbol{F}}$ technique.

Finally, a parallel processing strong scaling study was completed using a mesh with 48,962 nodes and is compared to the performance of a selective deviatoric hex-based simulation using the same mesh (24,038 elements). The analyses were completed on a single node of the Uno cluster and used 1,2,4,8 and 16 processors. Both the SCNI and $\overline{\boldsymbol{F}}$ method were studied and normalized

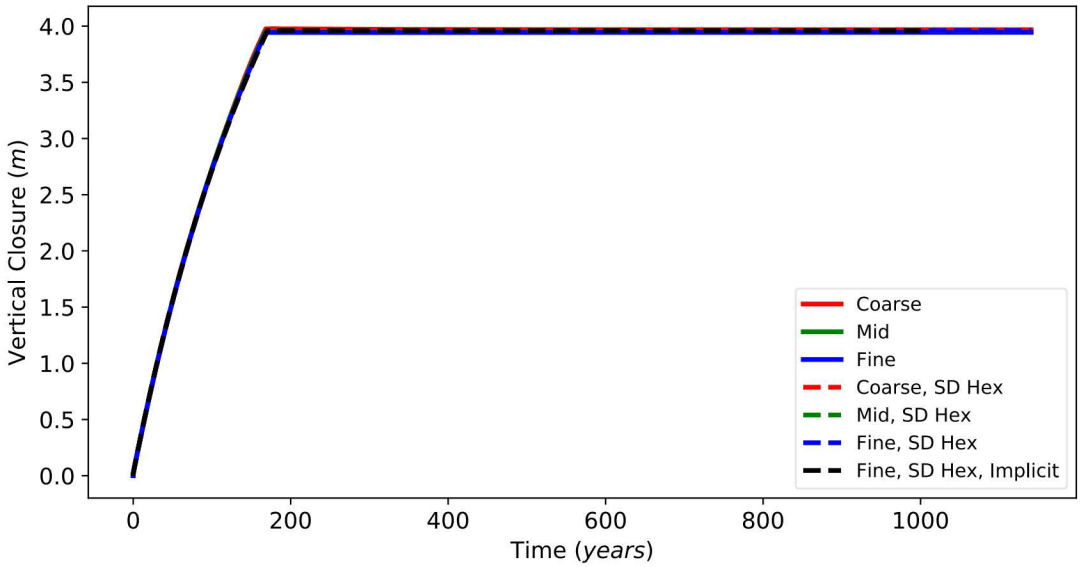

Figure 5-3. Vertical room closure, CRK predictions.

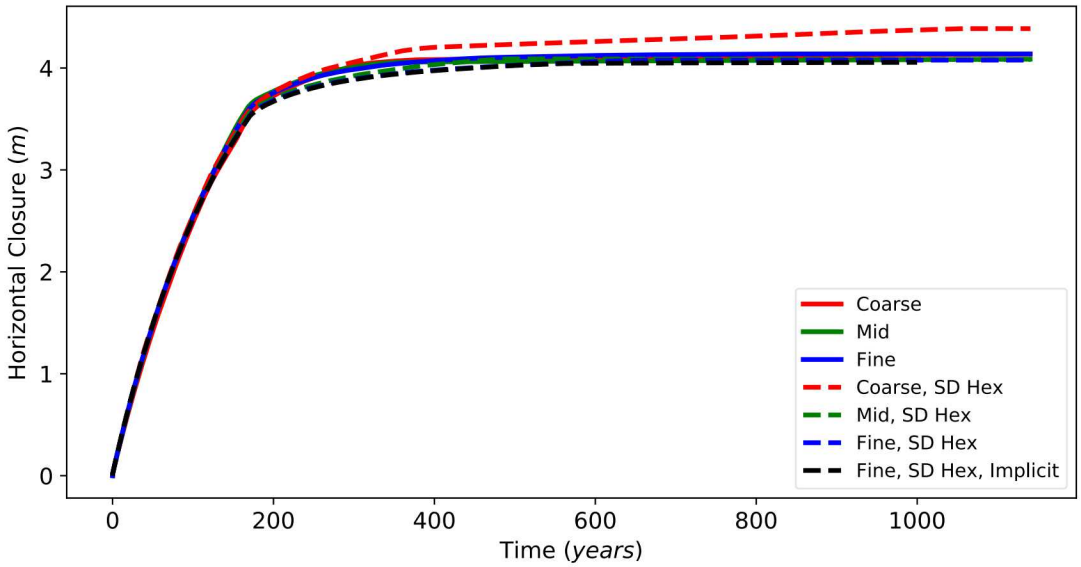

Figure 5-4. Horizontal room closure, CRK predictions.

support sizes of 1.1, 1.6 and 2.1 were used. The scaling appeared insensitive to the integration type and support size and compared agreeably with the selective deviatoric hex simulations.

Stable momentum balance time step size $\Delta t^{\text{mb}}_{\text{max}}$, clock time per time step Δt^{clock}, and clock time per momentum balance time step size $\Delta t^{\text{clock}} / \Delta t^{\text{mb}}$ is provided in Table 5-2. Although Δt^{clock} was about 1.3× to 3× bigger for CRK than the selective deviatoric hexahedral element, $\Delta t^{\text{mb}}_{\text{max}}$ was also about 2× larger for CRK, resulting in comparable values of $\Delta t^{\text{clock}} / \Delta t^{\text{mb}}$.

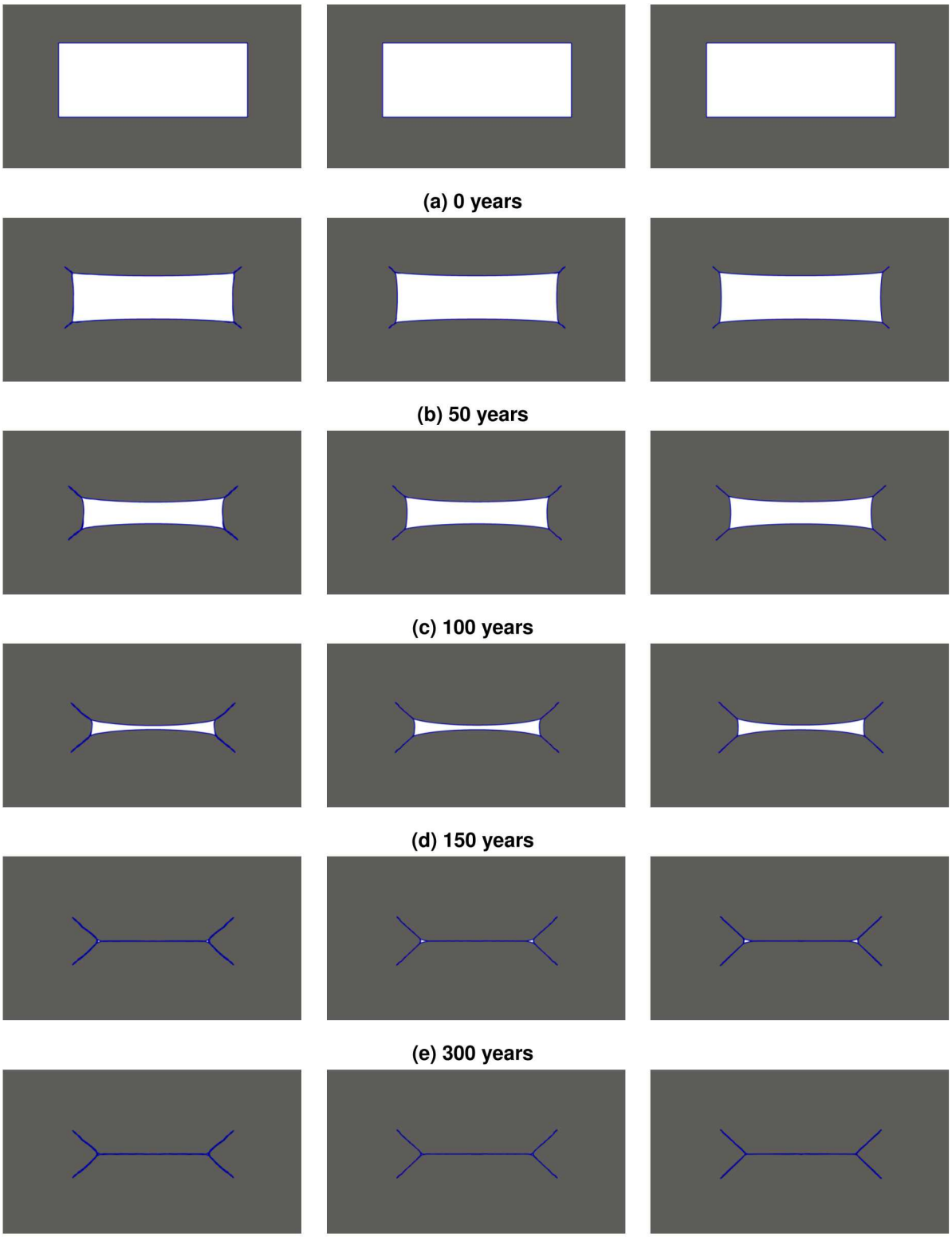

Figure 5-5. CRK room closure predictions. Coarse mesh (left), mid mesh (center) and fine mesh (right).

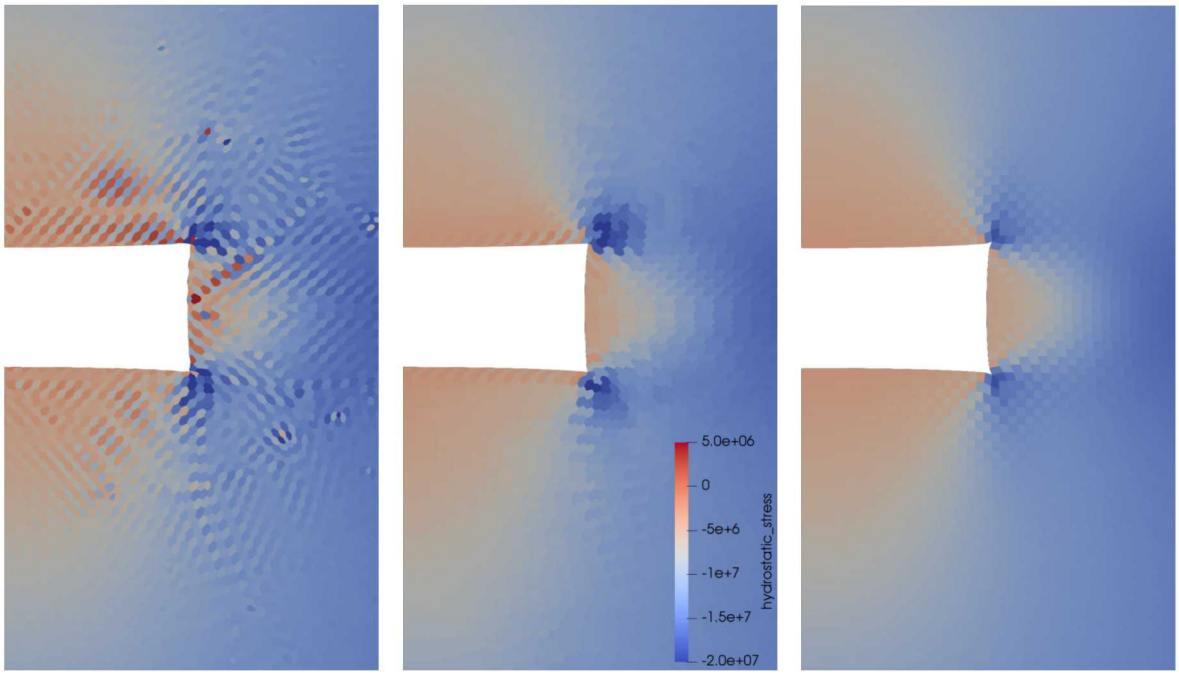

(a) CRK, Nodal (b) CRK, $\overline{F}$ (c) SD Hex

Figure 5-6. Hydrostatic stress predictions in early room closure.

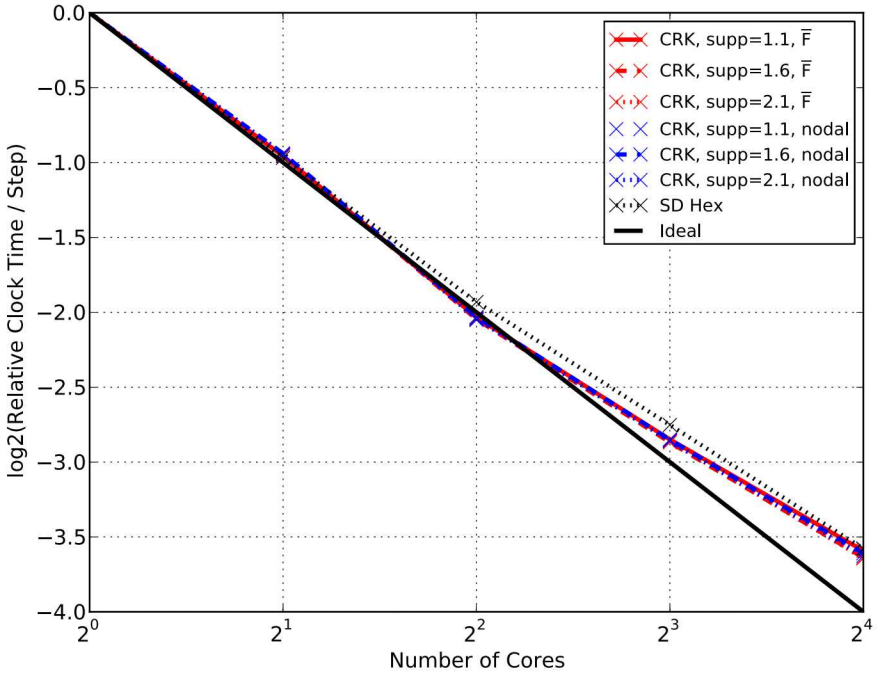

Figure 5-7. Strong scaling study for a mesh with 48,962 nodes and 24,038 hex elements. Analyses were run on Sandia's Uno compute server.

Table 5-2. Stable time increment and performance of CRK compared to FEM using the selective deviatoric hexahedral element. The discretization contained 48,962 nodes and 24,038 elements and 1 CPU on Sandia's Uno compute server was used.

Method	Support	Integration Type	$\Delta t^{\text{mb}}_{\text{max}}$ (seconds)	Δt^{clock} (seconds)	$\frac{\Delta t^{\text{clock}}}{\Delta t^{\text{mb}}}$ (second/second)
CRK	1.1	$\overline{\mathbf{F}}$	7.224e-05	0.840	10138.3
CRK	1.6	$\overline{\mathbf{F}}$	7.225e-05	1.170	14699.2
CRK	2.1	$\overline{\mathbf{F}}$	7.224e-05	1.528	19614.8
CRK	1.1	Nodal	7.224e-05	0.627	7926.1
CRK	1.6	Nodal	7.226e-05	0.907	11768.5
CRK	2.1	Nodal	7.224e-05	1.280	16872.9
Hex	N/A	Selective Deviatoric	3.418e-05	0.473	11198.5

5.4. Future Work

The next step is to simulate roof collapse and rubble pile compaction. A bond-based failure approach is used in the CRK method (Koester et al. 2019). An initial attempt uncovered robustness issues with the interaction of the bond-based approach and the material constitutive model. After these robustness issues are resolved the simulations can be performed, starting in two dimensions and followed by three dimensions.

After roof collapse simulations are complete, the bond-based failure approach and contact method can be further evaluated. The bond-based approach was designed to regularize the failure predictions and has been demonstrated to perform well on problems with Mode-I fractures (Koester et al. 2019). The complicated fracture process that occurs during roof collapse may require further attention. Additionally, contact between fracture surfaces is expected to work but needs to be verified and may also require more work.

6. FURTHER ANALYSIS OF GEOMECHANICAL SIMULATION RESULTS

Author: Benjamin Reedlunn**

6.1. Introduction

Section 1.2 presented two arguments why a collapsing room was anticipated to fully close slower than a gradually closing room, where fracturing was suppressed. First, fracturing around a room is expected to cause square and rectangular room cross-sections to transition to more circular cross-sections. Circles close more slowly than other two-dimensional shapes because circles distribute the stress around a room more evenly. Second, the rubble pile within a collapsing room supplies back pressure to the surrounding rock formation, which reduces the deviatoric stress in the surrounding rock and slows down the rate of room closure.

To assess whether a collapsing room is, in fact, predicted to close slower than a gradually closing room, it is helpful to define the relative (normalized) porosity ϕ/ϕ_0. The current porosity is defined as $\phi = V/V_{\text{enc}}$, where V is the current void volume and V_{enc} is a fixed Eulerian volume that fully encloses V. The original porosity is defined as $\phi_0 = V_0/V_{\text{enc}}$, where V_0 is the original void volume. This relative porosity concept was originally introduced in Section 4.4.2.2 to quantify the closure of a collapsing room, but it is also an appropriate measure for a gradually closing room because $\phi/\phi_0 = V/V_0$.

Surprisingly, both the RKPM and IGA Meshfree simulations predicted a collapsing room would reach its final relative porosity *sooner* than a gradually closing room. The RKPM and IGA Meshfree gradual room closure simulations both predict ϕ/ϕ_0 reaches 4 % about 170 yr after room excavation. (These gradual closure predictions were also confirmed by the FEM and CRK method.) The RKPM simulations of room collapse and reconsolidation predict ϕ/ϕ_0 reaches 4 % in about 110 yr without a clay seam in Fig. 4-21, and about 35 yr with a clay seam in Fig. 4-27. The IGA Meshfree simulations did not explicitly compute ϕ/ϕ_0, but the relative porosity appears to be less than 4 % at $t = 50$ yr in Fig. 3-8.

These predictions of fast collapsing room closure could be due to several factors:

1. Highly damaged salt seems to behave in a somewhat fluid-like manner in these meshless simulations, allowing it to "flow" into open cavities and avoid supplying much back pressure to the surrounding rock formation. Damaged salt can viscoplastically flow more easily than intact salt, so some of this fluid-like behavior may reflect reality, but some may

**Sandia National Laboratories, P.O. Box 5800, Albuquerque, NM 87185, USA

be due to modeling choices. For example, the width of the damage zone depends on the regularization length scale discussed in Section 4.3.1 and contact between damaged regions is assumed to be frictionless.

2. The salt constitutive model does not include healing. If sufficient local confining pressure is developed inside the rubble pile, prior to complete compaction, then rubble pieces could bond to each other and supply back pressure to the surrounding rock formation.
3. Any gases within the room were allowed to escape without supplying back pressure.
4. The RKPM collapsing room simulations only reach $\phi/\phi_0 = 4$ % before ϕ/ϕ_0 stops appreciably evolving. This last bit of porosity may have remained due to the coarse discretizations and implicit representation of contact surfaces. The final closure from $\phi/\phi_0 = 4$ % to nearly 0 % may require a long time with a more accurate numerical representation.
5. The damage fields in Sections 3.3 and 4.4.2 suggest that much of the salt nearest the room sheds stress to the surrounding intact rock formation. (Comparing stress fields instead of damage fields would be a better way to assess this in the future.) This stress redistribution makes the rectangular room cross-section transition into a square or a diamond shape, which both close faster than a circle.
6. Damaged induced stress redistribution also increases the effective room size without changing void volume, and big rooms lose void volume faster than small rooms.

The first five reasons listed above may have accelerated the collapse and reconsolidation process, but they do not explain why the collapsing room closed faster than the gradually closing room, at least prior to $\phi/\phi_0 = 4$ %. Having a room filled with fluid-like, permanently damaged, salt clearly provides more back pressure than the void space of an empty room. Furthermore, a square or diamond still closes more slowly than a rectangle with a 2.54-to-1 aspect ratio. An increase in effective room size due to damage, however, provides a mechanism for collapsing rooms to close faster than gradually closing rooms and deserves further attention.

6.2. Room Size Analysis

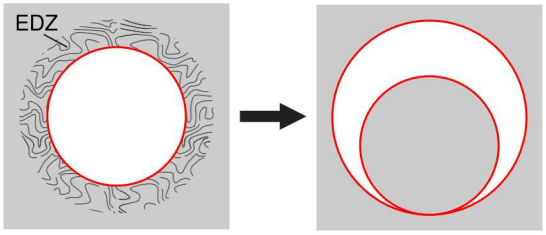

Figure 6-1. A circular room, rimmed with an excavation damaged zone, idealized as a bigger room filled with a commensurate amount of idealized rubble

A simple toy problem is analyzed in this section to demonstrate how damage induced stress redistribution affects room closure. Take a slender and isolated circular room, rimmed with an

excavation damaged zone (EDZ), as shown on the left of Fig. 6-1. If one assumes the EDZ cannot sustain any deviatoric stress, forms a rubble pile in the room, and provides zero back pressure until it has fully reconsolidated, then one can increase the room size to the extent of the EDZ and represent the rubble pile as a circle of intact salt, as shown on the right of Fig. 6-1. Let V_0^{room} and V^{room} respectively be the initial and current volume of the room, ignoring the idealized rubble, and let V_0 and V respectively be the initial and current void volume. The viscoplastic closure of a small room, without an EDZ or a rubble pile, can be compared against that of a big room filled with idealized rubble, provided the big room has the same initial void volume V_0 as the small room. For the analyses compared herein, the big room's initial room volume was twice that of the small room and any gases within the room were allowed to escape without supplying back pressure. See Appendices A.1 and A.2 for further details of the model setup and numerical settings.

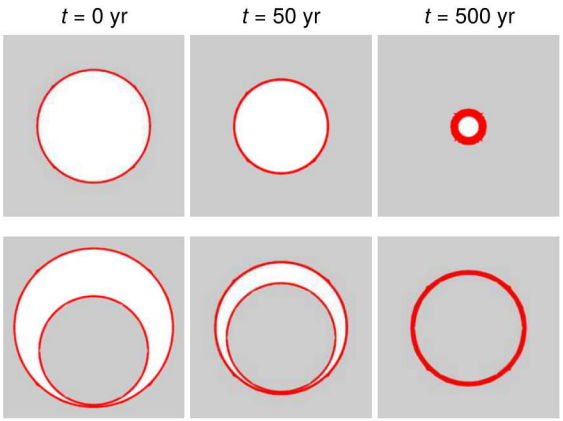

(a) Deformed room shapes at selected times

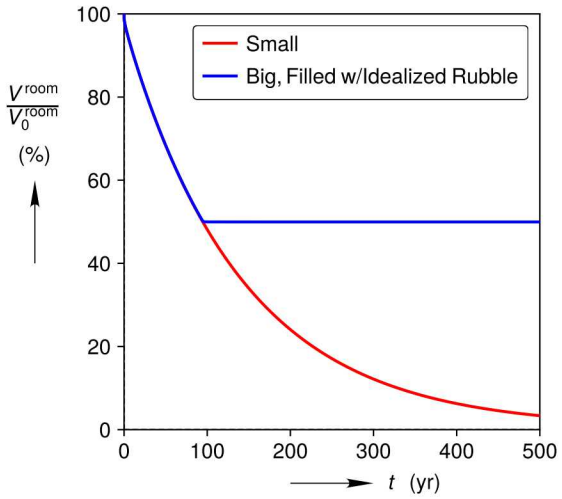

(b) Relative room volume histories

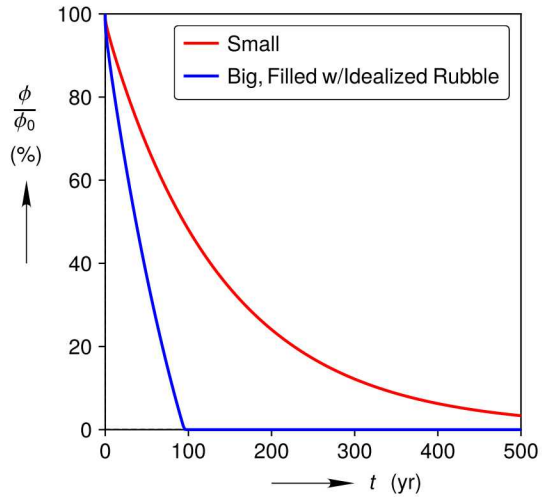

(c) Relative porosity histories

Figure 6-2. The effect of increasing a circular room's diameter and filling it with a commensurate amount of idealized rubble.

As depicted in Fig. 6-2, increasing the room size, while holding the initial void volume constant, dramatically shortens the time to close a room. Fig. 6-2a presents the room cross-sections at $t = 0$,

50, and 500 yr, where the layer of finite elements closest to the room and surrounding the idealized rubble has been colored red. The small and big rooms have the same *relative* room volume $V^{\text{room}}/V_0^{\text{room}}$ prior to $t = 95$ yr, as shown in Fig. 6-2b. At $t = 95$ yr, however, the surface of the big room contacts the idealized rubble and the big room is effectively closed. Alternatively, one can also plot the same results as ϕ/ϕ_0 versus t, as shown in Fig. 6-2c. In this depiction, it is more clear that the big room is fully closed at $t = 95$ yr, while the small room remains open even after 500 yr. Another way of describing these results is the big and small room are constrained to have the same void volume, yet the big room loses *absolute* void volume faster than the small room.

Two, more academic, observations can be made about the $V^{\text{room}}/V_0^{\text{room}}$ curves prior to $t = 95$ yr. First, the viscoplastic closure of a long and slender horizontal circular room, whose diameter is small compared to the lithostatic pressure gradient, is similar enough to viscoplastic closure of a slender vertical borehole that the results can be compared. Liu et al. (2011) developed an analytical solution for the vertical borehole through a Perzyna, Norton power-law, material without hardening. They found that R/R_0, where R is the current borehole radius and R_0 is the original borehole radius, is independent of R_0 in their equation (104), which is analogous to the observation that $V^{\text{room}}/V_0^{\text{room}}$ is independent of initial room size. Second, $\log(V^{\text{room}})$ versus t is essentially a straight line*, which means $(\mathrm{d}V^{\text{room}}/\mathrm{d}t)/V^{\text{room}}$ is virtually a constant. The initially circular room remains essentially circular and the only length scale is the diameter of the room, so the room volume loss rate is virtually a constant after dividing by the room volume.

6.3. Ventilation Drift Collapse at the Teutschenthal Mine

Section 1.3 mentioned the closure of ventilation drifts in a potash seam at the Teutschenthal Mine in Germany. The current author initially found these drift closures "interesting", but they appear more relevant now, in light of the analyses in Sections 3.3, 4.4.2 and 6.2. The ventilation drifts were originally excavated in 1962, but in 1996 a nearby region of the mine collapsed due to a rock-burst, accelerating the ventilation drift closure. The ventilation drifts were then re-excavated in 2016 (Popp 2019). Re-excavation revealed the rubble pile within the ventilation drifts had reconsolidated to a state that looked very similar to the intact carnallitite potash. Strength and permeability tests confirmed the reconsolidated carnallitite had equivalent behavior to intact carnallitite from the mine only 20 years after the rock-burst. See Popp et al. (2018) and the "Natural Closure of Salt Openings" presentation in Appendix D of Buchholz et al. (2019) for further information.

The remarkably quick reconsolidation of the Teutschenthal ventilation drifts could be due to several factors that (may) differ from rooms at the WIPP. First, carnallitite potash may have faster creep behavior than sodium chloride rock salt. Second, the rubble pile within the ventilation drifts may have been exposed to a substantial amount of moisture during humid German Summers. Third, the collapse of a region near the ventilation drifts likely transferred a significant amount of compressive stress to the ventilation drift pillars and rubble piles. Neighboring drifts may also

*The logarithm of equation (104) in Liu et al. (2011) is also linear with respect to t.

collapse at the WIPP, but the stresses caused by such a dynamic collapse could be significantly different.

Despite the geological and structural differences between the Teutschenthal ventilation drifts and rooms at the WIPP, the analyses in Sections 3.3, 4.4.2 and 6.2 makes it difficult to simply dismiss the rapid ventilation drift closure as an anomaly. The rapid Teutschenthal ventilation drift closure may be representative of what may occur at the WIPP and deserves further consideration.

7. DEVELOPMENT OF METHODS TO CHARACTERIZE PERMEABILITY/POROSITY RELATIONSHIPS AS A FUNCTION OF RUBBLE POLYDISPERSITY

Authors: Edward Matteo[††], Chven Mitchell[††], Robert Lander[‡‡], and Thomas Dewers[††]

7.1. Introduction

Roof collapse at WIPP is of interest in that the resulting rubble piles (see Fig. 1-3) likely consolidate in a manner differently from typical experimental salt consolidation tests, and the resulting flow pathways within the consolidation rubble have not been characterized, particularly in how these are influenced by consolidation. Here we discuss initial progress toward characterizing initial rubble piles using micro-computerized tomography and computational fluid dynamics modeling of gas transport in pore spaces within rubble. We detail methods used to separate segmented binary (solid and fluid) images and determine preliminary particle size distributions of rubble piles using image analysis software. In an initial trial, we show how particle separates are applied in a numerical scheme for particle consolidation. We use image analysis methods to extract a finite element mesh for the pore spaces within initial fractures from the disturbed rock zone and run-of-mine salt and perform example computational fluid dynamics (CFD) simulations of gas transport within representative sub-samples. We discuss paths forward in developing a methodology for modeling empty room rubble pile consolidation and gas transport at WIPP.

7.2. Methods

7.2.1. WIPP Salt Sample Provenance

Two samples of WIPP salt were collected for our initial analysis. These are:

1. WIPP Run-of-mine salt collected and stored in a sealed 10-gallon plastic bucket.
2. A piece of 12-inch drill core from the disturbed rock zone (DRZ).

[††]Sandia National Laboratories, P.O. Box 5800, Albuquerque, NM 87185, USA
[‡‡]Geocosm, 10 Town Plaza #233, Durango, CO 81301, USA

7.2.2. Computerized Tomography and Image Analysis

X-ray micro-computed tomography (X-ray μCT) imaging was performed on salt samples using a North Star Imaging X50 micro-CT scanner and a Perkin Elmer 0822 1622 Digital Image detector, with North Star efX-DR and efX-CT software used for image acquisition and reconstruction, respectively, by Carl Jacques of Sandia's Nondestructive Environments and Diagnostics Department. Tomographic reconstructions were provided in the form of TIFF image stacks with a voxel size of 8.3e5 μm^3 (94 μm × 94 μm × 94 μm). We applied a variety of filters to improve the quality of salt-pore space contrast, including a median filter and edge-preserving smoothing. A segmentation algorithm was then applied to determine, label, and measure particle sizes and shapes of salt particles in the run-of-mine salt, and a particle size distribution was prepared using Excel. The Scan-IP and Scan-FE modules of the Synapsis™ software suite, Simpleware™, were used to visualize connected and unconnected portions of pore networks delineated by the μCT reconstructions and to prepare surface meshes of grain separates, and finite element meshes for the CFD simulations.

7.2.3. Geocosm Cyberstone Modeling

Cyberstone™ is Geocosm's 3D proprietary simulator used by the company in-house (patents pending) to model sedimentation, compaction, and other processes (https://geocosm.net/products/).

7.2.4. CFD Modeling of Gas Transport

Example CFD modeling was performed using COMSOL Multiphysics™ software, using meshes prepared from the Scan-IP software. We used densities and dynamic viscosities of dry air, and modeled the gas transport using steady-state Navier-Stokes equations keeping inertial terms and using a downstream boundary condition at one end of the domain at a constant pressure of 1 atm and an upstream constant flux of 1.0e-4 m/s.

7.2.5. The "Drop" Experiment

The DRZ core piece was initially scanned, and then dropped from a height of 12 feet onto a concrete surface while contained inside a cloth bag (used to contain the fragments). The resulting pieces were placed in a plastic 10-gallon bucket and re-scanned.

7.3. Results

7.3.1. CT Imaging

7.3.1.1. Core of Disturbed Rock Zone

Figure 7-1 shows 2-D radiographs and a 3D reconstruction of the DRZ core piece. In Fig. 7-1A (scale bar is 30 mm), numerous extension fractures oriented parallel to the wall increase in density as the wall is approached (In Fig. 7-1A and Fig. 7-1B, this is the right-hand vertical boundary of the images). The fractures appear black against the grey levels of the salt and other minerals, where salt is the darkest grey, and other evaporite minerals appear as lighter shades.

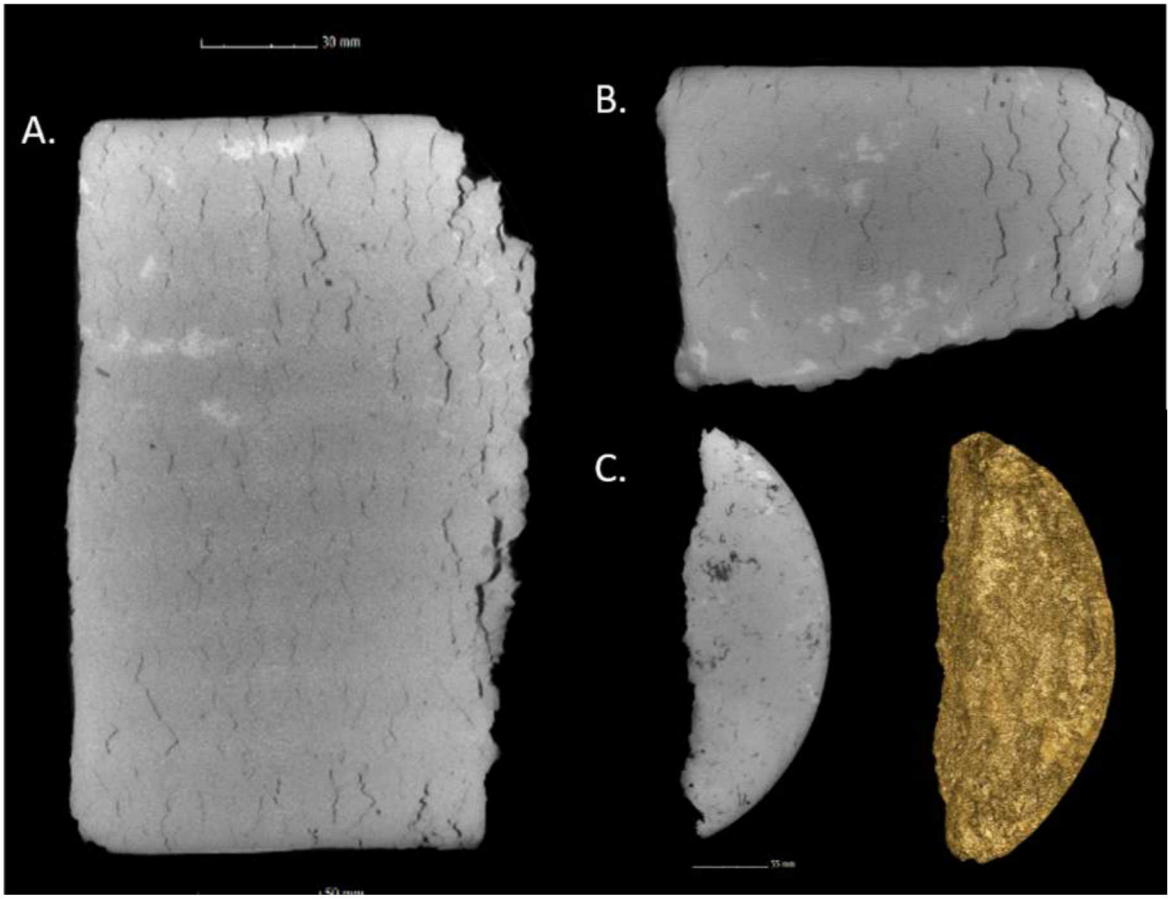

Figure 7-1. X-ray imaging of WIPP DRZ core sample.

7.3.1.2. Sample of Run-of-Mine Salt

The run-of-mine salt sample with included bucket is shown in Fig. 7-2. One can see just from looking at the top of the tomogram that there is a mixture of poorly sorted particles, with numerous flat pancake-like shapes for the larger grains, and more equant grains among the smaller in the distribution. A cross section view of the salt bucket is shown in Fig. 7-3.



Figure 7-2. X-ray tomographic reconstruction of bucket of run-of-mine salt. The bucket is approximately 12” across.

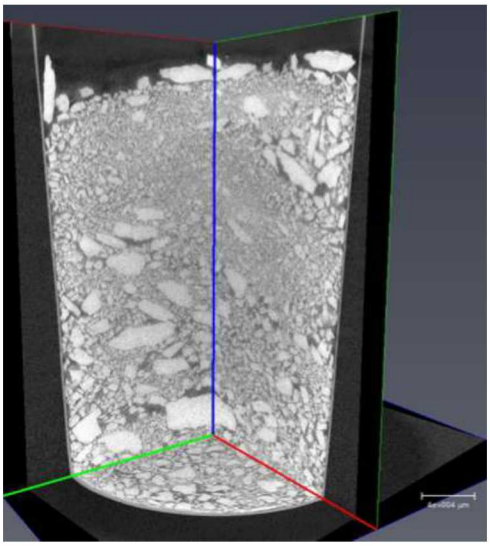

Figure 7-3. Cross section view of run-of-mine salt with voxel size of 94 microns.

7.3.1.3. DRZ Core From “Dropped” Experiment

The DRZ core piece subject to dropping is shown via tomographic reconstruction in Fig. 7-4. The piece has broken into three large pieces and many smaller pieces. Unexpectedly, many of the extension fractures visible in the unbroken piece (Fig. 7-1) survived the fall.

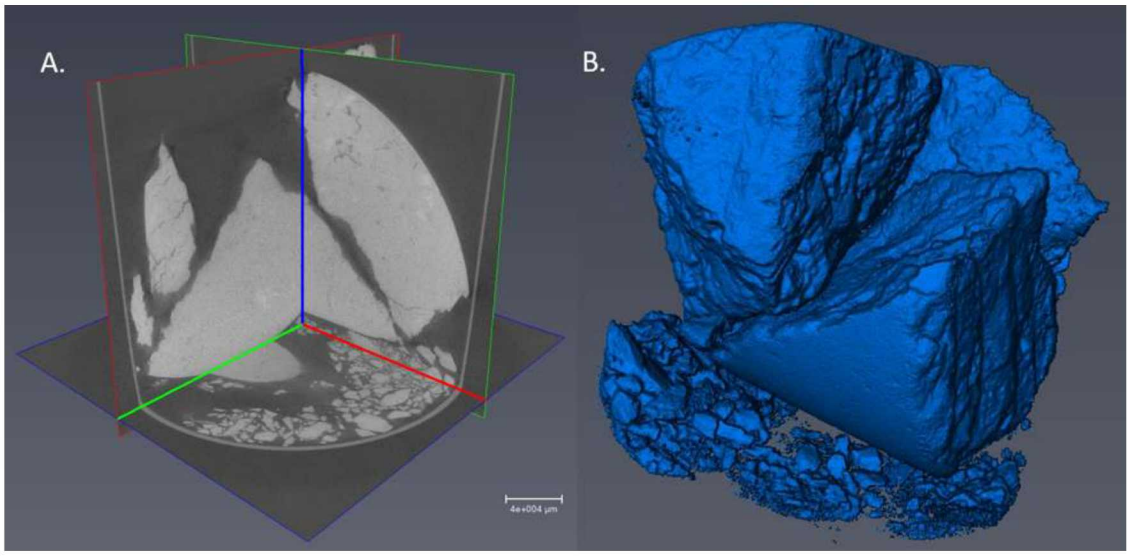

Figure 7-4. X-ray tomographic reconstruction of "dropped" DRZ core piece.

7.3.2. Grain Size Distributions of Run-of-Mine Salt Floor Samples

A preliminary estimation of the grain size distribution of the run-of-mine salt bucket was determined using the Pergeos software, using a small subset of the bucket one decimeter in volume taken from the middle bottom portion of the bucket shown in Fig. 7-3 which is depicted in Fig. 7-5. The image on the left side shows the original grey-level reconstruction from the tiff stack, the image in the middle shows segmented grains, shown in blue, and the right image shows grain separates using a proprietary watershed algorithm for separating grains. The grain separates are shown in different colors. A close inspection shows that several of the larger grains have been separated into two or more smaller grains, but that most of the smaller equant grains have been recognized and separated successfully. It is likely that the Pergeos watershed algorithm works best for equant grains, such as occurs in a well sorted sandstone, and that the larger, pancake-shaped grains are not well separated by the software.

The resulting grain size distribution is shown via a frequency histogram in Fig. 7-6, with particle size shown as a phi-scale (log-base 2) of grains in mm. A bi-modal distribution is evident, and we suggest that most of the more frequent smaller grains below ≈ 1 mm in size (a phi value of ≈ 0.0) can safely be deleted from consideration due to negligible volumes (this is the grain sizes expressed by the blue box; the extreme left side of the distribution with the smallest sizes plotted in Fig. 7-6 are essentially equivalent to just a few voxel sizes, and thus are not well resolved in the image set). In Fig. 7-6, 43,850 grains were recognized, with 3414 grains existing in the greater-than-1 mm size fraction.

7.3.3. Grain Separates

As a proof of concept, we constructed surface meshes in STL format of grain separates, and show how these files can be used in simulations of room rubble consolidation. The Scan-IP software

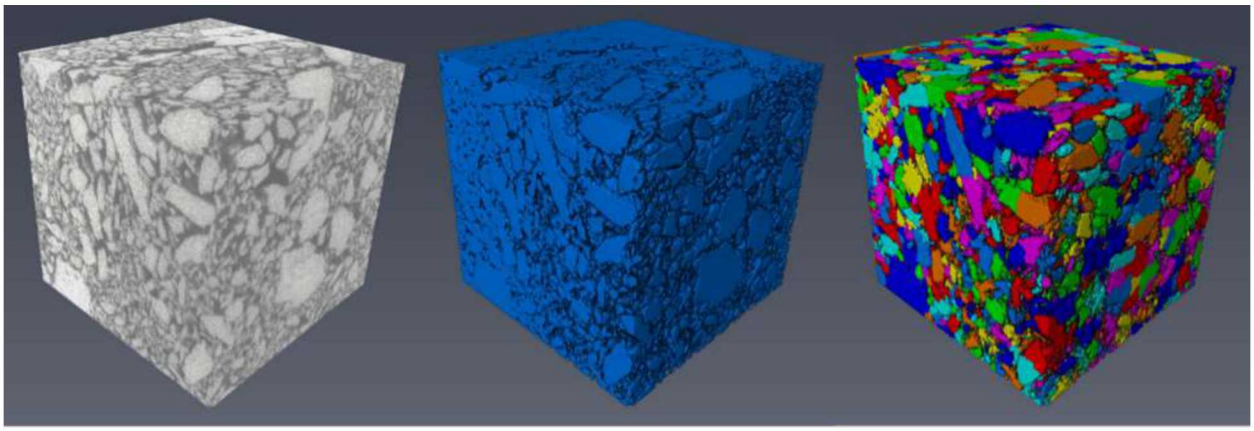

Figure 7-5. Decimeter volume of run-of-mine salt bucket, showing original grey levels (left), segmented solid phase (middle), and separated grains (right).

watershed algorithm was used in a similar fashion to the Pergeos method, and the grain separates are shown in different colors in Fig. 7-7. An STL surface mesh was made from the teal-colored grain, which is discussed in the next section.

7.3.4. Cyberstone™ Modeling

The Geocosm portion of this project involves simulating the deposition and mechanical compaction of rubble that forms in association with clasts that fall from the ceilings of collapsing chambers at the WIPP site. The deposition portion of this work uses rigid-body physics simulations that consider complex 3D shapes for clasts as they collide with the chamber floor and one another. The mechanical compaction phase of the work will use these simulated rubble deposits as starting points for simulations that consider clast deformation response to imposed stresses.

Our efforts thus far in the project have focused on proof-of-concept simulations of rubble deposition. The tasks involved include (1) preparing the 3D geometry for an example salt clast from the WIPP site for collision detection (previous section) and (2) simulating a rubble deposit using this clast using Geocosm's Cyberstone system. In conducting this analysis, we demonstrated that the data types, workflows, and simulation codes for rubble deposition all are functioning optimally. The simulation result that we describe below, however, is not intended to be representative of rubble deposits that are likely to occur at the WIPP site, which will be based on full size distributions prepared from the rubble.

The first portion of our analysis was to pre-process the 3D geometry for a clast from the WIPP site for rigid body physics simulation. Accurate collision detection for irregular, non-convex clasts is an extremely complex endeavor. Collision detection for objects with convex surfaces, by contrast, is computationally far simpler. Consequently, we use the hierarchical approximate

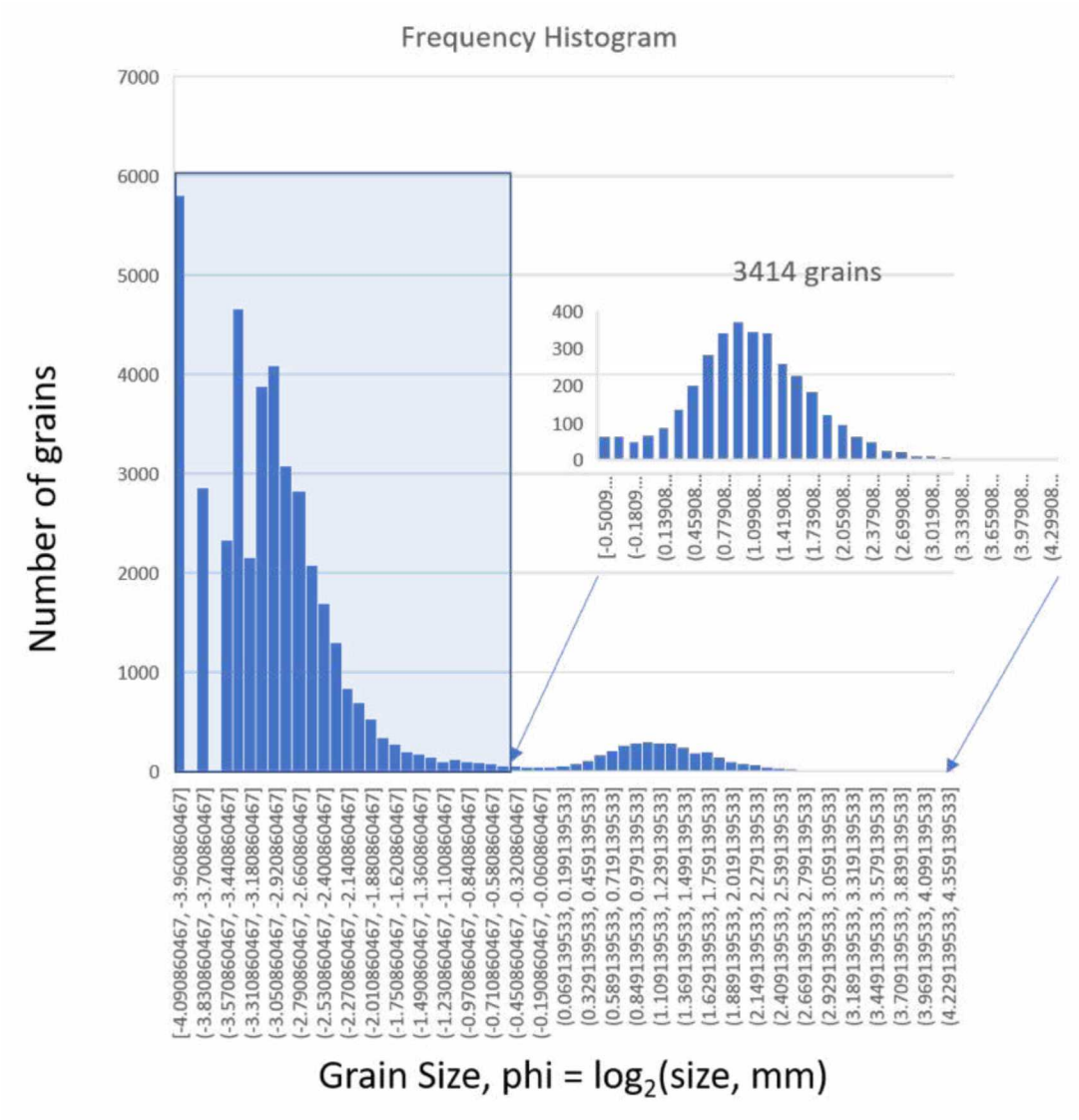

Figure 7-6. Frequency histogram of grain separates in Fig. 7-5, with grain size expressed in phi scale (log base 2 of grain size in mm).

convex decomposition approach (Mamou 2010) to represent each individual clast as a connected set of convex surface meshes. The result of this analysis on the example clast from the WIPP site is shown in Figs. 7-8 and 7-9 where the clast geometry is indicated in blue and the convex meshes that approximate it are shown in red. For the most part the convex decomposition process results in a geometry that closely mimics the actual grain shape. The most notable deviations in shape are indicated by the green arrows in the figures. Our assessment of this result is (1) that such deviations are likely to be less common for clasts shapes that omit neighboring clasts and (2) even for this example the impact of this deviation on simulated rubble packing geometries is likely negligible.

In the second portion of our proof-of-concept analysis we used the clast depicted in Figs. 7-8 and 7-9 as input for a simple rubble deposition simulation. In the simulation we arbitrarily allow

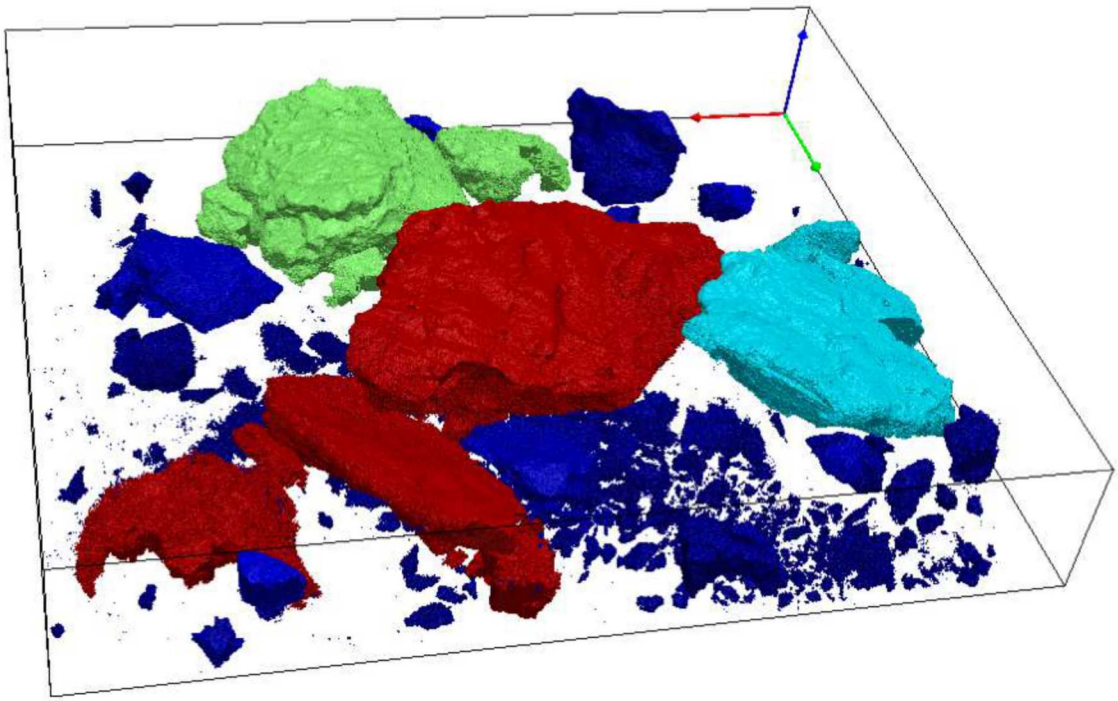

Figure 7-7. Grain separates taken from the top of the run-of-mine salt shown in Fig. 7-2 and Fig. 7-3.

the clasts that are deposited to have long axis lengths that range from 3.2 to 6.4 cm. In the simulation 1750 clasts were given random orientations and then dropped at random locations within a cylindrical container with a diameter of 40 cm (Fig. 7-10).

The flake-like shape of the reference clast results in cases where clasts in the deposition simulation obtain vertical orientations adjacent to the container walls. Consequently, to get a more realistic depiction of the internal structure of the rubble pack it is necessary to trim away the outer portions of the simulated pack as indicated in Fig. 7-11. Here we see the tendency for the clast particles to have sub-horizontal orientations. The porosity for this simulation is likely significantly higher compared to rubble that occurs at the WIPP site for several reasons: (1) the variation in clast sizes is much lower than expected at the WIPP site, (2) most of the clasts at the WIPP site have more equant forms (particularly in the finer size fractions) and (3) the irregular bump on the clast associated with the smaller unresolved neighboring clast (see Figures 1 and 2) reduces the packing efficiency and increases the effective friction.

7.3.5. CFD Modeling of Gas Transport in DRZ Core Fractures

To demonstrate how gas flux through the consolidating rubble pile can be simulated to estimate permeability and other transport properties, we first show connected volumes in the DRZ core piece in Fig. 7-12. The en echelon shapes of the extension fractures are evident in the segmented volumes of the fractures. We applied a flood-fill algorithm in the Scan-IP software to several of the larger fracture volumes, and the results shown that the fractures are percolating along the axis

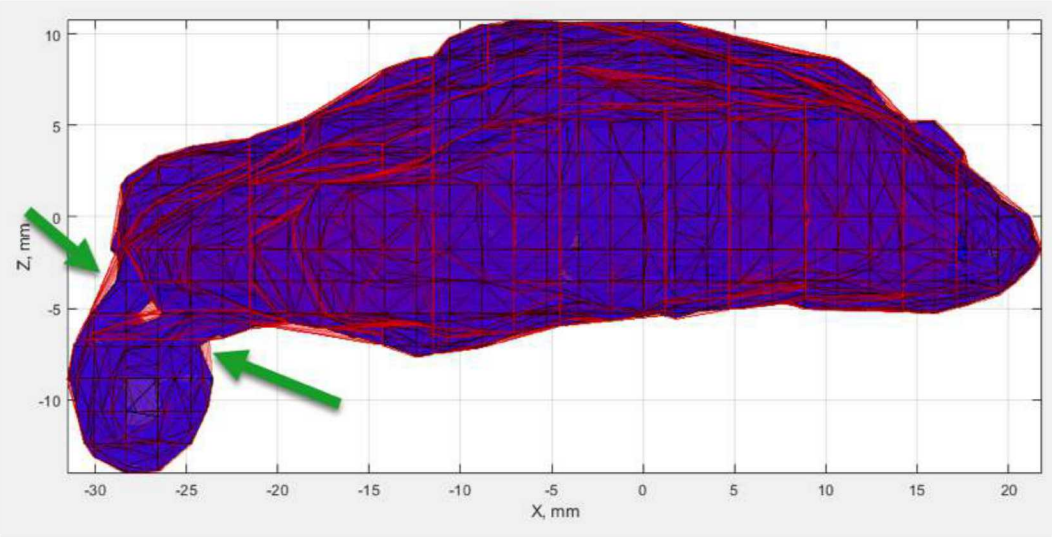

Figure 7-8. An example salt clast geometry from the WIPP site in blue together with the convex meshes that approximate it in red. The green arrows indicate regions where the convex meshes deviate somewhat from the clast shape.

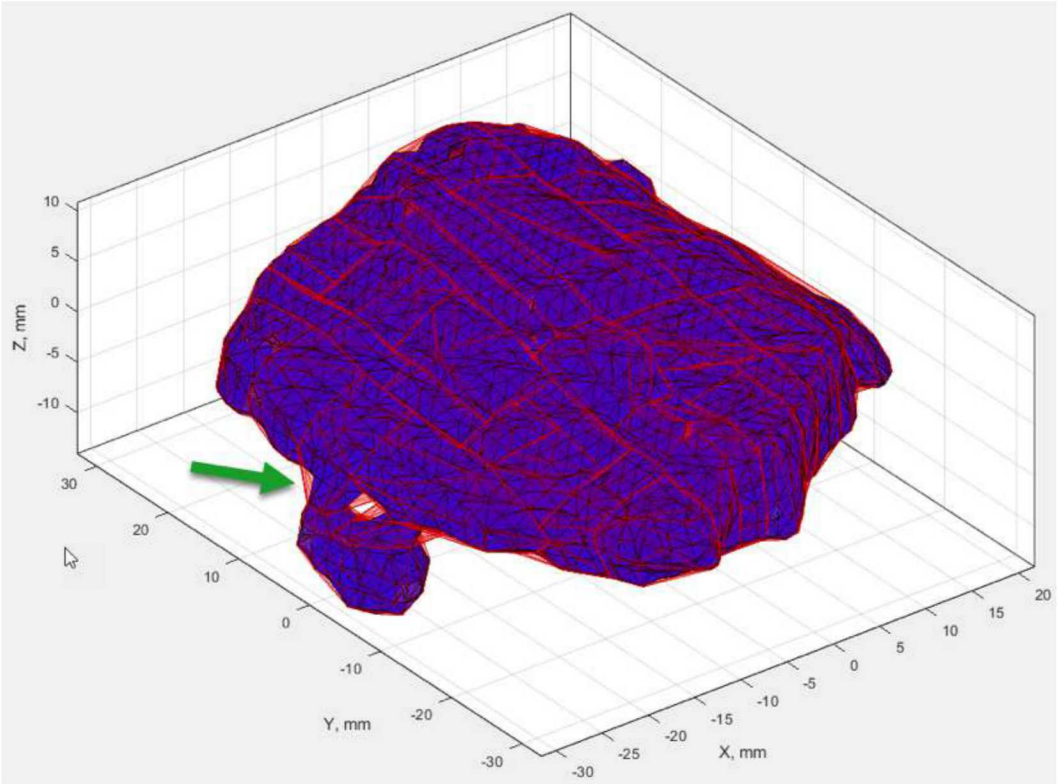

Figure 7-9. An alternative perspective of the same clast (blue) and convex meshes (red) shown in Fig. 7-8.

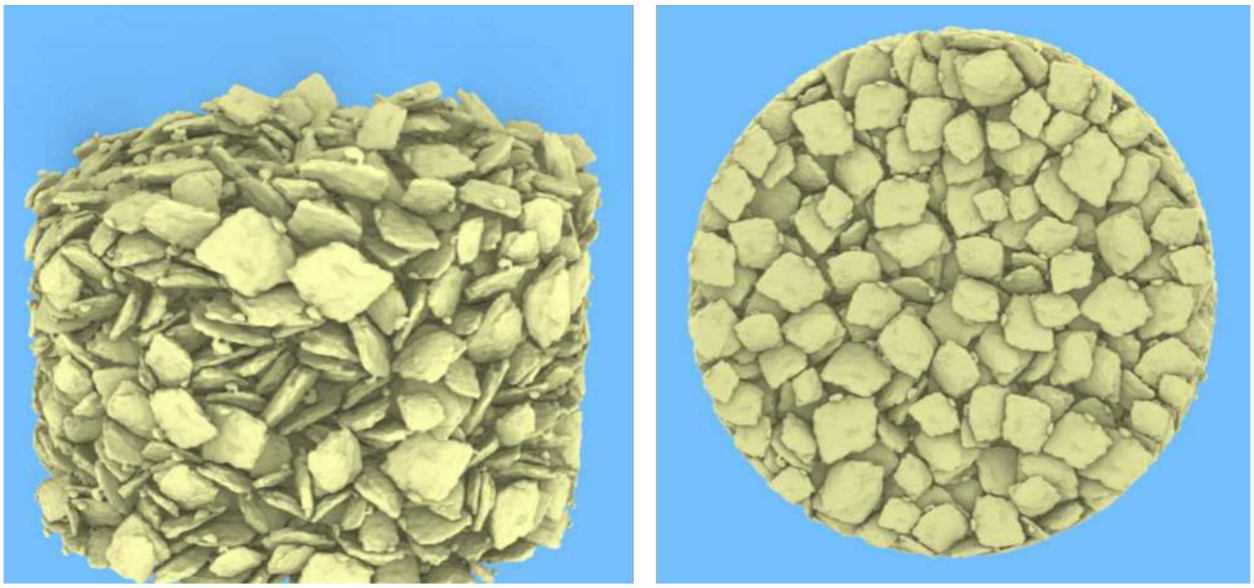

Figure 7-10. Rubble pack that resulted from depositing 1750 clasts with the shape shown in Fig. 7-8 into a cylindrical container.

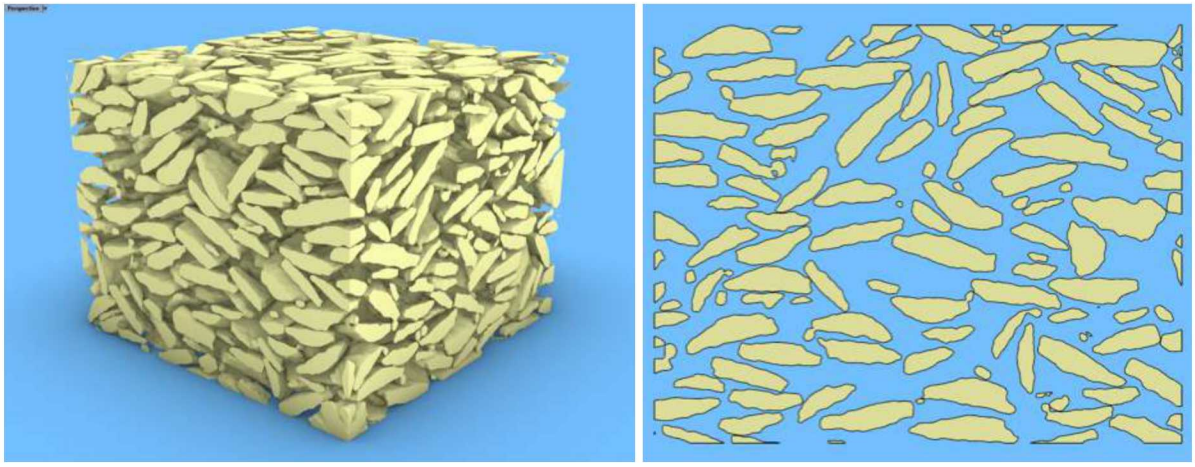

Figure 7-11. Trimmed portion of the rubble pack shown in Fig. 7-10. Left: 3D geometry of trimmed region. Right: a vertical cross section along the pack x-axis.

of the fractures, but are not connected to fractures above and below at least in the segmented volume examined, in that each color represents a unique connected volume.

We selected the "gold" colored fracture volume and used the Scan-FE algorithm to obtain a CFD triangular mesh for simulation purposes, shown in Fig. 7-13. An example simulation of dry air transport is shown in Fig. 7-14.

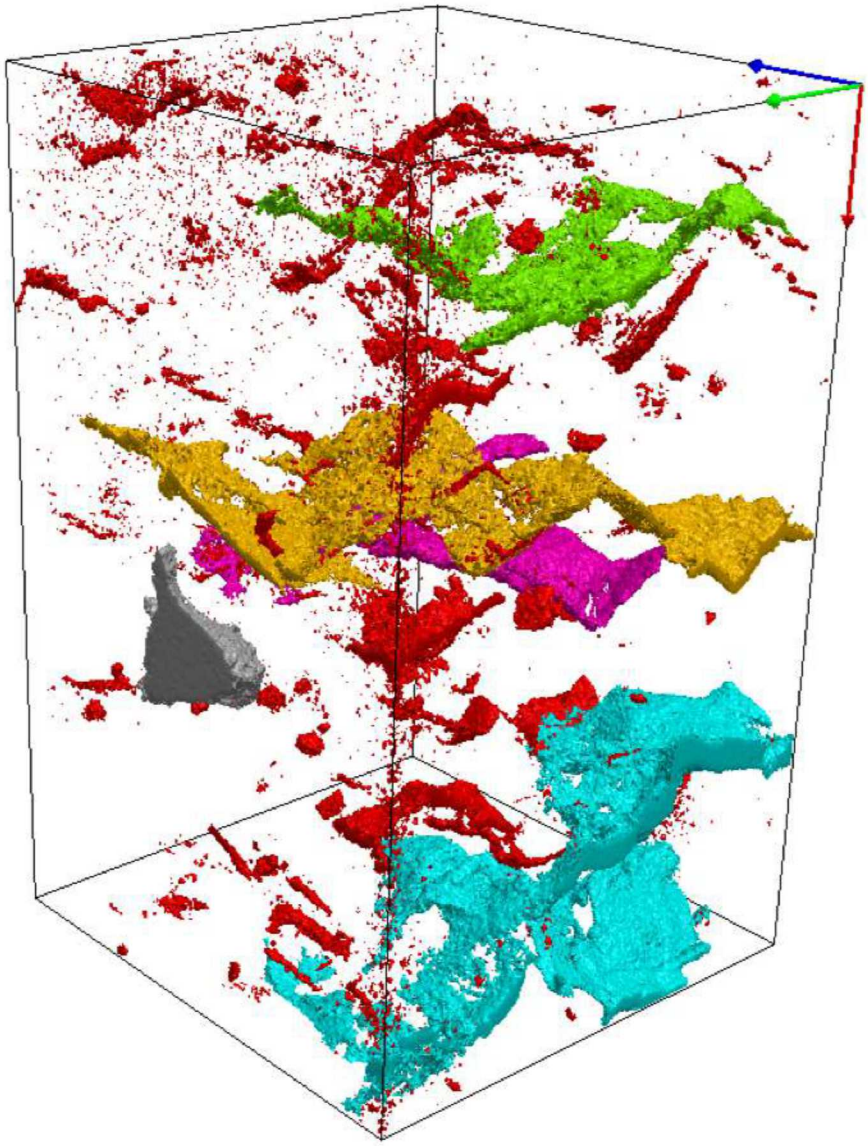

Figure 7-12. Connected volumes shown in different colors, for the extension fractures in the DRZ core piece shown in Fig. 7-1A.

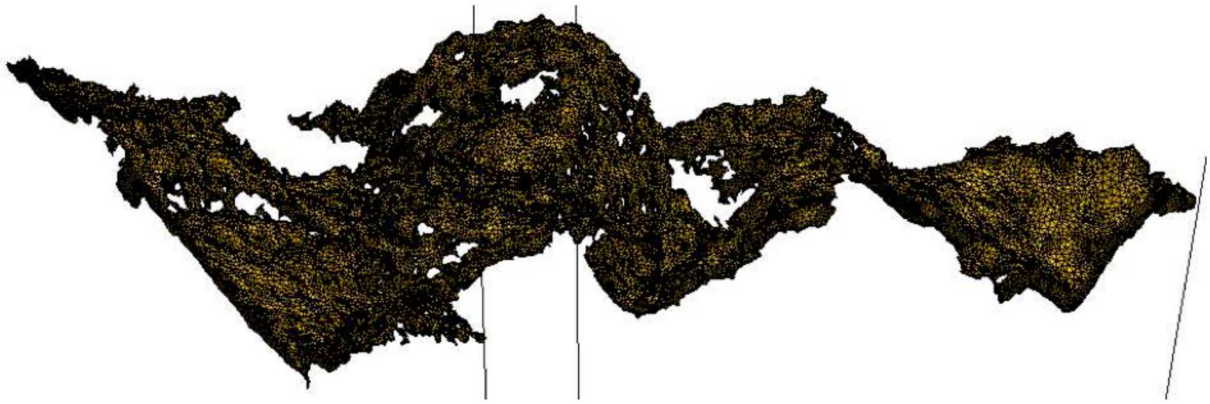

Figure 7-13. Triangular CFD mesh of WIPP DRZ core piece fracture.

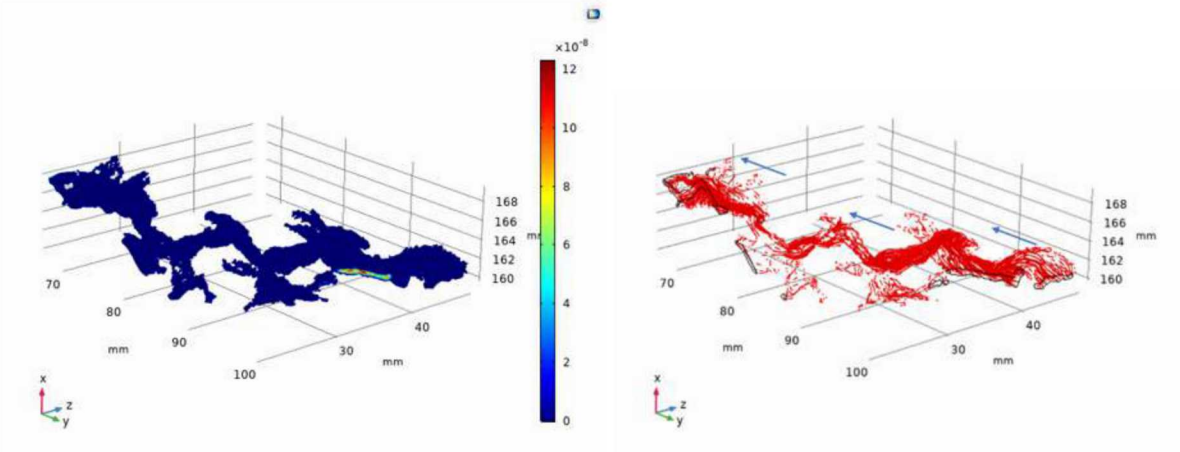

Figure 7-14. Flow simulations of dry air transport through DRZ fracture using mesh shown in Fig. 7-13 with COMSOL Multiphysics. The left figure shows velocity (although not evident in the image, the interior of the volume shows velocities of 1.0e-8 m/s for the boundary conditions chosen). The right figure shows simulated stream lines, depicting a central flow pathway and several "dead-end" portions of the fracture volume.

7.4. Conclusions

In this portion of the FY19 end-of-year report, we demonstrate a workflow for examining roof-fall consolidation and evolution of transport properties in the consolidating mass. This involves:

1. Characterization of rubble size and shape using X-ray micro-computed tomography
2. Image analysis to include solid segmentation and grain separation, using a variety of filters and watershed methods.
3. Creation of grain size distributions of rubble piles
4. Creation of grain surface meshes extracted from the separated particles, using the distribution as a guide.
5. Cyberstone modeling of rubble consolidation, extracting representative shapes and sizes using the provided STL files and the resulting volume distribution as a guide.
6. CFD modeling of gas transport in the consolidating rubble piles from the Cyberstone results.

One earlier conclusion is that it appears that the DRZ fractures percolate along the fracture lengths through centralized flow pathways but appear to not interact with nearby fractures. Current work involves perfecting the grain separation methods using different image analysis techniques and software. This will refine the distributions and grain mesh files passed to Geocosm for the consolidation simulations.

8. SUMMARY AND POTENTIAL FUTURE WORK

Author: Benjamin Reedlunn[§§]

The WIPP's long-term waste isolation performance depends on the permeability and porosity of rooms as they close. Sandia has models for rooms filled with nuclear waste containers or crushed salt, but models do not exist for empty room closure. Room ceilings and walls at the WIPP are known to cave in, and these cave-ins produce rubble piles on the floor of empty rooms. Prediction of an empty room's permeability and porosity evolution is a challenging endeavor for several reasons:

1. The formation and compaction of a rubble pile involves a series of complex physical processes: viscoplasticity, fracturing, rubble rearrangement, and healing.
2. The viscoplastic response of the surrounding rock formation is coupled with the mechanical response of the room contents, so one cannot simply focus on one without the other.
3. The permeability of a porous medium depends intimately on the geometry of the flow network, such that porosity alone cannot be used to predict permeability.
4. Unlike crushed salt, one cannot simply experimentally characterize a rubble pile's mechanical and hydraulic behavior while it consolidates–the rubble pieces are too large to be tested in a laboratory.
5. Many geomechanical numerical methods struggle to simulate fracture, severe deformations, pervasive contact, and healing.

Despite these challenges, Sandia is building models to simulate the permeability and porosity of empty rooms. One arm of this project is attempting to simulate gradual room closure, roof falls, and rubble pile consolidation using meshless methods. The other arm is using CFD to predict the permeability of excavation damaged and crushed salt samples characterized with X-ray μCT scans. At this juncture, both arms are focused on demonstrating capabilities rather than producing accurate predictions. Future efforts will strive to validate the models.

For the first arm of the project, two candidate meshless methods–the Immersed IGA Meshfree method and RKPM–were chosen to simulate the geomechanical aspects of empty room closure. Among other advantages, these meshless methods avoid material loss during fracture, can simulate severe deformations with relative ease, and do not require extensive reformulation of continuum material models. Two problems were devised to assess the suitability of these methods for empty room closure. The first problem involved the gradual closure of a simplified disposal room at the WIPP, without fracturing, such that the solution could be compared against Sierra/Solid Mechanics (2019)'s FEM simulation of gradual room closure. The second problem

[§§]Sandia National Laboratories, P.O. Box 5800, Albuquerque, NM 87185, USA

consisted of room closure with a roof fall and subsequent rubble pile consolidation. A simple elastic-viscoplastic-damage model, without strain hardening or healing, was utilized for both problems.

Both candidate meshless methods matched the Sierra/Solid Mechanics (2019) FEM simulation of gradual room closure reasonably well. Small differences between the gradual closure results are likely due to different viscoplastic rate scaling factors and the implicit nature of the meshless contact algorithms. The gradual room closure problem was also used to assess computational efficiency. As processors were added, the Immersed IGA Meshfree simulations scaled better than the RKPM simulations. This difference may be due to lack of a true 2-D capability, the domain partitioning algorithm, or the frequent semi-Lagrangian updates used in the RKPM simulations, but it does not appear to be a limitation of the RKPM itself. To investigate further, the gradual room closure problem was also simulated with CRK, which is a variant of RKPM. CRK used much of the Sierra/Solid Mechanics (2019) framework and scaled well as processors were added. The CRK simulations exhibited comparable accuracy and computational efficiency to the Sierra/Solid Mechanics (2019) FEM simulations.

The Immersed IGA Meshfree method and RKPM teams both successfully ran natural-looking two-dimensional simulations of roof falls and rubble pile reconsolidation. The IGA Meshfree team simulated roof falls, where a beam of salt above the room fractured, detached at a clay seam, fell into the room, and broke into multiple pieces. The surrounding rock salt eventually compacted the rubble pile to what appeared to be its final state, but metrics, such as relative porosity, were not presented to verify that consolidation completed. Initial three-dimensional IGA meshfree simulations of a roof fall appeared tractable, however these simulations did not complete due to excessive queue wait times. In the RKPM simulations, viscoplastic scaling was turned off during the roof fall in order to realistically capture the temporal evolution of the fall, and a brittleness parameter α was added to the salt damage evolution law. They found higher values of α produced more fractures when the roof fall landed on the floor, and that subsequent compaction of the rubble pile progressed more rapidly if the salt was more brittle. Although the relative porosity eventually stopped evolving, it did not dip beneath about 4 %. RKPM simulations of room closure with and without a clay seam above the room demonstrated that the clay seam encouraged earlier roof falls and faster reconsolidation.

The two meshless method simulations of roof falls and reconsolidation exhibited differences, but the differences appear to be due to modeling choices rather than inherent differences between the methods. First, when a clay seam was present, the IGA Meshfree simulations predicted a roughly 75° fracture angle relative to the ceiling, while the RKPM simulations predicted a roughly 45° angle. In addition, the IGA Meshfree simulations predicted the roof fall would occur within 0.2 yr of room excavation, while the RKPM simulations predicted 7 yr would elapse before a roof fall. These angle and time differences were probably due to the stress initialization procedure: the RKPM simulations paused to allowed the stress fields to equilibrate prior to letting the room close, while the IGA Meshfree simulations did not. Without an equilibration step, waves were likely ran through the rock and the clay seam exerted a downward force on the salt beam as the 75° angle fractures formed. Second, the IGA Meshfree simulation predicted the roof fall would break into pieces upon landing on the floor, while the RKPM simulation with $\alpha = 0$ predicted the roof fall would remain in one piece after impact. This difference in fragmentation predictions may

have been partly due to the clay seam downward force in the IGA meshfree simulations, but the IGA Meshfree simulations also did not turn off the viscoplastic scaling during the roof fall. At the time of impact in the IGA Meshfree simulations, the salt's viscoplasticity and damage rate were sped up by $s = 4.1 \times 10^8$ times. Third, the damaged salt envelope at the end of the IGA Meshfree simulations has a trapezoidal shape with the clay seam as the longer base, while the damage envelope resembles something closer to a diamond shape in the RKPM simulations. This damage envelope difference may be again due to the stress initialization procedure: the RKPM simulations allowed the diamond shape to fully evolve by delaying the roof fall by 6.8 yr.

The meshless methods both agreed, however, that collapsing rooms would reach their final state roughly 4 to 5 times faster than gradually closing rooms, where damage was prohibited. This result was not expected by the current authors, yet it could not be discarded as a numerical artifact or a poor modeling choice, because the fast closure may be due to a previously overlooked physical mechanism. Damage to the salt around a room causes the stress to redistribute, which effectively increases the size of the room without changing the void volume within the room. A simple viscoplastic closure study showed that a large circular room partially filled with rubble, idealized as intact salt, will close faster than an empty small circular room of the same initial void volume. This study does not, however, invalidate the previously posited mechanisms for slow closure of collapsing rooms. Damage likely causes rectangular or square rooms to transition to more stable circular room shapes, and a more realistic rubble pile should supply substantial back pressure to the surrounding rock formation to slow down room closure. Each effect may play an important role, which motivates the need to construct a model with the relevant physical processes and let simulation results guide conclusions rather than rely solely on intuition.

The second arm of this project began by generating flow network geometries from a sample of WIPP run-of-mine salt and EDZ salt. High-resolution X-ray μCT imaging was performed on the run-of-mine salt to examine the range in particle sizes and shape. The EDZ sample was "drop" tested and μCT reconstructions of before and after the drop were compared, showing the fragmented particle size distribution resulting from the drop impact. Image analysis techniques were applied and compared to demonstrate the ability to identify and separate particles in the tomograms, and to provide particle size distributions and grain separates for computational consolidation numerical schemes developed and performed by GeoCosm. Finally, a preliminary simulation of flow through a single fracture in the EDZ sample was carried out.

This project is still in its early stages and the modeling has many areas for improvement. A (incomplete) list of such areas is included below.

1. Mechanical Constitutive Model

    a) Salt is known to strain harden considerably in constant strain rate and creep tests. Adding isotropic and kinematic hardening could change stress distributions during gradual room closure, fracturing, impact, and rubble pile compaction.

    b) Salt mechanical behavior at strain rates above 10^{-3} 1/s has not been thoroughly investigated, yet dynamic strain rate behavior is probably important during rock fall impact.

c) Fracturing releases brine from isolated pores. Fluid assisted viscoplasticity (pressure solution redeposition) could accelerate the rate of rubble pile consolidation.

d) Fractures in salt heal under sufficient confining pressure. Adding healing could make the rubble pile stiffen and behave less like a fluid.

e) Salt macroscopically dilates as micro-cracks form and contracts as micro-cracks heal. These volumetric strains could play a role in the rubble pile mechanical response.

2. Geomechanical Numerical Method

a) Various numerical choices affect the width and behavior of highly damaged regions. These regions behave similar to a fluid since damaged material has little shear resistance and contact between damaged material was assumed to be frictionless. Highly damaged region behavior should be tuned to reasonably match experimental and in-situ observations.

b) The Immersed IGA Meshfree method and RKPM represent surfaces in an implicit manner. As implicit surfaces approach one another, they interact sooner and more gradually than they would with an explicit surface representation. This interaction leads to a contact gap and makes classical friction models difficult to implement. Alternative methods for simulating contact should be investigated.

c) All three meshless methods utilized viscoplastic rate scaling to enable explicit integration of the equations of motion. The scaling history was input at the start of the simulation, making it difficult to know how much to increase the scaling during a quasi-static period, or know when to reduce the scaling for a dynamic event. Unless an automatically adaptive scaling can be implemented, it may be worthwhile to investigate implicitly integrating the equations of motion.

3. Geomechanical Model

a) We hope to explicitly represent the macroscopic flow channels, but it remains to be seen whether a three-dimensional rubble pile simulation is computationally tractable.

b) Fractures frequently initiate at anhydrite stringers, clay seams, and other defect sites. A study of how rubble pile formation and consolidation depends on these defects could prove useful. For instance, could defects trigger a second or third roof fall after the first one?

c) The RKPM simulations showed that detachment at clay seams causes roof falls to happen significantly earlier. Experimental characterization of clay seam tensile and shear behavior could help create a more accurate clay seam model.

d) Potential back pressure due to gases trapped within the room will alter the room's final porosity and permeability, as well as the time required to reach this final porosity and permeability.

4. Hydraulic Model

a) A robust method to transfer the geomechanical simulation results, either from a meshless method or GeoCosm, into a CFD code needs to be developed.

b) Flow through a single fracture has been demonstrated, but it remains to be seen whether we have the computational power to simulate flow through an entire rubble pile with sufficient mesh resolution.

c) Interconnected micro-cracks permit fluid flow through salt. The permeability of micro-cracks could affect the effective permeability of the rubble pile once the consolidation process is nearly complete.

Despite the large number of potential improvements, the modeling results thus far are promising. The Immersed IGA Meshfree method and RKPM both handled the fracturing, large deformations, and contact involved in empty room closure. Gradual room closure simulations using CRK appear to have equivalent accuracy and computational efficiency to Sierra's FEM implementation. Finally, initial endeavors to characterize flow pathway geometry with μCT have been successful. Future efforts will improve the models and begin to compare predictions against laboratory and in-situ observations.

BIBLIOGRAPHY

Alnæs, M. S., Logg, A., Ølgaard, K. B., Rognes, M. E., and Wells, G. N. (Mar. 2014). "Unified form language: a domain-specific language for weak formulations of partial differential equations". In: *Acm trans. math. softw.* 40.2, 9:1–9:37. ISSN: 0098-3500.

Bazilevs, Y., Moutsanidis, G., Bueno, J., Kamran, K., Kamensky, D., Hillman, M. C., Gomez, H., and Chen, J. (2017a). "A new formulation for air-blast fluid–structure interaction using an immersed approach: part II—coupling of IGA and meshfree discretizations". In: *Computational mechanics* 60.1, pp. 101–116.

Bazilevs, Y., Moutsanidis, G., Bueno, J., Kamran, K., Kamensky, D., Hillman, M. C., Gomez, H., and Chen, J. (2017b). "A new formulation for air-blast fluid–structure interaction using an immersed approach. Part I: basic methodology and FEM-based simulations". In: *Computational mechanics* 60.1, pp. 101–116.

Belytschko, T. and Neal, M. O. (1991). "Contact-impact by the pinball algorithm with penalty and Lagrangian methods". In: *International journal for numerical methods in engineering* 31.3, pp. 547–572.

Buchholz, S. A., Keffeler, E., Lipp, K., DeVries, K. L., and Hansen, F. D. (Aug. 2019). *Proceedings of the 10th US/German workshop on salt repository research, design, and operation*. Tech. rep. SAND2019-9997R. US Department of Energy, Spent Fuel, Waste Science, and Technology.

Callahan, G. D. (Feb. 1999). *Crushed salt constitutive model*. Tech. rep. SAND98-2680. Albuquerque, NM, USA: Sandia National Laboratories.

Camphouse, R. C., Gross, M., Herrick, C., Kicker, D., and Thompson, B. (May 2012). *Recommendations and justifications of parameter values for the run-of-mine salt panel closure system design modeled in the PCS-2012 PA*. Memorandum.

Carrasco, R. (Sept. 2019a). *Empty areas at the Waste Isolation Pilot Plant*. Personal Communication.

Carrasco, R. (Sept. 2019b). *Roof fall photographs*. Personal Communication.

Chan, K. S., Munson, D., Fossum, A., and Bodner, S. (1998). "A constitutive model for representing coupled creep, fracture, and healing in rock salt". In: *Proc. 4th conference on the mechanical behavior of salt*. Ed. by M. Aubertin and H. R. H. Jr. Trans Tech Publications, pp. 221–234.

Chen, J.-S. (2001). "Nonlinear meshfree analysis program (NMAP)". In: *University of california, los angeles*.

Chen, J.-S., Hillman, M., and Chi, S.-W. (2017). "Meshfree methods: progress made after 20 years". In: *Journal of engineering mechanics* 143.4. DOI: 10.1061/(ASCE)EM.1943-7889.0001176.

Chen, J.-S., Hillman, M., and Rüter, M. (2013). "An arbitrary order variationally consistent integration for Galerkin meshfree methods". In: *International journal for numerical methods in engineering* 95.5, pp. 387–418.

Chen, J.-S., Pan, C., Wu, C.-T., and Liu, W. K. (1996). "Reproducing Kernel Particle Methods for large deformation analysis of non-linear structures". In: *Computer methods in applied mechanics and engineering* 139.1-4, pp. 195–227.

Chen, J.-S., Wu, C.-T., Yoon, S., and You, Y. (2001). "A stabilized conforming nodal integration for Galerkin mesh-free methods". In: *International journal for numerical methods in engineering* 50.2, pp. 435–466.

Chen, J.-S., Zhang, X., and Belytschko, T. (2004). "An implicit gradient model by a reproducing kernel strain regularization in strain localization problems". In: *Computer methods in applied mechanics and engineering* 193.27-29, pp. 2827–2844.

Chi, S.-W., Lee, C.-H., Chen, J.-S., and Guan, P.-C. (2015). "A level set enhanced natural kernel contact algorithm for impact and penetration modeling". In: *International journal for numerical methods in engineering* 102.3-4, pp. 839–866.

Cormeau, I. (1975). "Numerical stability in quasi-static elasto/visco-plasticity". In: *International journal for numerical methods in engineering* 9.1, pp. 109–127.

Düsterloh, U., Herchen, K., Lux, K.-H., Salzer, K., Günther, R.-M., Minkley, W., Hampel, A., Argüello Jr, J. G., and Hansen, F. D. (2015). "Joint Project III on the comparison of constitutive models for the thermomechanical behavior of rock salt. III. Extensive laboratory test program with argillaceous salt from WIPP and comparison of test results". In: *Proc. 8th conference on the mechanical behavior of salt*. Ed. by L. Roberts, K. D. Mellegard, and F. D. Hansen, pp. 13–21.

Günther, R. and Salzer, K. (2012). "Advanced strain-hardening approach: a powerful creep model for rock salt with dilatancy, strength and healing". In: *Proc. 7th conference on the mechanical behavior of salt*. Ed. by P. Bérest, M. Ghoreychi, F. Hadj-Hassen, and M. Tijani. CRC Press/Balkema, pp. 13–22.

Hampel, A. (2015). "Description of damage reduction and healing with the CDM constitutive model for the thermo-mechanical behavior of rock salt". In: *Proc. 8th conference on the mechanical behavior of salt*. Ed. by L. Roberts, K. Mellegard, and F. D. Hansen, pp. 361–371.

Herrick, C. G., Reedlunn, B., and Jensen, R. P. (2017). *Experimental investigation of small-scale openings in WIPP salt*. Tech. rep. TP-17-02 Rev. 0. July: Sandia National Laboratories.

Hillman, M. and Chen, J.-S. (2016). "An accelerated, convergent, and stable nodal integration in Galerkin meshfree methods for linear and nonlinear mechanics". In: *International journal for numerical methods in engineering* 107.7, pp. 603–630.

Homel, M. A. and Herbold, E. B. (2017). "Field-gradient partitioning for fracture and frictional contact in the Material Point Method". In: *International journal for numerical methods in engineering* 109.7, pp. 1013–1044.

Hughes, T. J., Cottrell, J. A., and Bazilevs, Y. (2005). "Isogeometric analysis: CAD, finite elements, NURBS, exact geometry and mesh refinement". In: *Computer methods in applied mechanics and engineering* 194.39-41, pp. 4135–4195.

Hughes, T. J. and Winget, J. (1980). "Finite rotation effects in numerical integration of rate constitutive equations arising in large-deformation analysis". In: *International journal for numerical methods in engineering* 15.12, pp. 1862–1867.

Kachanov, L. (2013). *Introduction to continuum damage mechanics*. Vol. 10. Springer Science & Business Media.

Kamensky, D., Behzadinasab, M., Foster, J. T., and Bazilevs, Y. (2019). "Peridynamic modeling of frictional contact". In: *Journal of peridynamics and nonlocal modeling*, pp. 1–15.

Kamensky, D., Moutsanidis, G., and Bazilevs, Y. (2018). “Hyperbolic phase field modeling of brittle fracture: Part I—theory and simulations”. In: *Journal of the mechanics and physics of solids* 121, pp. 81–98.

Kicker, D., Reedlunn, B., and Herrick, C. (2017). *Analysis plan for reconsideration of the WIPP geomechanical model for room closure*. Tech. rep. AP-178 Rev. 0. September: Sandia National Laboratories.

Kirby, R. C. and Logg, A. (Sept. 2006). “A compiler for variational forms”. In: *Acm trans. math. softw.* 32.3, pp. 417–444. ISSN: 0098-3500.

Koester, J. J., Tupek, M. R., and Mitchell, S. A. (Sept. 2019). *An agile design-to-simulation workflow using a new conforming moving least squares method*. Tech. rep. SAND2019-11851. Sandia National Laboratories.

Koester, J. J. and Chen, J.-S. (2019). “Conforming window functions for meshfree methods”. In: *Computer methods in applied mechanics and engineering* 347, pp. 588–621.

Kuhlman, K. L., Matteo, E. N., Reedlunn, B., Sobolik, M. M. M. S. R., Gross, M., and Simo, E. (Aug. 2019). *International collaborations on radioactive waste disposal in salt*. Tech. rep. M4SF-19SN010303064 (SAND2019-9134 R). Sandia National Laboratories.

Liu, X., Birchwood, R., Hooyman, P. J., et al. (2011). “A new analytical solution for wellbore creep in soft sediments and salt”. In: *45th us rock mechanics/geomechanics symposium*. American Rock Mechanics Association.

Logg, A., Mardal, K.-A., and Wells, G. N. (2012). *Automated solution of differential equations by the finite element method*. Springer. ISBN: 978-3-642-23098-1.

Logg, A. and Wells, G. N. (Apr. 2010). “DOLFIN: automated finite element computing”. In: *Acm trans. math. softw.* 37.2, 20:1–20:28. ISSN: 0098-3500.

Mamou, K. (2010). “Approximate convex decomposition for real-time collision detection”. In: *Game programming gems* 8, p. 202.

Martinez, M. J., Yoon, H., Kucala, A., Dewers, T., and Mendoza, H. (Sept. 2017). *Digital rock physics and 3D printing for fractured porous media*. Tech. rep. SAND2017-10469. Sandia National Laboratories.

Miehe, C., Hofacker, M., and Welschinger, F. (2010). “A phase field model for rate-independent crack propagation: robust algorithmic implementation based on operator splits”. In: *Computer methods in applied mechanics and engineering* 199.45-48, pp. 2765–2778.

Moutsanidis, G., Kamensky, D., Chen, J., and Bazilevs, Y. (2018). “Hyperbolic phase field modeling of brittle fracture: part ii—immersed IGA–RKPM coupling for air-blast–structure interaction”. In: *Journal of the mechanics and physics of solids* 121, pp. 114–132.

Moutsanidis, G., Koester, J. J., Tupek, M. R., Chen, J.-S., and Bazilevs, Y. (2019). “Treatment of near-incompressibility in meshfree and immersed-particle methods”. In: *Computational particle mechanics*, pp. 1–19.

Munson, D. E. (1997). “Constitutive model of creep in rock salt applied to underground room closure”. In: *International journal of rock mechanics and mining sciences* 34.2, pp. 233–247.

Munson, D. E., Fossum, A. F., and Senseny, P. E. (1989). *Advances in resolution of discrepancies between predicted and measured in situ WIPP room closures*. Tech. rep. SAND88-2948. Albuquerque, NM, USA: Sandia National Laboratories.

Munson, D. E., Torres, T. M., and Jones, R. L. (1987). “Pseudostrain representation of multipass excavations in salt”. In: *The 28th us symposium on rock mechanics (usrms)*. American Rock Mechanics Association.

Peerlings, R. H., Borst, R. de, Brekelmans, W. M., and Geers, M. (2002). "Localisation issues in local and nonlocal continuum approaches to fracture". In: *European journal of mechanics-a/solids* 21.2, pp. 175–189.

Peerlings, R. H., Borst, R. de, Brekelmans, W. M., and Vree, J. D. (1996). "Gradient enhanced damage for quasi-brittle materials". In: *International journal for numerical methods in engineering* 39.19, pp. 3391–3403.

Popp, T. (Nov. 2019). *Teutschenthal ventilation drift re-excavation date*. Personal Communication.

Popp, T., Minkley, W., Fillinger, E., and Boettge, V. (2018). "Closure of the Teutschenthal backfill mine – about the challenge to elaborate a geomechanical safety concept in salt formations". In: *The mechanical behavior of salt IX*. Ed. by S. Fahland, J. Hammer, F. D. Hansen, S. Heusermann, K.-H. Lux, and W. M. Minkley, pp. 84–99. ISBN: 978-3-9814108-6-0.

Reedlunn, B. (2016). *Reinvestigation into closure predictions of Room D at the Waste Isolation Pilot Plant*. Tech. rep. SAND2016-9961. Albuquerque, NM, USA: Sandia National Laboratories. DOI: 10.2172/1333709.

Reedlunn, B. (Nov. 2018a). *Enhancements to the Munson-Dawson model for rock salt*. Tech. rep. SAND2018-12601. Sandia National Laboratories. DOI: 10.2172/1481508.

Reedlunn, B. (2018b). "Joint Project III on the comparison of constitutive models for the mechanical behavior of rock salt: reinvestigation into isothermal room closure predictions at the Waste Isolation Pilot Plant". In: *The mechanical behavior of salt IX*. Ed. by S. Fahland, J. Hammer, F. D. H. Hansen, S. Heusermann, K.-H. Lux, and W. Minkley. BGR (Federal Institute for Geosciences and Natural Resources). ISBN: 978-3-9814108-6-0.

Reedlunn, B., Bean, J., Wilkes, J., and Bignell, J. (2019). *Simulations of Criticality Control Overpack container compaction at the Waste Isolation Pilot Plant*. Tech. rep. SAND2019-3106 O. Sandia National Laboratories.

Salzer, K., Günther, R.-M., Minkley, W., Naumann, D., Popp, T., Hampel, A., Lux, K.-H., Herchen, K., Düsterloh, U., Argüello Jr, J. G., and Hansen, F. D. (2015). "Joint Project III on the comparison of constitutive models for the thermomechanical behavior of rock salt. II. Extensive laboratory test program with clean salt from WIPP". In: *Proc. 8th conference on the mechanical behavior of salt*. Ed. by L. Roberts, K. D. Mellegard, and F. D. Hansen, pp. 3–12.

Scherzinger, W. M. and Lester, B. T. (Sept. 2019). *Library of advanced materials for engineering (LAME) 4.54.* Tech. rep. SAND2019-11095. Sandia National Lab.(SNL-NM), Albuquerque, NM (United States).

Sierra/Solid Mechanics (2019). *Sierra/Solid Mechanics User's Guide.* 4.52. SAND2019-2715. Sandia National Laboratories. Albuquerque, NM, USA; Livermore, CA, USA.

Stone, C. M. (Aug. 1997). *Final disposal room structural response calculations*. Tech. rep. SAND97-0795. Albuquerque, NM, USA; Livermore, CA, USA: Sandia National Laboratories.

Sulsky, D., Chen, Z., and Schreyer, H. L. (1994). "A particle method for history-dependent materials". In: *Computer methods in applied mechanics and engineering* 118.1-2, pp. 179–196.

US DOE (1996). *Title 40 CFR part 191 compliance certification application for the Waste Isolation Pilot Plant (October). 21 vols.* Tech. rep. DOE/CAO-1996-2184. US Department of Energy: Carlsbad Field Office.

US DOE (Apr. 2014a). *Accident investigation report phase 1. Radiological release event at the Waste Isolation Pilot Plant on February 14, 2014*. Tech. rep. United States Department of Energy Office of Environmental Management.

US DOE (2014b). *Title 40 CFR part 191 subparts B and C compliance recertification application for the Waste Isolation Pilot Plant, carlsbad, nm*. Tech. rep. DOE/WIPP 2014-3503. US Department of Energy: Carlsbad Field Office.

US DOE (Apr. 2015). *Accident investigation report phase 2. Radiological release event at the Waste Isolation Pilot Plant on February 14, 2014*. Tech. rep. United States Department of Energy Office of Environmental Management.

Wei, H., Chen, J.-S., and Hillman, M. (2016). "A stabilized nodally integrated meshfree formulation for fully coupled hydro-mechanical analysis of fluid-saturated porous media". In: *Computers & fluids* 141. Advances in Fluid-Structure Interaction, pp. 105–115. ISSN: 0045-7930. DOI: https://doi.org/10.1016/j.compfluid.2015.11.002. URL: http://www.sciencedirect.com/science/article/pii/S0045793015003631.

APPENDIX A. Finite Element Modeling Details

Author: Benjamin Reedlunn[¶¶]

A.1. Model Setups for Room Shape and Size Studies

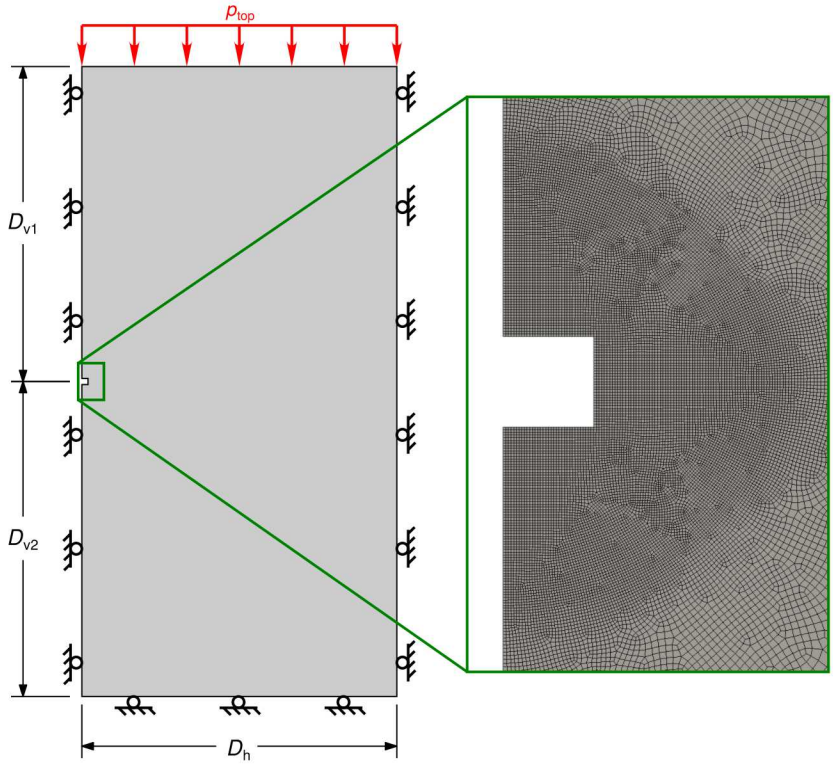

Figure A-1. Room geometry, boundary conditions, and mesh used to investigate initial room shape and size on viscoplastic room closure. (2-to-1 rectangular room shown)

Simple plane strain simulations of a square room, a 2-to-1 rectangular room, a small circular room, and a big circular room filled with idealized rubble were performed to assess how viscoplastic closure depends on initial room shape and size. The square, rectangular, and small circular room each began with an initial cross-sectional area of 30.25 m^2. The big room's initial cross-sectional area, ignoring the idealized rubble, was set to 60.5 m^2, and the idealized rubble cross-sectional area was set to 30.25 m^2 to create an initial void cross-sectional area of 30.25 m^2.

[¶¶]Sandia National Laboratories, P.O. Box 5800, Albuquerque, NM 87185, USA

Each long, slender, and isolated room was placed in a stratigraphy of plain salt, without anhydrite, polyhalite, or clay strata.

The salt material model was the M-D model with Calibration 3B in Table 5.1 of Reedlunn (2018a), except for two minor differences. First, the Hosford exponent $a = 18$ instead of $a = 16$, simply because these simulations were run prior to finalizing Calibration 3B. Second, steady-state creep mechanism 3 was turned off by setting $q = B_1 = B_2 = 0$. As discussed in Appendix A.1 of Reedlunn et al. (2019), mechanism 3 often makes the material model's ordinary differential equations difficult to numerically solve, yet it had negligible impact on the closure of a disposal room on the upper horizon, so mechanism 3 was neglected for these analyses.

As shown for the rectangular room in Fig. A-1, the simulation domain boundaries were far away from the room in an attempt to make the room closure independent of domain size. The boundary conditions involved rollers on three sides (the left rollers represent a mirror boundary) and a normal pressure of p_{top} at the top. The domain boundaries were $D_{\text{h}} = D_{\text{v1}} = D_{\text{v2}} = 200$ m away from the square, rectangular, and small circular room, while the domain boundaries were $D_{\text{h}} = D_{\text{v1}} = D_{\text{v2}} = 282.84$ m away from the big circular room filled with idealized rubble. Although a domain size convergence study was not performed, a past unpublished study by the current author, using a similar simulation setup, found these domain sizes to be large enough to avoid influencing the room closure. The normal pressure at the top was $p_{\text{top}} = 10.27$ MPa for the square, rectangular, and small circular room, and was $p_{\text{top}} = 8.41$ MPa for the big circular room. These pressure boundary conditions both lead to a lithostatic pressure of 14.76 MPa at the room center, which is the approximate lithostatic pressure of clay seam G at the WIPP.

The salt stress fields immediately following the (instantaneous) room excavation were calculated using the fluid pressure ramp down procedure defined at the end of Section 2.2.1.

A.2. Numerical Settings for Room Shape and Size Studies

The room shape and size studies were performed using finite element meshes similar to that shown in the magnified view in the right of Fig. A-1. The rectangular room's half width has 34 elements across it, each with a width of 0.114 m. Other room shapes and sizes utilized meshes with similar element densities near the room and similar coarsening further away from the room. Formal mesh convergence studies were not performed, but the mesh convergence study for the gradual room closure problem in Section 5.3 found that 0.210 m and 0.105 m element sizes near the room produced nearly the same closure curve, suggesting that 0.114 m elements were small enough for the room shape and size studies. All finite element simulations used selective deviatoric elements with the deviatoric parameter set to 1 (Sierra/Solid Mechanics 2019).

The implicit quasi-static capability in Sierra/Solid Mechanics (2019) was utilized to solve the discretized equilibrium equations. Sierra/Solid Mechanics (2019) employed a multi-level solver to balance internal forces, reaction forces, applied loads, and contact forces. The inner loop used a conjugate gradient solver for the equilibrium equations, with the contact interactions held fixed. The outer loop utilized an augmented Lagrange algorithm to resolve the contact interactions, with

the nodal displacements outside of the contact zone held fixed. Under the default settings, Sierra/Solid Mechanics accepts an outer loop contact iteration as converged if

$$\frac{\sqrt{\boldsymbol{R}\cdot\boldsymbol{R}}}{\sqrt{\boldsymbol{F}^{\mathrm{r}}\cdot\boldsymbol{F}^{\mathrm{r}}}} = \hat{R} \leq \hat{R}_{\max}. \tag{A.1}$$

where $\boldsymbol{R}$ is the residual from the discretized equilibrium equations, $\boldsymbol{F}^{\mathrm{r}}$ is the reaction force vector, and $\hat{R}_{\max}$ is the user specified maximum value of the relative residual norm $\hat{R}$. A past unpublished convergence study by the current author on a similar simulation setup found $\hat{R}_{\max} = 10^{-6}$ was sufficiently small for $D_{\mathrm{h}} = D_{\mathrm{v1}} = D_{\mathrm{v2}} = 400$ m, so $\hat{R}_{\max} = 10^{-6}$ was utilized herein.

Implicit solvers can take arbitrarily large time steps without numerical instabilities, but large time steps can cause inaccurate integration of the M-D model's ordinary differential equations. A past unpublished time step size sensitivity study found that starting with a time step size of $t = 1.0$ s, after the virtually instantaneous excavation, followed by growth rates of 2 %, 4 %, and 8 % all produced the same closure curves for 7.8 yr after room excavation. As the simulations herein were run well past 7.8 yr, the time step increment began at $t = 0.1$ s and was allowed to grow by only 2 % after each successful step.

The results of the room shape study can be found in Section 1.2.1, while the results of the room size study can be found in Section 6.2.

A.3. Numerical Settings for Gradual Room Closure Simulations

The gradual room closure problem defined in Section 2.2.1 was simulated using Sierra/Solid Mechanics (2019)'s finite element implementation to provide reference solutions to compare the meshless simulations against. All finite element simulations used selective deviatoric elements with the deviatoric parameter set to 1 (Sierra/Solid Mechanics 2019). Some finite element simulations used the implicit quasi-static solver, while others used the explicit dynamics solver, so numerical settings for both are described below.

Much of implicit solver description in Appendix A.2 applies to the gradual room closure simulations, but two settings differed. First, Appendix A.1 of Reedlunn et al. (2019) found that $\hat{R}_{\max} = 10^{-4}$ was sufficiently small for an upper horizon disposal room closure setup because the domain size was far smaller than $D_{\mathrm{h}} = D_{\mathrm{v1}} = D_{\mathrm{v2}} = 200$ m, so $\hat{R}_{\max} = 10^{-4}$ was utilized for the gradual room closure simulations herein. Second, the time step increment began at $t = 1.0$ s, instead of 0.1 s, but it was still allowed to grow by only 2 % after each successful step.

Explicitly integrated finite element solutions were generated using the viscoplastic rate scaling described in Section 2.2.4 to enable a direct comparison of computational performance against the meshless methods. The viscoplastic rate scaling was of the form

$$s = \begin{cases} s_0 & t_{-1}^{\mathrm{mb}} \leq t^{\mathrm{mb}} \leq 0 \\ s_0 + s_1\, t^{\mathrm{mb}} & t^{\mathrm{mb}} > 0, \end{cases} \tag{A.2}$$

where $s_0 = 10^{-2}$, $s_1 = 2\times 10^{9}$ s^{-1}, and $t_{-1}^{\mathrm{mb}} = -0.5$. Holding $s = s_0$ during $t_{-1}^{\mathrm{mb}} \leq t^{\mathrm{mb}} \leq 0$ allowed the virtually instantaneous room excavation using the procedure defined at the end of Section 2.2.1 to

proceed over 10 ms of physical time. It should also be mentioned that contact enforcement with explicit time integration in Sierra/Solid Mechanics requires one to specify a number of contact iterations per momentum balance time step. Appendix A.2.2 of Reedlunn et al. (2019) found that upper horizon disposal room closure was relatively insensitive to the number of contact iterations. They found 20 contact iterations were more than sufficient, so that value was employed herein.

Note that a direct implementation of the material model specified in Section 2.2.3.1 did not exist in Sierra/Solid Mechanics (2019), so the M-D model was reduced to the form in Section 2.2.3.1. The reduction involved setting the transient creep parameters to zero, turning off steady-state creep mechanism 1 and 3, and setting the Hosford exponent $a = 4$. The remaining M-D model parameters were set using the parameters in the "Gradual Closure" column of Table 2-1.

The results of the finite element gradual room closure simulations are shown in several locations in the report. The finite element results labeled as "Sierra" in Fig. 3-4 and "SNL" in Fig. 4-9 correspond to an implicit quasi-static solution with a 0.105 m element size near the room. Section 5.3 includes this same implicit quasi-static solution with a 0.105 m element size near the room, as well as three different explicit dynamic solutions with 0.419 m, 0.210 m, and 0.105 m element sizes near the room.

DISTRIBUTION

Email—External

Name	Company Email Address	Company Name
Russ Patterson	russ.patterson@cbfo.doe.gov	U.S. Department of Energy Carlsbad Field Office
George Basabilvazo	george.basabilvazo@wipp.ws	U.S. Department of Energy Carlsbad Field Office
Michael Brown	mike.brown@cbfo.doe.gov	U.S. Department of Energy Carlsbad Field Office
Michael Gross	mgross713@gmail.com	MG Enterprises
Gordan Gjerapic	gordan_gjerapic@golder.com	Golder Associates
Till Popp	till.popp@ifg-leipzig.de	Institute für Gebirgsmechanik
Markus Knauth	markus.knauth@ifg-leipzig.de	Institute für Gebirgsmechanik
Evan Keffeler	evan.keffeler@respec.com	RESPEC
Frank Hansen	francis.d.hansen@gmail.com	N/A
J. Guadalupe Arguello	llae.arguello@att.net	N/A
Howard Schreyer	schreyer@unm.edu	University of New Mexico

Email—Internal

Name	Org.	Sandia Email Address
M. Martinez	1516	mjmarti@sandia.gov
F. Beckwith	1542	fbeckwi@sandia.gov
T. Shelton	1542	trshelt@sandia.gov
M. Tupek	1542	mrtupek@sandia.gov
S. Klenke	1550	seklenk@sandia.gov
A. Brundage	1554	albrund@sandia.gov
C. Vignes	1558	cvignes@sandia.gov
J. Bean	1554	jebean@sandia.gov
K. Mish	1555	kdmish@sandia.gov
J. Bishop	1556	jebisho@sandia.gov

Name	Org.	Sandia Email Address
J. Pott	1557	jpott@sandia.gov
E. Fang	1558	hefang@sandia.gov
R. C. Camphouse	8842	rccamph@sandia.gov
E. Matteo	8842	enmatte@sandia.gov
R. Rechard	8842	rprecha@sandia.gov
E. Hardin	8844	ehardin@sandia.gov
K. Kuhlman	8844	klkuhlm@sandia.gov
M. Mills	8844	mmmills@sandia.gov
E. Stein	8844	ergiamb@sandia.gov
B. Park	8862	bypark@sandia.gov
S. Sobolik	8862	srsobol@sandia.gov
T. Zeitler	8862	tzeitle@sandia.gov
S. Broome	8864	stbroom@sandia.gov
C. Herrick	8864	cgherri@sandia.gov
R. Jensen	8864	rpjense@sandia.gov
R. C. Choens	8864	rcchoen@sandia.gov
M. Ingraham	8864	mdingr@sandia.gov
M. Lee	8864	mylee@sandia.gov
S. Bauer	8866	sjbauer@sandia.gov
P. Shoemaker	8880	peshoem@sandia.gov
D. Kicker	8881	dckicke@sandia.gov
R. Kirkes	8883	grkirke@sandia.gov
M. D. Rascon	8880	mdrasco@sandia.gov
C. Leigh	8888	cdleigh@sandia.gov
Technical Library	01177	libref@sandia.gov



Sandia National Laboratories

Sandia National Laboratories is a multimission laboratory managed and operated by National Technology & Engineering Solutions of Sandia LLC, a wholly owned subsidiary of Honeywell International Inc., for the U.S. Department of Energy's National Nuclear Security Administration under contract DE-NA0003525.